

**Synthesis and Characterization of Novel Functional
Materials based on Cellulose and Graphene Oxide**

DISSERTATION

Zur Erlangung des akademischen Grades
Doktor rerum naturalium
(Dr. rer. nat.)
vorgelegt
dem Fakultät Chemie und Lebensmittelchemie
der Technischen Universität Dresden
von

Yian Chen

Geboren am 1. Dezember 1992 in Shandong, V. R. China

Eingereicht am 06.03.2020

Die Dissertation wurde in der Zeit von Oktober 2016 bis März 2020 im
Leibniz-Institut für Polymerforschung Dresden e. V. angefertigt.

©Yian Chen, 2020

Acknowledgement

First and foremost, I am very grateful to my supervisor, Prof. Brigitte Voit, whose useful suggestions and patient guidance give me continuous confidence and motivation to complete the PhD career. She is a very kind and patient supervisor and gave me the opportunity to broaden my horizon. I would like to express my sincere gratitude to Prof. Haisong Qi. He personally taught me lots of measurement and helped me to design many experimental plans. More like a friend, he was very enthusiastic to help me to start the PhD career and to adjust to life in Germany.

In particular, I am very honored to join in the research group of Dr. Petra Pötschke. She influenced and inspired me a lot in my master career. Before the PhD stage, I read lots of her paper and hoped to I can join in her group. Dream may come true. I learned the rigorous scientific attitude and many scientific ideas and skills from her. Moreover, the NB group is like a family. I have had a very enjoyable time here. Then, I want to sincerely thank Dr. Jürgen Pionteck. He is very kind and humorous. At the same time, he is also very responsible. He made a lot of useful comments and help for me. He also shared some useful papers with me. I am very honored and grateful to meet and learn from these two excellent teachers.

To my dear motherland: China. I want to thank China Scholarship Council for the financial support and for the PhD study in Germany.

I am grateful to Dr. Beate Krause for the training of electrical conductivity measurement, Dr. Lothar Jakisch for the training of laboratory safety, Dr. Dieter Jehnichen for XRD testing, Ms. Uta Reuter for TEM observation, Mr. Minoj Gnanaseelan for the SEM observation, Dr. Dieter Fisher for Raman test, Ms. Kerstin Arnhold for the thermal analysis, Dr. Konrad Schneider for tensile testing, and Ms. Bettina Pilch for UV-Vis spectrophotometer testing.

I also thanks to my lovely colleges: Ms. Xueyan Zhao, Mr. Yilong Li, Mr. Xinlei Tang, Dr. Jianwei Zhang. They give me lots of help and suggestion in the academic career and daily life. Especially, I want to thank my friend Xinlei Tang. He is a very special and kind person. I am very happy to have had a lot of good times with him.

Many thanks to my family: my parents and my sister. They are my solid backing and give me support and encouragement.

Table of Contents

1. Aim of this work	12
2. Introduction.....	16
2.1. Cellulose	16
2.2. Graphene.....	17
2.3. Green solvents for cellulose/graphene nanocomposite materials	19
2.3.1. Ionic liquids	19
2.3.2. NaOH/urea aqueous solution.....	22
2.3.3. NMMO solvent.....	25
2.3.4 Other solvent for cellulose/graphene composites	26
2.4. Cellulose/graphene composite materials.....	29
2.4.1 Cellulose/graphene composite films and membranes.....	30
2.4.2 Cellulose/graphene composite fibers	41
2.4.3 Cellulose/graphene composite hydrogels and aerogels	43
2.5. Cellulose/graphene-based functional materials	46
2.5.1 Antibacterial activities with silver nanoparticles	47
2.5.2 Enhanced properties with poly (vinyl alcohol) (PVA).....	47
2.5.3 Photocatalysts with Cu ₂ O	48
3. Experimental part.....	49
3.1. Materials and chemicals.....	49
3.2. Preparation of samples	49
3.2.1 Preparation of cellulose/rGO composites	49
3.2.2 Preparation of cellulose/GO/Fe ₃ O ₄ composites	51
3.2.3 Preparation of cellulose/rGO/Fe ₃ O ₄ composites.....	52
3.3. Instruments and characterization methods.....	53

3.3.1	Characterization of morphology and microstructure, and thermogravimetric analysis.....	53
3.3.2	Characterization of sensing abilities	54
3.3.3	Characterization of catalytic activity	58
3.3.4	Characterization of electrical, dielectric, magnetic, and EMI shielding abilities	59
4.	Result and discussion.....	60
4.1.	Cellulose/rGO composites for multiple sensing applications.....	60
4.1.1	Introduction.....	60
4.1.2	In-situ chemical reduction of GO	63
4.1.3	Properties of cellulose/GO and cellulose/rGO composites.....	65
4.1.4	Temperature and humidity sensor of cellulose/rGO composites	68
4.1.5	Strain sensor of cellulose/rGO composites	70
4.1.6	Liquid sensor of cellulose/rGO composites	72
4.1.7	Vapor sensor of cellulose/rGO composites	77
4.1.8	Summary	83
4.2.	Cellulose/GO/Fe ₃ O ₄ hydrogels for advanced catalytic materials for the heterogeneous Fenton-like reaction	85
4.2.1	Introduction.....	85
4.2.2	Structure and morphological analysis of cellulose/GO/Fe ₃ O ₄ composites.....	86
4.2.3	Optimization analysis of the AO7 degradation conditions	89
4.2.4	Catalytic activity of cellulose/GO/Fe ₃ O ₄ hydrogels	91
4.2.5	Summary	100
4.3.	Cellulose/rGO/Fe ₃ O ₄ aerogels for EMI shielding application.....	101
4.3.1	Introduction.....	101
4.3.2	Characterizations of cellulose/rGO/Fe ₃ O ₄ composites	102
4.3.3	Electrical conductivity properties for different samples	106

4.3.4 Dielectric properties of different films and aerogels	109
4.3.5 Magnetic properties of different films and aerogels	109
4.3.6 EMI performance of different films and aerogels.....	111
4.3.7 The possible EMI shielding mechanism	116
4.3.8 Summary	118
5. Summary	119
6. Outlook	121
Bibliography	123
Publications and attended conferences	147
Versicherung	148
Erklärung.....	148

List of Abbreviations and Symbols

Abbreviations

A	absorptivity
AC	activated carbon
AO7	acid orange 7
b	positive constant
C	concentration
CaCl ₂ ·6H ₂ O	calcium chloride hexahydrate
Ca(NO ₃) ₂ ·4H ₂ O	calcium nitrate tetrahydrate
CB	carbon black
cm	centimeter (unit)
CNC	nanocrystalline cellulose
CNTs	carbon nanotubes
CV	cyclic voltammetry
d	thickness
dB	decibel
DMAc	dimethylacetamide
DMF	dimethylformamide
EDA	electron donor-electron acceptor
EG	ethylene glycol
EMI	electromagnetic interference
EMIMAc	1-ethyl-3-methylimidazolium acetate
E _T	solvent polarity
eV	electron volt
f	flow rate of MFC 1
F	flow rate of MFC 2
FeCl ₂	ferrous chloride
FeCl ₃	iron chloride
FTIR	fourier-transform infrared

g	gram (unit)
GHz	gigahertz (unit)
GO	graphene oxide
GV	galvanostatic
h	hour (unit)
HCl	hydrochloric acid
H ₂ O ₂	hydrogen peroxide
HO•	hydroxyl radical
HOO•	hydroperoxyl radicals
H ₂ SO ₄	sulphuric acid
ILs	ionic liquids
K	Kelvin temperature degree (unit)
KCl	potassium chloride
K ₂ CO ₃	potassium carbonate
kV	kilovolt (unit)
L	liter (unit)
LED	light-emitting diodes
LiOH	lithium hydroxide
min	minute (unit)
μm	micrometer (unit)
M _s	saturation magnetization
MWCNT	multiwall carbon nanotube
NaOH	sodium hydroxide
nm	nanometer (unit)
NaCl	sodium chloride
NaNO ₂	sodium nitrite
NFC	nanofibrillated cellulose
NMMO	N-methylmorpholine-N-oxide
NTC	negative temperature coefficient

P	input air pressure
PCC	phase change composites
PEG	polyethylene glycol
P_i	saturated partial pressure
PVA	poly (vinyl alcohol)
R	resistance
	reflectivity
R_0	initial resistance
rGO	reduced graphene oxide
RH	relative humidity
R_{rel}	relative electrical resistance change
R_t	transient resistance at time t
RTILs	room temperature molten salts
s	second (unit)
S	Siemens (unit)
SE	shielding effectiveness
SE_A	shielding effectiveness due to absorption
SE_M	multiple internal reflection of effectiveness
SEM	scanning electron microscope / microscopy
SE_R	reflection of effectiveness
SE_{total}	total value of shielding effectiveness
SMO	semiconductor metal oxide
T	transmissivity
TCR	temperature coefficient of resistance
TEM	transmission electron microscope microscopy
TGA	thermogravimetric analysis
THF	tetrahydrofuran
UV	ultraviolet
V	volt (unit)

VOCs	volatile organic compounds
wt.	weight (unit)
XPS	X-ray spectroscopy
XRD	X-ray diffraction
Symbols	
$^{\circ}\text{C}$	degree centigrade (unit)
θ	angle
ω	angular frequency
ϵ_0	dielectric constant of vacuum
μ_r	real permeability
σ	electrical conductivity
ΔR_S	the change of electrical resistance due to swelling
ΔR_A	the change of electrical resistance due to absorption

1. Aim of this work

Cellulose, the most abundant renewable material, is widely used in various applications due to its fascinating structure and attractive properties, such as chemical stability, biodegradability, renewability, derivatizability, and biocompatibility. Graphene, a single nanosheet with sp^2 -hybridized carbon atoms, has received more and more attention in recent years because of its unique 2D structure and outstanding properties. Thus, to produce functional and smart composite materials based on graphene and cellulose, which endows cellulose matrix with tailored properties, such as sensing performance, catalytic activity, electrical conductivity, and other functionalities, are of great interest to smart and functional polymer fields. However, it was difficult to achieve the nano-dispersion of graphene layers in polymer matrixes. In addition, one drawback of cellulose is its difficulty in the processing as a solution or melt due to its close chain packing by strong inter and intra-molecular hydrogen bonds and persistent chain conformation. Therefore, to disperse graphene within the matrix of cellulose efficiently poses a major challenge in the field of functional composites. On the other hand, the manufacturing of such composites requires that graphene is not only produced in a sufficient scale but also homogeneously distributed into various matrices in order to maintain the unique properties of graphene in the composites. Preparation of graphene from graphene oxide (GO) by reduction is the most promising method for the cost-effective, large-scale production of graphene-based materials. Considering the strong aggregations of graphene sheets, furthermore, GO is also used as the starting material in place of graphene. In view of its abundant oxygen-containing groups, besides the reduction, GO also provides great opportunities to prepare various functionalized cellulose/GO composites by chemical modification. The investigations of their structure and properties offers a comprehensive knowledge of the possible interactions between graphene and cellulose to tailor the performance of composites based on them.

As shown in Fig. 1.1, the main purpose of this work is to produce multifunctional and smart materials based on cellulose and graphene by a simple, environmentally friendly, low cost, and efficient method. Till now, in order to obtain a uniform dispersion in which graphene could interact with cellulose matrix in nano-scale level, some special solvents for cellulose, such as ionic liquids and lithium chloride /N, N-dimethylacetamide, were also used for preparation of cellulose/graphene composites. However, the solvents are either expensive or not commercially available. New routes to fabricate cellulose/graphene composite in a more economic and environmentally friendly process need to be developed. There is no report to use the cellulose/GO hydrogel as the starting material and a novel platform for the preparation of various functionalized cellulose/GO composites by chemical modification. More specifically, the first aim is to develop cellulose/graphene nanocomposite films and aerogels for the multifunctional sensing applications by dissolving cellulose and dispersing GO homogeneously in alkaline-urea aqueous solution followed by in-situ chemical reduction of GO. In the first section of this study, the cellulose/graphene composites are fabricated and investigated as multifunctional sensors responding to different external stimuli, such as humidity, temperature, stress/strain, liquids and vapours. The temperature sensitivity and reproducibility of cellulose/graphene composites under two temperature sweeps were studied. The sensitivity of experimental humidity and the detection of human exhaled breath were also investigated. Besides, the cellulose/graphene films attached on the surface of human skin were used as strain sensors to capture, record, and distinguish different signals of human muscle motions. The sensitivity and recovery of cellulose/graphene films as sensor for different liquids, different water temperature, and water with different contents of salt was also studied. Furthermore, the vapour sensing performance of cellulose/graphene aerogels was studied based on the change of electrical resistance in cyclic exposure to a series of vapours such as acetone, ethanol, water, methanol, and others. The influences of

graphene contents, vapour types, and vapour concentrations on the change of electrical resistance were also tested.

The second aim is to prepare cellulose/GO/Fe₃O₄ hydrogels by co-precipitating iron salts onto cellulose/GO hydrogels in a basic solution for the removal of acid orange 7 (AO7), which is a major water pollutant from textile production. In this part of the study, the formation of Fe₃O₄ on the cellulose/GO hydrogel was characterized by transmission electron microscope (TEM), X-ray diffraction (XRD), Fourier-transform infrared (FTIR), and X-ray spectroscopy (XPS). The operational conditions of AO7 removal were evaluated and modelled as a function of initial AO7 dye concentration, temperature, pH, and the initial concentration of H₂O₂. The catalytic activity and stability of different composites over 20 consecutive cycles of removal of AO7 were performed by means of UV-vis spectroscopy and XPS.

The third aim is to fabricate cellulose/graphene/Fe₃O₄ aerogels for electromagnetic interference (EMI) shielding applications by an efficient, environmentally friendly, and scalable co-precipitation method. In this part, the electrical conductivity and magnetic properties of cellulose/graphene/Fe₃O₄ aerogels were determined and compared with cellulose/graphene/Fe₃O₄ films. Then, the influence of graphene content and composite thickness on the EMI shielding effectiveness (SE) was studied. The detailed EMI shielding mechanism is also investigated.

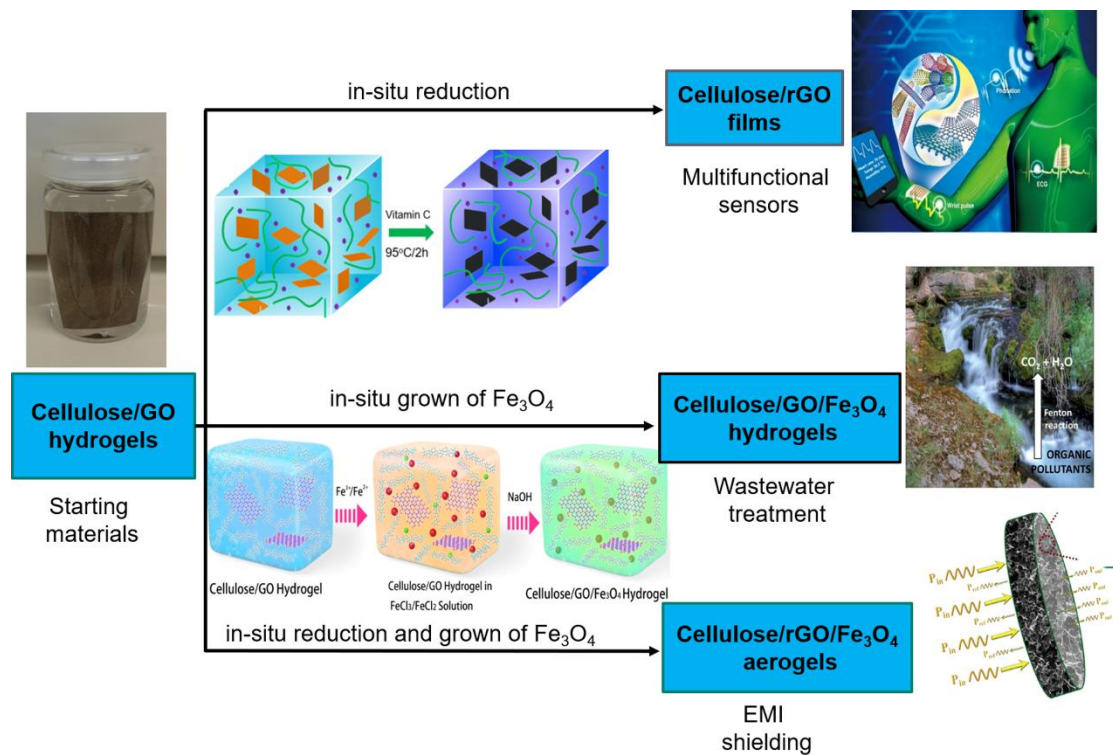


Fig. 1.1 Schematic representation of the three purposes of this study.

2. Introduction

2.1. Cellulose

Cellulose was first defined as the molecular formula of $C_6H_{10}O_5$ and first used by French chemist Anselme Payen. As the most abundant and inexhaustible biopolymer in nature, cellulose is widely present in various forms of biomasses, such as trees, plants, tunicates and bacterias, and it finds applications in many areas of modern industry. It has fascinating structure and many attractive properties such as renewability, availability, non-toxicity, low-cost, environmental friendliness, biocompatibility, biodegradability, thermal and chemical stability, and derivatizability. However, cellulose is difficult to process in water and common organic solvents, due to the formation of a strong hydrogen-bonding network formed by the intra- and inter-molecular hydrogen bonds, as shown in Fig. 2.1. For dissolving cellulose, new and efficient environmentally friendly solvent systems, such as alkali/urea aqueous solution [1-4], N-methylmorpholine-N-oxide hydrate (NMMO) [5], ionic liquids (ILs) [6-8], and LiCl/N,N-dimethylacetamide (DMAc) [9, 10] were used to break the hydrogen bonding network and to prepare regenerated cellulosic composite materials. In general, cellulose functioned as the raw material has two main application approaches. On the one hand, cellulose from cotton and wood is mainly used in building materials. On the other hand, cellulose, as the starting platform, has been widely applied in the fabrication of cellulose-based composites. Cellulose can be extensively derivatized and so forms strong and stable stiff-chain homomolecular structures with film- and hydrogel-forming properties, which have the potential to be a stable and robust carrier, matrix or scaffold component for the fabrication of various functional materials [11-17]. The development of nanostructured inorganic materials in the form of nanotubes, nanowires, and nanocrystals supplies a range of functional fillers for integration into the cellulose matrix [18-25]. Among them, nanocarbons such

as graphene have unique structural and mechanical, electrical, thermal, and optical properties.

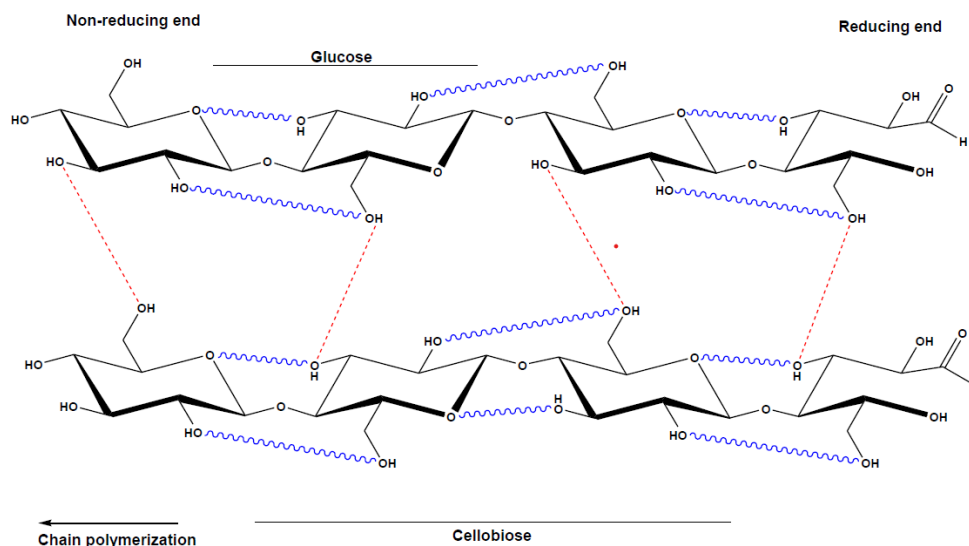


Fig. 2.1 Schematic diagram of intra- and inter-molecular hydrogen bonds in cellulose.

Reused with permission from MDPI. [26]

2.2. Graphene

Graphene is an interesting two-dimensional carbon allotrope that attracted considerable research interest because of its outstanding mechanical properties, chemical stability, superior electrical conductivity, and EMI shielding properties [27-30]. So far, various device/material applications, such as light-emitting diodes (LED), solar cells, smart phones and windows, supercapacitors, and lithium ion batteries have been reported [31]. As we all know, the processability and/or the solubility in a suitable solvent are the first topics for possible fabrication and application of functional and smart materials based on graphene. Until now, chemical modification of graphene has focused on improving the interactions with the matrix polymers and enhancing the processability and solubility in water and organic solvents [32-36]. However, functional and smart composite materials that combine the

functionalized material with the excellent performance of graphene remain mostly undeveloped.

Hence, to fabricate multifunctional graphene-integrated cellulose materials, which combine the specific properties of graphene and the characteristics of cellulose, is of great interest to polymeric science. However, it is difficult to achieve the nano-dispersion of graphene layers in polymer matrixes. In addition, cellulose cannot be easily dissolved in common solvents or impossibly be melted due to its strong inter and intra-molecular hydrogen bonds. The practical application of graphene is severely restricted by their poor dispersion and secondary aggregation in the dispersion and mixing process, bringing about the hardship to preserve their superiority. Several approaches have been developed to obtain graphene, including micromechanical exfoliation of graphite, chemical vapour deposition, reduction of GO, etc. [37-40]. Among them, preparation of graphene from GO reduction is the most promising method for the cost-effective, large-scale production of graphene-based materials. Considering the strong aggregations of graphene sheets, furthermore, GO is also used as the starting material in place of graphene. The fabrication of cellulose/GO composite by using special solvents was reported recently [41, 42]. Although the presence of GO enhanced the thermal and mechanical properties of cellulose-based materials, a lack of electrical conductivity limits their practical applications. Thus, it is required to realize the reduction of GO during the compositing process, which not only can simplify the fabrication procedures for graphene-filled nanocomposites but also prevent the undesired aggregation of reduced GO [43]. There are mainly two effective reduction techniques, chemical reduction and thermal reduction, which were used for reduction of GO [44-46]. However, how to reduce GO in cellulose matrix efficiently while preserving the mechanical properties simultaneously, is still the main challenge for the preparation of electrically conductive materials from cellulose/GO composites.

In view of the unique structure of graphene and abundant oxygen-containing groups of GO, the cellulose/graphene composites could be applied for various applications, such as water treatment field, EMI shielding field, sensors, supercapacitors, electrochemical and photothermal device.

2.3. Green solvents for cellulose/graphene nanocomposite materials

In order to fabricate functional and smart cellulose/graphene composite materials, which combine the characteristics of cellulose and the advantages of graphene, many studies have been carried out. However, it was difficult to achieve the nano-dispersion of graphene layers in polymer matrixes. How to disperse graphene within the matrix of cellulose efficiently, therefore, poses a major challenge in the field of functional bio-composites. Ordinarily, the regeneration of cellulose can be achieved by the following two methods: the physical dissolution in a suitable solvent and chemical derivatization. The physical dissolution in a suitable solvent is much cheaper and simpler for the regeneration of cellulose than the chemical derivatization. Some solvents such as ionic liquids (ILs), NaOH/urea aqueous solution, N-methyl morpholine-N-oxide (NMMO), lithium chloride (LiCl)/N, N-dimethylacetamide (DMAc), and other solvents are reported as direct solvents for the shaping and regeneration of cellulose.

2.3.1. Ionic liquids

In recent years, ILs have been used as green and effective solvents for cellulose, which attributed to their excellent chemical and thermal stability, low melting point, low flammability and good miscibility in combinations with other solutions [6]. ILs are commonly known as salts in the liquid state and composed of inorganic anions and organic nitrogen-containing inorganic cations [47].

As shown in Fig. 2.2, the formation of electron donor-electron acceptor (EDA) complexes is beneficial for the interaction of cellulose and ILs, and thereby bring about

the dissolving of cellulose in ILs [48]. For example, during the dissolution process, the oxygen and hydrogen atoms of cellulose-OH function as electron donor and acceptor. Correspondingly, the cations and anions of ILs serve as electron acceptor and donor center. Thus, the interaction of cellulose and ILs leads to the destruction of hydrogen bonds within the cellulose and procure the dissolution of cellulose.

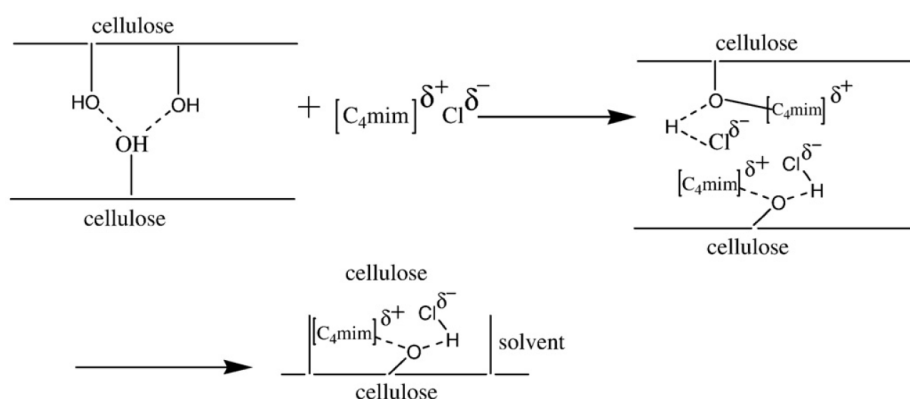


Fig. 2.2 Schematic illustration of dissolving mechanism of cellulose in ionic liquids $[C_4mim]Cl$. Reused with permission from Royal Society of Chemistry. [47]

In 2002, Swatloski et al. [7] found that cellulose could be dissolved in the ionic liquid 1-butyl-3-methyl imidazole chloride ($[C_4mim]Cl$), which opened up new paths for the development of a class of cellulose solvent systems. Recently, various ILs have been reported as cellulose solvents to fabricate the cellulose/graphene composite. GO widely acted as the precursor for the fabrication of the cellulose/graphene composites in the ILs [49-52]. For example, Peng et al. [53] prepared cellulose/rGO composite papers in 1-butyl-3-methylimidazolium chloride (BmimCl) solution. The resultant composite papers showed the excellent performance of mechanical flexibility. Zhang et al. [54] demonstrated that GO can be chemically reduced by hydrazine monohydrate with cellulose in 1-allyl-3-methylimidazolium chloride (AmimCl). The fabricated cellulose/rGO composite films exhibited enhanced stiffness.

Moreover, cellulose/graphene composite also can be obtained by using directly exfoliation of graphite in ILs. Ionic liquids are ideal green solvents for the exfoliation of graphite, for reasons that the imidazolium structure of ILs are favorable for conjugation with π electrons of graphite and the high surface tension of ILs are suitable for the exfoliation of graphite [55-57]. It is noted that cellulose exhibits a special affinity for graphite [58]. Given the abundant hydroxyl groups in cellulose, cellulose may stabilize graphene sheets by forming hydrogen bonds. Notably, cellulose can be dissolved well in ILs without any modification. Therefore, it provides the possibility to exfoliate graphite in ILs with cellulose and the cellulose-ionic liquid complexes acted as exfoliating agent. Fig. 2.3 shows the proposed formation mechanism of cellulose/graphene composite [59]. First of all, when cellulose dissolute in ILs, the hydrogen bonds in cellulose were destroyed. At the same time, the new bonds between the chloride in [Bmim]Cl and hydrogen atoms of hydroxyl in cellulose were formed [60]. Then, the liquid jet permeates through the bubbles and attacks cellulose and graphite through ultrasonication. Subsequently, the solvate complexes containing cellulose exfoliated the graphite into graphene due to the decrease of van der Waals forces between the graphite under the influence of the liquid jet and bubbles. Afterward, the solvate complexes penetrated into the graphite interlayers and acted as exfoliating agent. Finally, the hydrogen bonds of cellulose were regenerated. Cellulose as a stabilizing agent was reformed on the surface of graphene sheets. Therefore, the resultant graphene sheets were uniformly dispersed within the cellulose matrix.

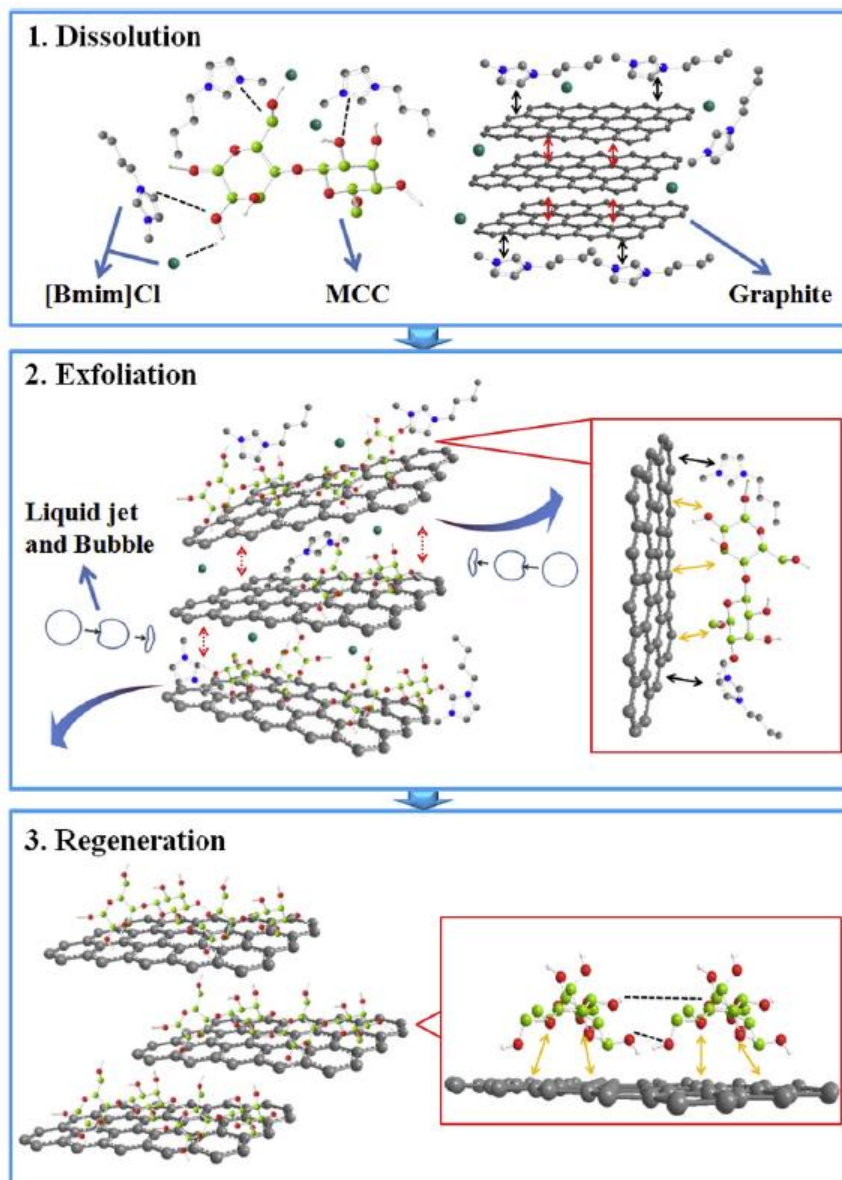


Fig. 2.3 Schematic generation of cellulose/graphene composite in ILs. Reused with permission from Elsevier. [59]

2.3.2. NaOH/urea aqueous solution

NaOH/urea aqueous solution have been one focus of cellulose solvents due to that the solution can lead to a simple, low cost, and environmentally friendly processes for dissolving cellulose. Generally, cellulose can only be dissolved in 7-9 wt.% NaOH aqueous solution at low temperature. NaOH can penetrate into the amorphous area of cellulose, where it destroys intermolecular hydrogen bonds. However, it is found that

only cellulose with lower molecular weight could be dissolved in such solution, limiting the mechanical properties and processing of cellulose products. The development of new solvents for cellulose is essential for successful and various applications of cellulose. Notably, urea can also break intermolecular hydrogen bonds of cellulose and avoid the aggregation of cellulose [61]. The addition of urea or thiourea to NaOH solution can be beneficial for cellulose solubility. In the recent years, Zhang et al. [61] found that NaOH/urea aqueous solution can dissolve cellulose more efficiently than the NaOH/H₂O system. For instance, cellulose could be totally dissolved in the new solvent, a 7 wt.% NaOH/12 wt.% urea aqueous system, within a few minutes. The most important advantage of this solvent is its low-cost and the rapid cellulose dissolution. More importantly, the NaOH/urea aqueous solution is able to entirely dissolve cellulose with relatively high molecular weight, which can broaden the application of cellulose. Similarly, Lithium hydroxide (LiOH)/urea aqueous solution can also rapidly dissolve cellulose. Fig. 2.4 describes the dissolution of the cellulose in NaOH/urea and LiOH/urea aqueous solutions [62]. In Fig. 2.4 (a), when cellulose is added into the NaOH/urea or LiOH/urea aqueous solution at -10 °C, cellulose is surrounded by free water, alkali hydrates and urea hydrates. As shown in Fig. 2.4 (b), free water, alkali hydrates, and urea hydrates can permeate the cellulose matrix and then lead to the destruction of the intra- and inter-molecular hydrogen bonds. Fig. 2.4 (c) displays that free water, alkali hydrates, and urea hydrates, which act as overcoat enveloping the cellulose chains. Therefore, cellulose molecules are uniformly dissolved in the NaOH/urea or LiOH/urea aqueous solution forming a transparent solution. Moreover, a series of regenerated cellulose products such as cellulose films, fibers, and aerogels [63-65] have been fabricated from cellulose dopes based on aqueous alkali solvents.

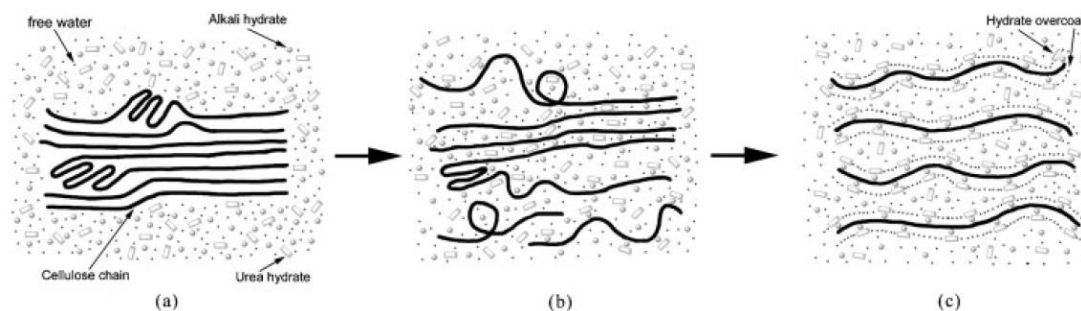


Fig. 2.4 Schematic illustration of dissolving mechanism of cellulose in NaOH/urea and LiOH/urea solutions. Reused with permission from Wiley-VCH Verlag. [62]

Recently, GO has attracted much attention because it can serve as a possible intermediate for manufacture of graphene. The sufficient amount of oxygen-containing functional groups in GO, such as hydroxyl, carboxyl, and epoxy groups, make it easily dispersible in water and aqueous alkali solvents. GO has been widely used as precursor for the preparation of the cellulose/graphene nanocomposite based on aqueous alkali solvents. Therefore, NaOH/urea aqueous solution provides a low-cost and “green” platform for regeneration of cellulose and fabricating the cellulose/graphene nanocomposites.

Nanocomposites of GO with cellulose can be fabricated by solution mixing, as long as aqueous alkali solvents that can dissolve cellulose and disperse GO sufficiently, are used. Huang et al. [66] found that GO was fully exfoliated in cellulose using NaOH/urea as a solvent. As a result, the barrier properties of the cellulose/GO film were improved and the permeability coefficient of O_2 were reduced. Green aerogels can also be prepared with GO and cellulose using NaOH/thiourea as a solvent, followed by gelation and freeze drying. Young’s modulus and the compression strength increase significantly, since the well dispersion of GO accelerated the gelation process and induced strong interactions with cellulose. The nanocomposite film also can be prepared with cellulose and GO in aqueous LiOH/urea solution followed by

coagulation in ethanol [67]. The mechanical properties of cellulose films were also drastically improved.

2.3.3. N-methyl morpholine-N-oxide

N-methyl morpholine-N-oxide, commonly known as NMMO, is widely used as a non-derivatizing solvent and able to dissolve high contents of cellulose. The whole NMMO procedure can be considered as a physical process. In 1939, Greanacher et al. [68] firstly reported the dissolution of cellulose in tertiary amine oxides. About 20 years later, Johnson et al. [69] patented a series of solvents based on cyclic tertiary amine oxides, especially NMMO. The main advantage of NMMO solvents is that NMMO can dissolve many polymers including cellulose. Moreover, the rapid technical break-through of NMMO solvents brings about the innovation in handmade cellulose fibers. Overall, the NMMO process is a relatively environmentally friendly, simple and resource preserving method to prepare regenerate cellulose.

Due to the effective dipole moment of N-O, NMMO can dissolve cellulose without derivatization or cell activation as depicted in Fig. 2.5 [70]. Although the NMMO process is well established nowadays, there is still a considerable lack of understanding the mechanism for the dissolution of cellulose in NMMO. Generally, it is well agreed upon that the solvation power of NMMO could result from its ability to disrupt intermolecular hydrogen bonds of cellulose, and to form solvent complexes by forming new hydrogen bonds between cellulose molecules and the solvent. The oxygen in NMMO can form hydrogen bonds with nearby hydroxyl groups in cellulose as well as graphite (and graphene) oxides. Thus, well-dispersed graphite oxides or graphene oxides in cellulose and strong physical hydrogen bonds between cellulose matrix and filler can be expected. Therefore, environmentally friendly NMMO monohydrate is suitable for dissolving cellulose and dispersing GO to prepare the cellulose/GO composites.

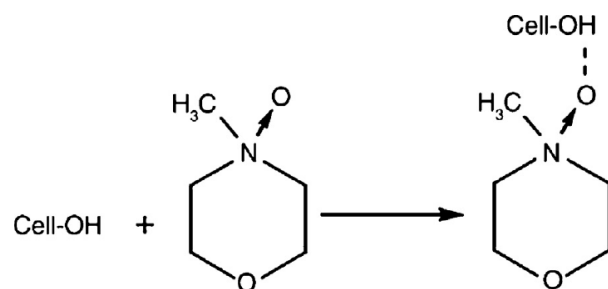


Fig. 2.5 Schematic illustration of dissolving mechanism of cellulose in NMMO. Reused with permission from Elsevier. [70]

Recently, Kim et al. [41] used NMMO monohydrate as the solvent to disperse GO and dissolve cellulose. Due to the effective dipole moment of N-O, the solvent can dissolve cellulose without derivatization. The strong and efficient interaction between NMMO and GO increases the viscosity of the resultant composites, and thereby enhances the thermal and mechanical performance. Zhou et al. [71] reported the successful fabrication of cellulose/GO aerogels with NMMO as an environmentally friendly and nontoxic solvent. The uniform dispersion of GO in cellulose matrix enhanced the thermal stability.

2.3.4 Other solvents for cellulose/graphene composites

2.3.4.1 LiCl/DMAc

LiCl/DMAc is a direct and environmentally friendly solvent for dissolving of different cellulose types [72]. The widespread use of this solvent is attributed to the fact that LiCl/DMAc solvent is colorless and able to molecularly dissolve cellulose without obvious degradation even in case of high molecular weight at room temperature [73]. Though the dissolution mechanisms for cellulose in LiCl/DMAc have been insufficiently clarified, it is generally accepted that Li^+ links to the solvent carbonyl leaving Cl^- as an efficient nucleophile that can break the hydrogen bonds of cellulose [74, 75]. Fig. 2.6 shows the dissolution mechanism of cellulose in LiCl/DMAc [76]. When cellulose is added into the LiCl/DMAc cosolvent system, the cellulose-OH strongly forms

hydrogen bonds with the Cl^- , during which the intra and inter-molecular hydrogen-bonding of cellulose is broken with simultaneously splitting the $\text{Li}^+\text{-Cl}^-$ ion pairs. Simultaneously, free DMAc molecules in this cosolvent system surrounded and solvated Li^+ to meet the electric balance. Therefore, cellulose could be dissolved in this LiCl/DMAc cosolvent system on molecular level to form a homogeneous cellulose solution.

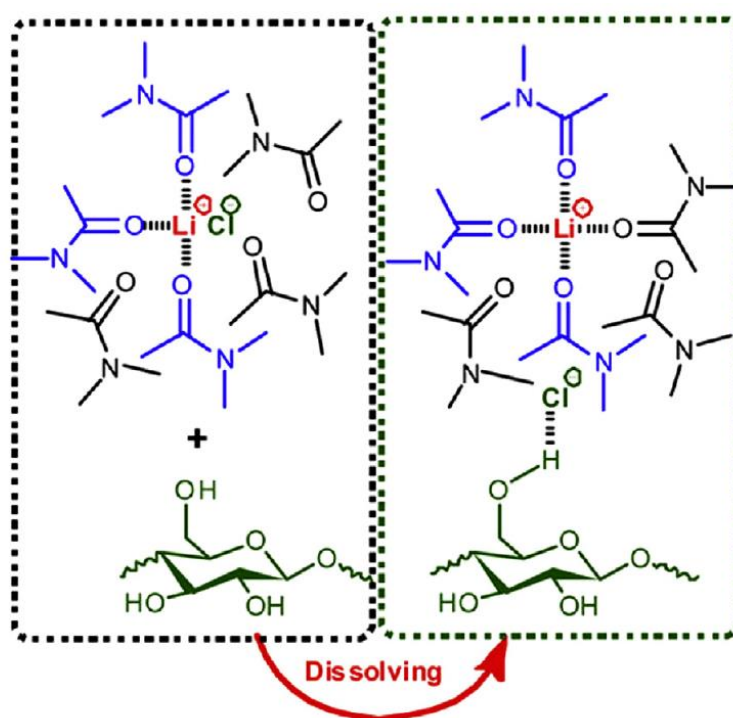


Fig. 2.6 Schematic illustration of dissolving mechanism of cellulose in LiCl/DMAc solution. Reused with permission from American Chemical Society. [76]

Recently, Zhang et al. [77] reported the fabrication of cellulose/graphene composite films through dispersing graphene and dissolving cellulose in LiCl/DMAc solution. The strong interaction between cellulose and graphene by hydrogen bond is beneficial for the good dispersion of graphene sheets in cellulose matrix. Therefore, the cellulose/graphene composite films displayed an obvious enhancement on mechanical, thermal, and electrical conductivity properties.

2.3.4.2 *N*-methyl-2-pyrrolidone (NMP)

It is well known that the presence of oxygen-containing groups in graphene oxide renders it strongly hydrophilic and water soluble. Meanwhile, the good dispersion performance of GO in other organic solvents, such as tetrahydrofuran (THF), ethylene glycol (EG), NMP, and dimethylformamide (DMF), has been reported.

Similar to LiCl/DMAc, the combined use of NMP and LiCl can also be applied in dissolving of cellulose. Recently, NMP has been widely employed as a starting solvent applied in agricultural chemicals, coatings, and wood dissolution. For example, Eberhardt et al. [78] used a solvent system based on LiCl in NMP to assess the merits of partial dissolutions of wood samples. With the combined use of NMP and LiCl, an obviously enhanced dissolution of wood can be achieved. Weng et al. [24] reported a scalable and simple method to prepare cellulose/graphene composite membranes. The fabrication of cellulose/graphene composite membranes is shown in Fig. 2.7. First of all, graphene nanosheets (GNS) was added and dispersed in NMP. The graphene solution was achieved after the sonication and centrifugation. Secondly, the graphene solution was vacuum filtered by a filter paper. During the process, the color of graphene solution changed from black to colorless. Finally, the different shapes of cellulose/graphene composite membranes were achieved after vacuum drying.

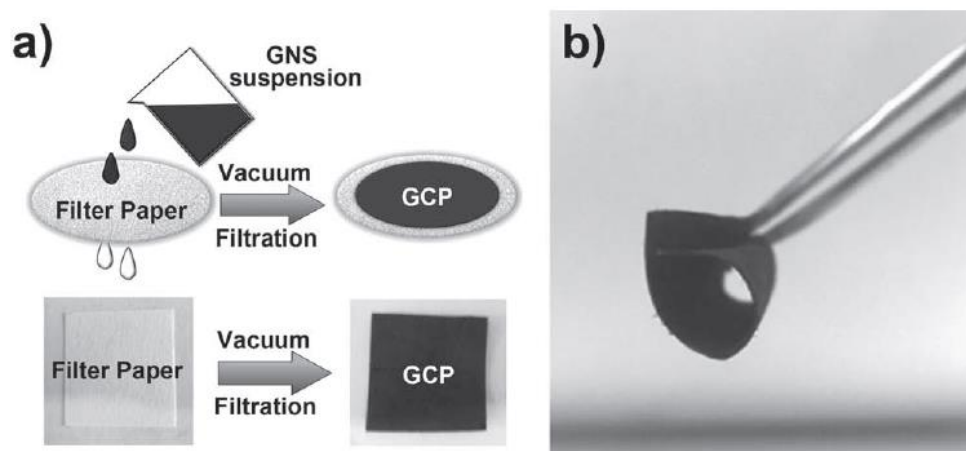


Fig. 2.7 (a) Schematic illustration of the preparation of cellulose/graphene composite membranes. (b) The digital image of cellulose/graphene composite membrane indicates the flexibility of the membrane. Reused with permission from Wiley. [24]

2.4. Cellulose/graphene composites

Cellulose as a polymeric raw material has been widely used in two general fields: cellulose has been used as constructing materials based on cotton, wood, paper and board. In addition, cellulose also has been used mainly as a starting material for fabricating various functional and smart composite materials by mixing cellulose with an inorganic/organic material with specific functionalities in an appropriate solvent. Graphene with an atomically thin, two-dimensional structure, exhibits remarkable electronic, mechanical, optical, and thermal properties. For combining the excellent performances of graphene and the characteristics of cellulose, several attempts to fabricate cellulose/graphene composite have been reported, including films, membranes, fibers, hydrogels, and aerogels. Some solvents such as NaOH/urea solution, ILs, NMMO, and LiCl/DMAc were used for both dispersing of graphene and dissolution of cellulose, in order to obtain a uniform dispersion in which graphene interact with cellulose in nano-scale level. On the one hand, the cellulose/graphene composites display excellent mechanical strength, improved thermal properties and good electrical properties, due to the excellent performance of graphene and well-dispersion of graphene in cellulose matrix; On the other hand, in view of the unique structure of graphene and abundant oxygen-containing groups of GO, the cellulose/graphene composites could be applied for various applications, such as water treatment, EMI shielding, sensors, supercapacitors, and electrochemical and photothermal devices.

2.4.1 Cellulose/graphene composite films and membranes

Transparent cellulose films are produced mainly by the viscose process and cuprammonium method, which are still important roles for packaging applications, food casing, cosmetics, and pressure sensitive tapes. Compared with the cellulose films, the cellulose/graphene composite films with the incorporation of graphene exhibit enhanced properties, such as good electrical conductivity properties, increased thermal properties and excellent mechanical strength. Moreover, graphene and GO endow the cellulose film materials with various functions, extremely broadening their applications in different fields.

2.4.1.1 Cellulose/graphene derivatives composite films with enhanced properties

Large area graphene and GO endowed enhanced mechanical and thermal properties to composite films. Several ILs have been used to prepare composites of cellulose with graphene. Regenerated cellulose/reduced graphene oxide nanocomposites have been prepared by a green and simple method based on the solvent of 1-allyl-3-methylimidazolium chloride (AmimCl) [54]. Notedly, the addition of a small amount of reduced GO could significantly decelerate the dissolution of cellulose in AmimCl. Thus, this provided a simple method to control the mechanical and thermal properties by changing the dissolution time. Fig. 2.8 displays the mechanical properties of cellulose/reduced GO composite films and cellulose film. The tensile strength and the strain at break of cellulose/reduced GO composite films increase obviously, compared with the pure cellulose films. For example, composite film prepared with dissolution time of 4 h exhibits about 390 % increase in strain at break and about 11 % increase in tensile strength, respectively.

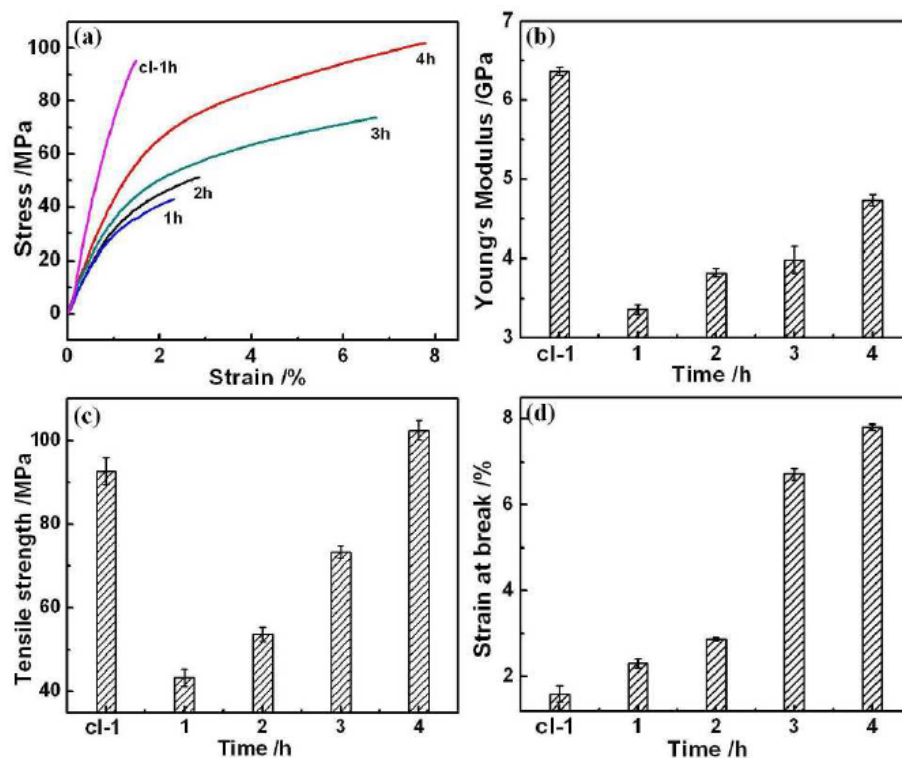


Fig. 2.8 Mechanical properties of different cellulose/graphene composite and cellulose films with different dissolving time. Reused with permission from American Chemical Society. [54]

NMMO is an environmentally friendly solvent for cellulose and an excellent dispersing agent for GO. Kim et al. [41] used NMMO monohydrate solvent to prepare the cellulose/GO composite films. As expected, NMMO and GO interacted strongly and the rheological properties, mechanical properties, and thermal properties of the composite films were improved, even with a small amount of GO. In addition, thermal annealing of the cellulose/GO composite films removed the oxygen groups of GO and endowed the composite films to the electrical conductivity.

The aqueous solvent systems also have great potential to fabricate many functional cellulose composites. The cellulose/GO composite films were prepared by adding GO and cellulose in LiOH/urea solvent followed by coagulation in ethanol [67]. Fully exfoliated GO were added into cellulose matrix and randomly dispersed in cellulose by a facial method. Physical interactions between cellulose and GO were confirmed using XRD, XPS, and Raman. Even with only a small amount of GO, the

composite films exhibited three times greater elongation at break and a 120 % improvement in the tensile strength compared with the pure cellulose film. It has been confirmed that cellulose also could be well dissolved in NaOH/urea aqueous solution at low temperature [79]. Regenerated cellulose/GO composite films have been fabricated in NaOH/urea aqueous solution by a green and simple method. The structure, thermal stability, and mechanical properties of these composite films have been investigated by wide-angle X-ray diffraction, scanning electron microscopy, thermal analyses, and tensile strength measurements. The results obtained from those different studies revealed that cellulose and GO are mixed homogeneously. The thermal stability and mechanical properties of the composite materials are improved significantly over those of pure cellulose. The cellulose/GO film showed a high storage modulus up to 180 °C. The effect of the amount of GO content in the composite material has also been investigated.

Another solvent used for dissolving cellulose and dispersing graphene or GO is LiCl/DMAc. Cellulose/graphene films can be obtained by mixing solutions of both cellulose matrix and graphene in LiCl/DMAc, exhibiting strong interactions between the polar groups of the two components [77]. These interactions provided the nanocomposite films with enhanced mechanical and thermal properties, as well as improved electrical conductivity. Especially, the nanocomposite with 1.6 wt.% graphene had a Young's modulus of 7.2 GPa, thus it is increased by 110 % compared to 3.4 GPa of neat cellulose, and the tensile strength of the composite is 148 MPa, corresponding to an increase of 66% compared to 89 MPa of neat cellulose.

Apart from their common solvents for dissolving cellulose and dispersing graphene or GO, there are also many method and suitable solutions to prepare the cellulose/graphene composite films with enhanced properties. For example, Luong et al. [80] fabricated the cellulose/graphene composite film with excellent electrical and mechanical properties by adding graphene into the amine-modified nanofibrillated

cellulose. With the addition of only 0.3 wt.% graphene, the resultant cellulose/graphene composite film can reach the electrical percolation with an electrical conductivity of $4.79 \times 10^{-4} \text{ S m}^{-1}$. Moreover, the tensile strength of cellulose/graphene composite film also obviously improved with addition of 0.3 wt.% of graphene, compared with graphene oxide and cellulose film. Furthermore, the elongation at break of the composite cellulose/graphene (8 wt.%) composite film is much higher than that of graphene oxide film. Secor et al. [81] reported high conductivity and inkjet-printed graphene patterns based on the platform of ethyl cellulose for flexible electronics. The graphene ink is fabricated by solution-phase exfoliation of graphene in ethanol and ethyl cellulose. The graphene/ethyl cellulose composite shows tolerance to bending stresses, which allow the composite applied in a wide range of flexible and printed electronic fields.

Nanocrystalline cellulose (CNC), the nanoscale derivatives of cellulose, has attracted more and more attention due to its special properties and unique structure. Valentini et al. [42] fabricated conductive CNC/GO composite films through casting GO solution onto CNC. With the addition of GO, the CNC/GO composite film exhibited electrical conductivity and enhanced wettability when the film was applied to an electric current. This result opens a simple and efficient way for the paper electronic based on GO and CNC. Wang et al. [82] prepared a strong and conductive CNC/graphene composite film by dispersing GO and CNC in water. The hot-pressing method induced the well-aligned graphene sheets. Therefore, the modulus and tensile strength of resultant CNC/graphene composite film improved by 57 % and 33%, respectively, compared with net graphene paper. Moreover, the hybrid paper also displays good thermal conductivity performance. These flexible, “green”, and low-cost CNC/graphene composite films have the potential in the application of packaging, and heat-conducting fields.

2.4.1.2 Gas permeable materials

Cellulose is considered an environmentally friendly, promising and potential substitute in protective and packaging applications, which is ascribed to the biodegradability, low-cost, and biocompatibility. However, cellulose film, as the packaging material, has a poor performance as gas barrier, which limits the use of cellulose in packaging applications. The incorporation of GO sheets into different polymeric films is beneficial for the effective enhancement of gas barrier performance, which is due to the large aspect ratio and high specific surface area of GO sheets. Huang et al. [66] reported the preparation of cellulose/GO composite film in NaOH/urea solution by an efficient, low-cost and simple method. Fig. 2.9 displays the morphology and evolution of GO sheets during the preparation of cellulose/GO composite films. Firstly, NaOH and urea easily damaged the intra- and intermolecular hydrogen bonding of the cellulose chains at low temperatures. Urea, water, and sodium ions formed an “overcoat” structure, surrounding the cellulose molecules and preventing the self-aggregation of cellulose molecules. Due to the strong interaction between GO sheets and cellulose matrix, GO sheets were uniformly and randomly dispersed in NaOH/urea solution. The low-viscosity of the NaOH/urea solution results in the parallel alignment of the GO sheets in the cellulose matrix, induced by gravitational forces. Secondly, stable physical crosslinking networks are formed because of the self-association of the cellulose chains. Finally, the cellulose/GO hydrogels are transformed into cellulose/GO composite films by the hot-pressing method, and the excellent alignment of GO sheets is further preserved during the processing procedure. Thus, the high orientation and well dispersion of GO sheets improved the barrier properties of cellulose composites.

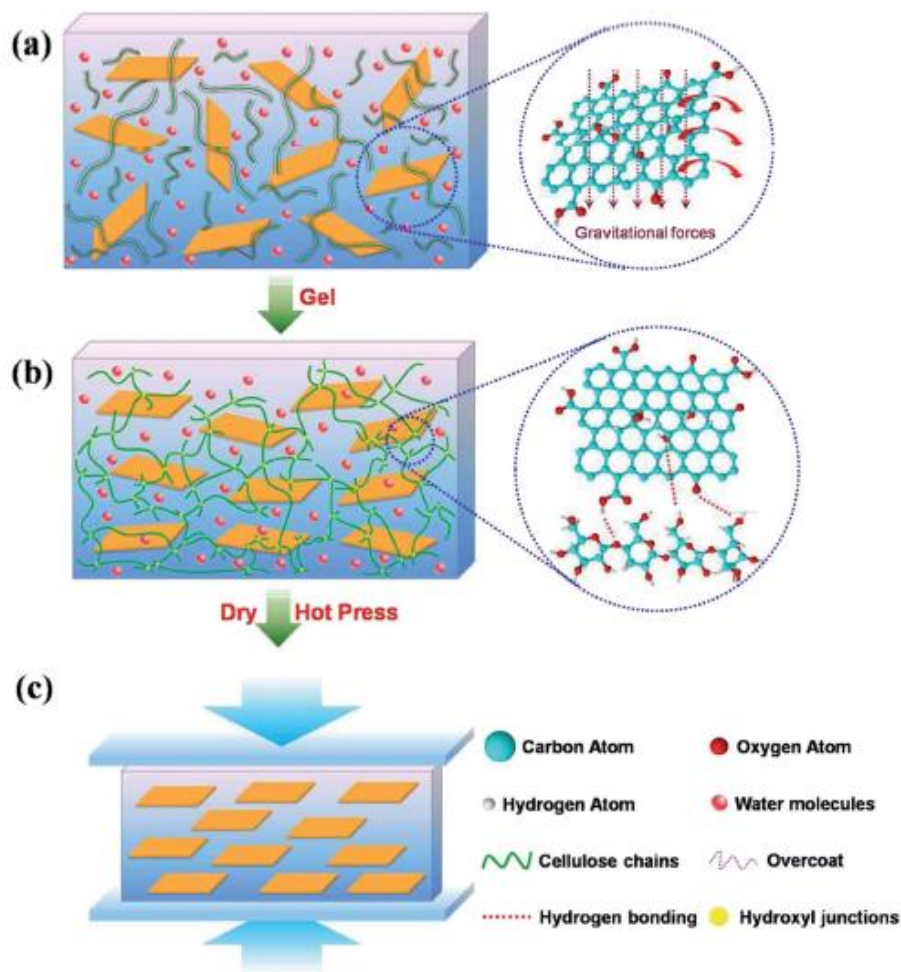


Fig. 2.9 Schematic representation of cellulose/GO composite morphology and its evolution during the fabrication of composite films. Reused with permission from Royal Society of Chemistry. [66]

2.4.1.3 Multifunctional sensor materials

In the recently years, cellulose has been considered as smart and functional materials in flexible electronics, sensors, and actuators. Graphene also have excellent electronic transport properties and high electro-catalytic activities, which make they suitable for electrochemical supercapacitors, optoelectronic devices, and multifunctional sensors, such as strain sensor, humidity sensor, wearable sensor, and gas sensor. Till now, the functional and smart cellulose/graphene composite materials

are being studied in the sensing fields. Yan et al. [83] prepared flexible and high-strain sensors based on nanocellulose and graphene. The stretchable strain sensor was achieved by embedding the flexible cellulose/graphene nanopapers in an elastomer matrix. These strain sensors exhibited high-strain and all-directional sensing performance, which is very important for the detection of human motion. As shown in Fig. 2.10, the functional nanopapers were attached on gloves to detect the finger movement. Moreover, Xu et al. [84] also prepared functional and smart sensors based on inverse opal cellulose and rGO for the detection of human movement, such as wrist bending movement, finger bending movement, different movements of the human throat, and head rotation movement as well as NaCl concentrations in the sweat, as shown in Fig. 2.11.

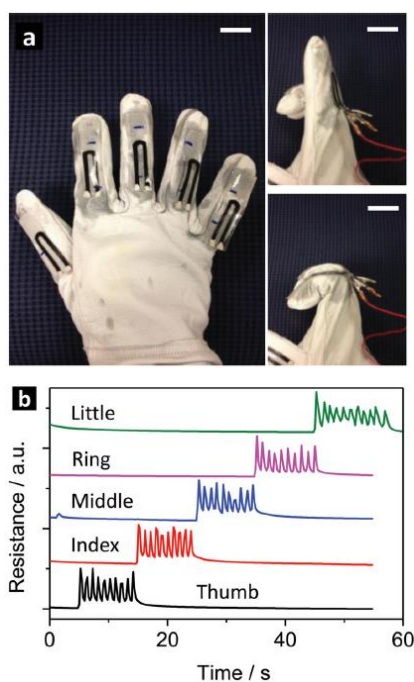


Fig. 2.10 Wearable strain sensors for the detections of finger movement. Reused with permission from Royal Society of Chemistry. [83]

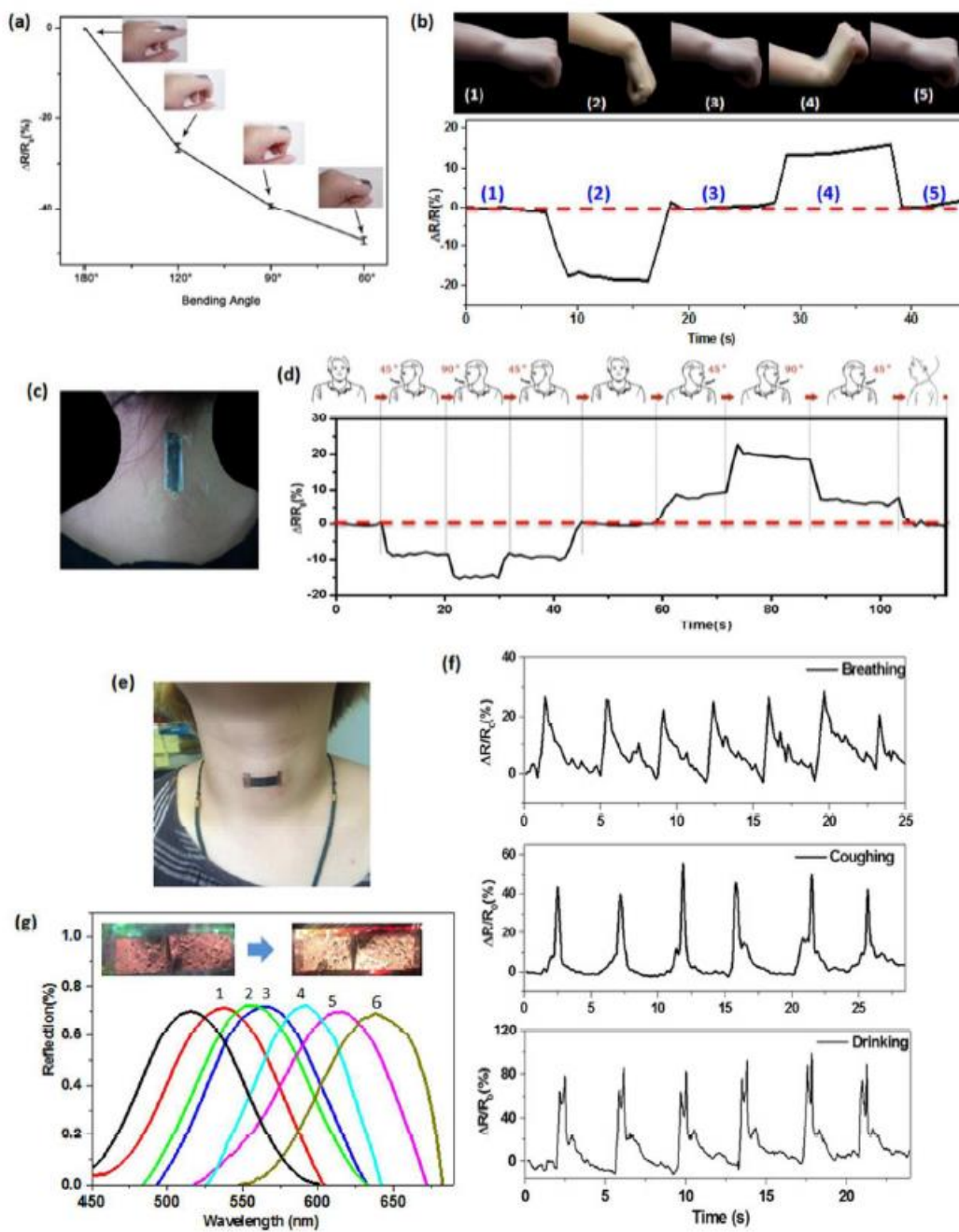


Fig. 2.11 Photograph and relative resistance change of cellulose/rGO composite film attached on various parts of body to detect different human movement and sweat. Reused with permission from Royal Society of Chemistry. [84]

Kafy et al. [85] reported the cellulose/graphene nanocomposites as liquid solvent sensor and semiconductor based on the change of surface capacitance when it interacts

with solvents. The cellulose/graphene composite film with excellent dielectric, electrical, and mechanical properties was prepared by combining cellulose with modified graphene oxide (CFGO) sheets in a well-controlled manner. The cellulose/graphene composite film displays fast response and excellent sensitivity to organic solvents. The performance as solvent sensor was also evaluated based on relative capacitance changes caused by interactions with various solvents. As shown in Fig. 2.12, the cellulose/graphene composite film is able to distinguish different organic solvents because of different relative capacitance change. The sensing ability and selectivity is explained based on solubility parameters and diffusion processes.

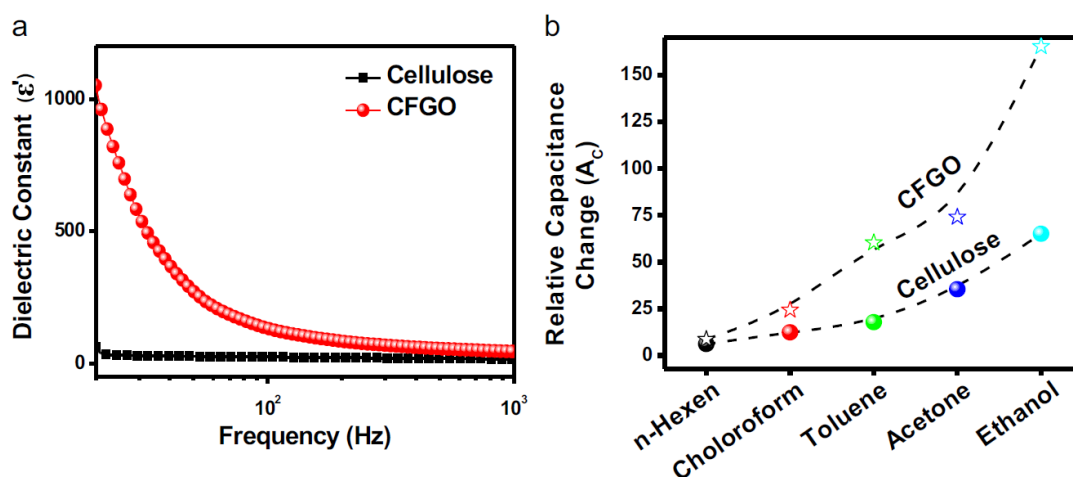


Fig. 2.12 (a) Frequencies dependency of the dielectric constant of cellulose and CFGO. (b) Relative capacitance change of cellulose/CFGO composite film caused by different solvents. Reused with permission from Elsevier. [85]

2.4.1.5 Supercapacitors

Graphene and its derivatives have demonstrated versatile feasibility for energy-storage devices and flexible electronics due to their special structure with versatile electrochemical properties and their atomic thickness. Notably, flexible

macroscopic assemblies of graphene or related polymer composites have been used as soft electrodes for supercapacitors and flexible batteries. Ouyang et al. [86] reported the successful preparation of cellulose/rGO composites by an efficient, simple, and scalable method. In this work, ball milling was applied for chemical reduction of GO. The hydrogen bond interactions between cellulose and rGO sheets and the efficient mechanical shearing of ball milling are beneficial for the enhancement of crystallinity and thermal stability of cellulose/rGO composites. As shown in Fig. 2.12 (a), the cellulose/rGO composites function as working electrodes. The cyclic voltammetry (CV) curves in Fig. 2.12 (b) exhibited ideal capacitive behavior with nearly rectangular shape, indicating excellent electrochemical performance of the cellulose/rGO composite. In Fig. 2.12 (c), the galvanostatic (GV) curve of the cellulose/rGO composite has a symmetric nature with no drop, demonstrating small mass transfer resistance, good charge propagation behavior in the 3D porous structures, rapid current-voltage response, and good electrochemical capacitive behavior. Nyquist plots of cellulose/rGO composite are displayed in Fig. 2.12 (d). The well overlap of these curves demonstrated the electrochemical stability. Fig. 2.12 (e) shows the impedance phase curve. The cellulose/rGO composite exhibited capacitive behavior with no capacitor-transition in a wide frequency range. Moreover, the high-porous network of cellulose/rGO composite with high specific surface area results in the fast charge propagation and thereby it displays suitable applications in the fields of supercapacitors, catalyst supports, and adsorption.

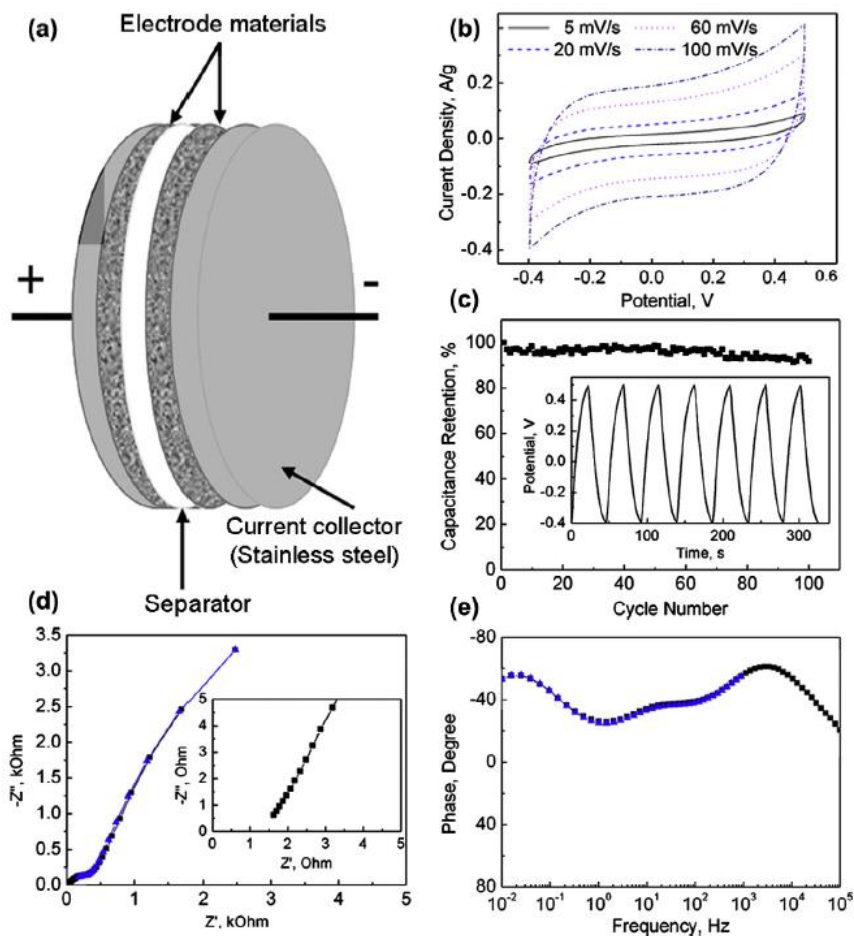


Fig. 2.13 (a) Schematic illustration of the supercapacitor device prepared by using cellulose/rGO composite film as working electrodes. (b) CV curves of cellulose/rGO composite film at different scanning rates. (c) Cycling GV charge/discharge test of cellulose/rGO composite at 150 mA g^{-1} . Inset: seven detailed continuous cycles. (d) Nyquist plots of the cellulose/rGO composite film. Inset: an expanded view of Nyquist plot. (e) Impedance phase angle plot of cellulose/rGO composite film. Reused with permission from Elsevier. [86]

2.4.1.6 Lithium sulphur batteries

As we know, the combination of amine-functionalized cellulose and reduced GO resulted in graphene nanocomposite paper with high mechanical properties and excellent electrical conductivity. Patel et al. [87] have combined graphene and cellulose in a simple and easy method to fabricate conductive and porous graphene/cellulose

composite for lithium sulphur batteries. The resultant graphene/cellulose/S composite material was used as the positive electrode for Li-S batteries. It was found that the well-designed cellulose/graphene composite material with low surface area displays excellent electrochemical performance and good stability. The nanocellulose structure functions as the matrix for the S-graphene mixture and avoids the opening of graphene fillers. At the same time, the well-dispersed graphene also prevents diffusion of lithium polysulphides into the electrolyte and ensures the good stability and long cycle life. This work demonstrates the potential application of cellulose/graphene composite as the host matrix for the Sulphur impregnation

2.4.2 Cellulose/graphene composite fibers

Cellulose /graphene nanocomposites can also be in the form of fibers, with the help of the spinning process. Tian et al. [88] prepared cellulose/graphene composite fibers by using a pilot-scale wet spinning method. The incorporation of 0.2 wt.% graphene in cellulose matrix can significantly increase the tensile strength and Young's modulus of the fiber, demonstrating the efficient load transfer between the cellulose matrix and graphene sheets. Moreover, the addition of 0.2 wt.% graphene also increases the onset decomposition temperature by 44 °C. The cellulose/graphene composite fibers display excellent performance of thermal stability and dynamic heat transfer. The cellulose/graphene composite fibers expand the application of cellulose/graphene composite in fibrous materials.

Shaya et al. [89] reported an environmentally friendly and facile method to fabricating composite fibers based on graphene nanoplatelets and cellulose. Nanocomposite fibers with nano-scale reinforcements could have potential to broaden fiber applications. The unique surface features and the high aspect ratio of graphene lead to great improvements of the nanocomposite fiber properties. The cellulose/graphene composite fibers were wet spun by using an IL solution of 1-ethyl-3-methylimidazolium acetate (EMIMAc) as solvent. The addition of graphene

into cellulose generated electrical conductivity. Moreover, the composite fibers also exhibited significant improvements in char yield and thermal stability.

Nanofibrillated cellulose (NFC) is a plentiful 1D material with a length in microscale and a diameter in nanoscale. Due to its excellent mechanical properties with an elastic modulus of ~140 GPa, NFC can be used as a building block for high strength composite materials. In addition, since this material has strong interacting surface hydroxyls, it also can act as an impressive binder/reinforcement. As we know, 2D GO nanosheets exhibit a high aspect ratio, remarkable mechanical properties, and good processability, making the GO nanosheets another possible building block for high strength microfibers. Li et al. [90] prepared the high-performance fibers by hybridizing graphene oxide and wood cellulose. Fig. 2.14 shows the structure of the NFC/GO hybrid microfibers. In the hybrid microfiber, NFC fibers and GO nanosheets align along the direction of the microfiber. Metal ions (Ca^{2+}) link GO nanosheets and the NFC together to create even tougher and stronger microfibers. These well-aligned hybrid microfibers are much stronger than microfibers composed of NFC or GO alone. Both the experimental results and molecular dynamics simulations reveal the synergistic effect between GO and NFC: the bonding between neighboring GO nanosheets is enhanced by NFC because the introduction of NFC provides the extra bonding options available between the nanosheets. In addition, NFC fibers function as 'lines' to 'wrap and weave' GO sheets together. In turn, GO sheet also function as a bridge to contact the neighboring NFC fibers, and thereby improving the performance of mechanical properties. The excellent design of mechanically strong composite fibers can be applied in high-quality building fields.

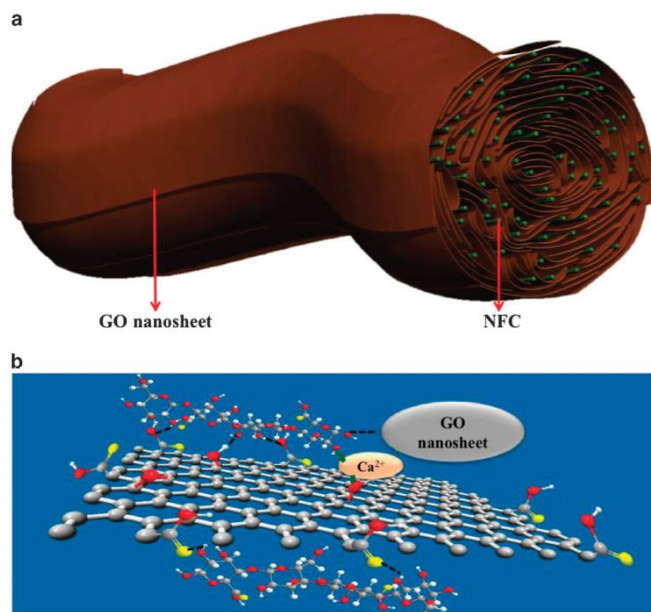


Fig. 2.14 (a) Schematic illustration of the NFC/GO composite microfiber with NFC fibers along the microfiber direction and aligned GO nanosheets. (b) The increased interaction between GO nanosheets and NFC by the addition of Ca^{2+} . Reused with permission from Nature Publishing Group. [91]

2.4.3 Cellulose/graphene composite hydrogels and aerogels

Hydrogels network structures obtained by chemical cross-linking or physical aggregation contain large amounts of retained water. Cellulose hydrogels are attracting attention in various fields such as wastewater treatment, drug delivery, sensing, and wound dressing due to their low cost, low toxicity, excellent hydrophilicity, biocompatibility, and biodegradability. However, the cellulose hydrogels suffer from the lack of mechanical performance, which limited their further product applications. Recently, by regenerating the mixture of reduced graphene oxide and wood pulp from their IL solution, highly tough cellulose/graphene composite hydrogels were fabricated [92]. Fig. 2.15 shows increased mechanical strength of cellulose/graphene composite hydrogels. ILs are efficient solvents for cellulose. Meanwhile, ILs can also disperse bulk-quantity of graphene sheets. Firstly, when the IL solution of graphene and the IL solution of cellulose were mixed together, the graphene sheets were uniformly

dispersed in the IL solution. Then, the physical hydrogels could be obtained by regenerating the solution of cellulose in water. The incorporation of graphene significantly increased the mechanical strength and thermal stability. The mechanical strength of cellulose/graphene composite hydrogels were related with the doping ratio of graphene. This green and simple method could combine the excellent performances of graphene with cellulose-based hydrogels, and hold great potential for various fields such as in energy and biology.

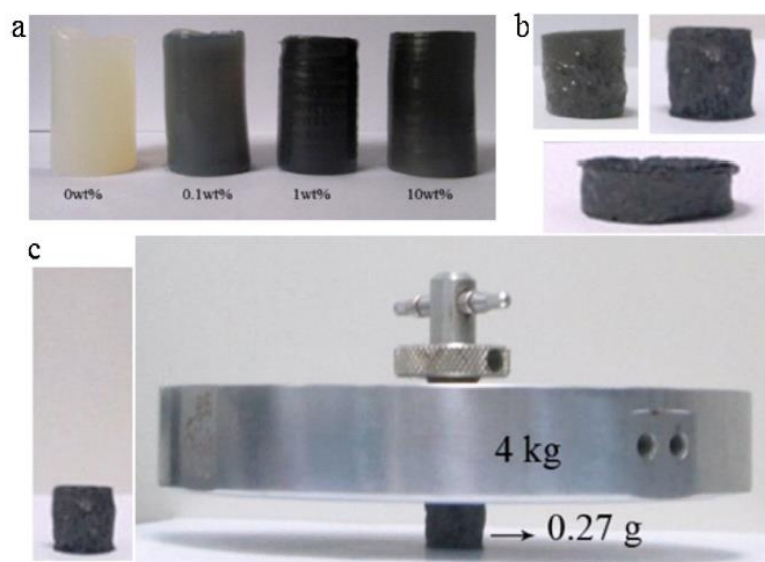


Fig. 2.15 (a) Digital images of cellulose and cellulose/graphene hydrogels, (b) Digital images of cellulose/graphene aerogels, c) Digital images of cellulose/graphene aerogels under a 4 kg counterpoise. Reused with permission from Elsevier. [92]

Furthermore, Si et al. [93] used a facile one-step in situ biosynthesis by incorporating graphene oxide into bacterial cellulose to prepare bacterial cellulose/GO nanocomposite hydrogels. The results suggested that GO were well dispersed in bacterial cellulose and that the 3D porous structure of bacterial cellulose is sustained. Compared with the pure bacterial cellulose hydrogels, the bacterial cellulose/GO (0.48

wt.%) composite hydrogels exhibit about 38 % increase in tensile strength, and 120 % increase in Young's modulus, respectively.

Apart from the application to enhance the mechanical strength and thermal stability, the cellulose/graphene composite hydrogels also can act as the precursor to prepare graphene/cellulose composite aerogels by the flash freezing/lyophilization process. Aerogels are highly porous solids consisting of ultra-high volume gas-phase fractions and three-dimensional networks of solid substrates. Because of their unique features such as ultra-low density, large open pores, and ultra-high specific surface area, inserting electrically conductive nanofillers into the aerogel is one of the most promising strategies to reduce significantly the density of EMI shielding materials. Hybrid aerogels based on cellulose and GO were fabricated by a solution mixing-regeneration-freeze drying method [94]. After the in-situ reduction of GO by L-ascorbic acid and the pyrolysis of cellulose/graphene aerogels, the resultant aerogels show excellent EMI shielding performance with the best SE_{total} of 58.4 dB, good electrical conductivity, flame retardancy, and hydrophobicity. Therefore, the cellulose/graphene composite aerogels hold an opportunity for various applications such as EMI protection, fire retardants, electrochemical devices, and waterproofing agents.

Moreover, lightweight cellulose/graphene composite aerogels are suitable as supporting network for polyethylene glycol (PEG)-containing phase change composites (PCC) due to their highly porous and strong three-dimensional networks [95]. Fig. 2.16 shows the process of the preparation of cellulose/graphene composite aerogel and PEG/cellulose/graphene composite. PEG/cellulose/graphene composite was prepared by vacuum-assisted impregnation with PEG. The strong and highly porous three-dimensional network is beneficial for the encapsulation of PEG and prevents the leakage of PEG. With addition of 5.3 wt.% graphene, the composite aerogel displays a high thermal conductivity of $1.35 \text{ Wm}^{-1}\text{K}^{-1}$, 463 % higher than the

composite without graphene. In addition, even compressed at 70 °C (upon melting point of PEG) the composite aerogel keeps their shape stable without any leakage.

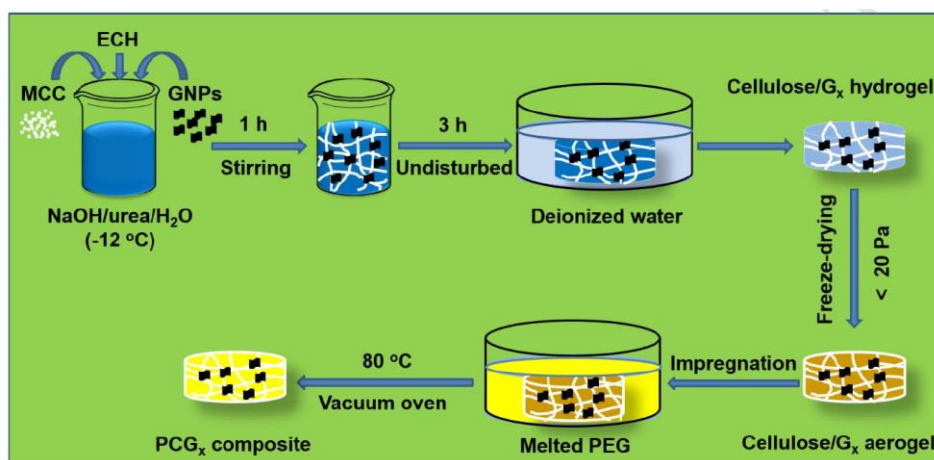


Fig. 2.16 Schematic illustration of experimental fabrication of cellulose/graphene composite and cellulose/graphene/PEG composite aerogels. Reused with permission from Wiley-VCH Verlag. [93]

Green aerogels can also be prepared with cellulose and GO by adding GO in cellulosic solution in NaOH/thiourea/H₂O, followed by gelation, solvent exchange, and freeze drying [96]. Traditionally, cellulose industries use for cellulose processing a variety of solvents that are highly toxic and produce harmful products. These include CS₂ and cuprammonium solutions, which generate heavy metal residues. NaOH/thiourea/H₂O is considered to be an environmental-friendly solvent because of the absence of volatile chemicals during the dissolution process. The presence of GO accelerated the gelation process and induced strong interactions with cellulosic chains, resulting in important increase of the compression strength and Young's modulus by 30 % and 90 %, respectively.

2.5. Cellulose/graphene-based functional materials

The presence of oxygen-containing groups in graphene oxide renders it strongly hydrophilic and water soluble, and it also provides great opportunities to prepare various functionalized GO/cellulose composites by chemical modification. In addition,

it was proved that there was a large amount of water and highly porous networks in cellulose/GO composite. Therefore, cellulose/GO or cellulose/graphene composites also have been used mainly as a precursor material for fabricating various functional composite materials by mixing cellulose/graphene with an inorganic/organic material with specific functionalities in an appropriate solvent. Thus, the fabrication of functional materials based on cellulose/graphene, which combine the unique structure and properties of nanomaterials and excellent performance of cellulose/graphene composite, are of great interest to polymer science.

2.5.1 Antibacterial activities with silver nanoparticles

Chook et al. [97] reported the preparation of an effective and porous antibacterial cellulose membrane with embedded GO-Ag particles. The as-produced GO-Ag particles were mixed into the cellulose solution and subsequently the mixture was regenerated into composite membrane by immersing in sulfuric acid solution. The introduction of GO greatly increased the mechanical and antibacterial performance of the composite membrane. Moreover, the porous structure of cellulose/GO-Ag membrane is beneficial for interaction of bacteria with Ag particles, and thereby enhances the antibacterial performance of composite membrane. The cellulose/GO-Ag membrane shows excellent antibacterial properties and has potential applications in water treatment fields.

2.5.2 Enhanced properties with poly (vinyl alcohol) (PVA)

El Miri et al. [98] introduced CNC/GO composite nanofillers into a PVA matrix to study the synergistic effect in improving the properties. Due to the synergistic effect and the strong interaction, the tensile strength, the Young's modulus, and toughness of CNC/GO/PVA composites were significantly improved, compared with pure PVA. The presence of CNC improved the dispersion of GO sheets in the PVA matrix and avoided the agglomeration of GO sheets, and thereby obviously improved the mechanical performance.

2.5.3 Photocatalysts with Cu₂O

Tu et al. [99] introduced Cu₂O into cellulose/GO composite for the fabrication of visible-light photocatalysts through an efficient and simple method. The in-situ generation and well dispersion of Cu₂O in the porous cellulose matrix provides free photoelectrons and electron holes and is beneficial for the high performance in methyl orange photodegradation. Furthermore, the introduction of GO sheets also improved the performance in photodegradation of methyl orange and enhanced the photodegradation rate. The cellulose/GO/Cu₂O composite films used as the photocatalysts can be easily reused and recycled, showing another advantage in the application in the wastewater treatment fields.

. Till now, in order to obtain a uniform dispersion in which graphene could interact with cellulose matrix in nano-scale level, some special solvents for cellulose, such as ionic liquids and lithium chloride /N, N-dimethylacetamide, were also used for preparation of cellulose/graphene composites. In these cases, the cellulose/graphene composites exhibit good electrical properties and excellent mechanical properties as well as enhanced thermal properties. However, it should be noted that the solvents are either expensive or not commercially available. There is no report to use the cellulose/GO hydrogel as the starting material and a novel platform for the preparation of various functionalized cellulose/GO composites by chemical modification. New routes to fabricate cellulose/graphene composite in a more economic and environmentally friendly process need to be developed. Moreover, it requires a more comprehensive knowledge of the possible interactions between graphene and cellulose to tailor the performance of composites based on them.

3. Experimental part

3.1. Materials and chemicals

Cellulose (Cotton linters, DP 500) was purchased from Hubei Chemical Fiber Group Ltd. (Xiangfan, China). Graphene oxide dispersion (GO, 4 mg/ml, monolayer content > 95%) was purchased from Sigma-Aldrich. L-Ascorbic acid (99 %), iron chloride (FeCl_3 , 97 %), ferrous chloride (FeCl_2 , 99 %), acid orange 7 (AO7, 85 %), urea (ACS \geq 99 %), sodium hydroxide (NaOH, ACS \geq 98 %), sulfuric acid (H_2SO_4 , 95-98 %), hydrogen peroxide (H_2O_2), calcium chloride hexahydrate ($\text{CaCl}_2 \cdot 6\text{H}_2\text{O}$, 98 %), potassium carbonate (K_2CO_3 , 99 %), calcium nitrate tetrahydrate ($\text{Ca}(\text{NO}_3)_2 \cdot 4\text{H}_2\text{O}$, 99 %), sodium nitrite (NaNO_2 , 99 %), sodium chloride (NaCl, 99 %), potassium chloride (KCl, 99 %), acetone, methanol, ethanol, and chloroform were obtained from Sigma-Aldrich. Toluene (99.8 %) and Tetrahydrofuran (THF, 99 %) were supplied by Acros Organics. All chemicals are of reagent grade. Distilled water was used for the experiments.

3.2. Preparation of samples

3.2.1 Preparation of cellulose/rGO composites

Firstly, NaOH/urea/ H_2O solution was chosen as the solvent for the dispersion of GO and dissolution of cellulose. 7 g of NaOH and 12 g of urea were added into 81 g of distilled water and then the mixture was pre-cooled to $-12\text{ }^\circ\text{C}$. 4 g of cellulose was immediately added into the mixture. Under vigorously stirring for 5 min, the mixture turned into the uniform cellulose solution. Subsequently, the designated amount of GO dispersion was introduced into the cellulose solution and mixed under vigorously stirring for 5 min. After degasification, the cellulose/GO solution was poured and casted on a glass plate using a glass tube for a gel sheet. The thickness of the gel sheet was controlled by two iron rings at the ends of the glass tube. The gel sheet with glass plate were soaked into a coagulation bath with 5 wt.% H_2SO_4 at ambient temperature

for 5 min to coagulate and regenerate. The resultant cellulose/GO hydrogel was then washed with deionized water (500 mL) for 3 days (3 times a day). In order to achieve the in-situ reduction of GO into rGO, the cellulose/GO hydrogel was introduced into L-Ascorbic acid (vitamin C) solution (500 mL, 30 g/L). Under vigorously stirring at 95 °C for 2 h, the color of the hydrogel became from brown to black. The resultant hydrogel was then washed again with deionized water (500 mL) for 3 days (3 times a day). Finally, the cellulose/rGO films were achieved by fixing the hydrogels on a glass plate using Scotch® tape and dried for 6 h at temperature. The cellulose/rGO aerogels were obtained by lyophilizing the hydrogels in a freeze drier (Alpha 1-2 LDplus, Christ GmbH, Germany) for 24 h. By using weight ratios of GO to cellulose matrix of 2, 3, 5, and 8 wt.% GO, we fabricated cellulose/rGO composite aerogels with various rGO loadings. In case of rGO/cellulose composites the weight reduction of GO during the reducing process to rGO is ignored in the given compositions. The fabrication of cellulose/rGO film and aerogel is displayed in Fig.3.2.1.

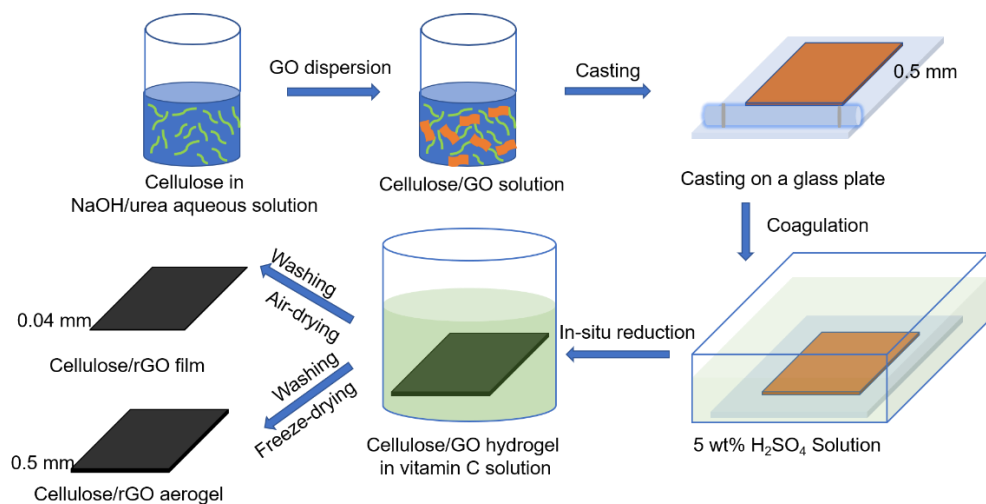


Fig. 3.2.1 Schematic diagram of fabrication of cellulose/rGO film and aerogel.

3.2.2 Preparation of cellulose/GO/Fe₃O₄ composites

An aqueous solution of FeCl₃/FeCl₂ was prepared by mixed 8 mmol FeCl₃ and 4 mmol FeCl₂ in 200 ml of water. Meanwhile, the cellulose/GO hydrogel was followed by the same procedure as described in the 3.2.1. section. Then, the cellulose/GO hydrogel was immediately immersed into the FeCl₃/FeCl₂ solution at room temperature for 2 h. Subsequently, the resultant hydrogel was transferred to 100 ml of NaOH solution (1 M) at room temperature for 5 min. During the immersion in NaOH solution, the color of hydrogel changed from brown to black. The final hydrogel was taken out from the NaOH solution and neutralized by washing with deionized water for 3 days. The preparation of cellulose/GO/Fe₃O₄ hydrogel is described in Fig.3.2.2. For further characterization, the cellulose/GO/Fe₃O₄ hydrogels were fixed on the glass plate by Scotch® tape and dried for 6 h at room temperature to get cellulose/GO/Fe₃O₄ films. We obtained cellulose/GO/Fe₃O₄ hydrogels with various GO loadings at 2, 3, 5, and 8 wt.% by adjusting the amount of GO dispersion.

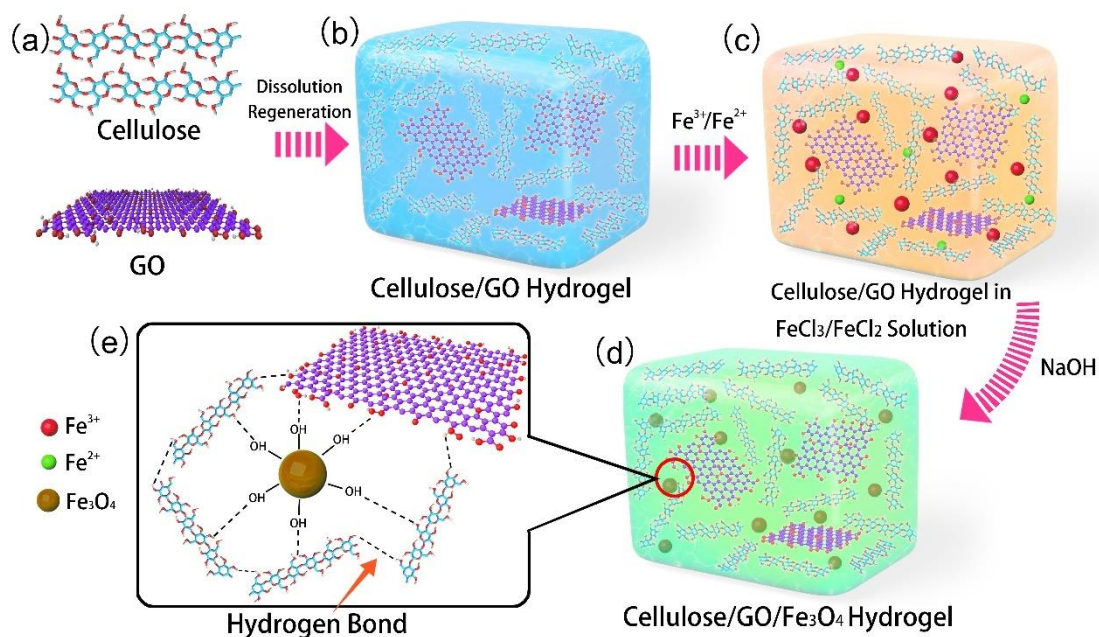


Fig. 3.2.2 Schematic diagram of the synthesis process of cellulose/GO/Fe₃O₄ hydrogel.

3.2.3 Preparation of cellulose/rGO/Fe₃O₄ composites

Firstly, the cellulose/GO hydrogel was prepared by the same procedure as described in Fig. 3.2.1. In order to achieve the in-situ reduction of GO into rGO, the cellulose/GO hydrogel was introduced into L-Ascorbic acid solution (500mL, 30 g/L). Under vigorously stirring at 95 °C for 2 h, the color of the hydrogel changed from brown to black. The resultant hydrogel was then washed again with deionized water for 3 days. Subsequently, an aqueous solution of FeCl₃/FeCl₂ was prepared by dissolution of 8 mmol FeCl₃ and 4 mmol FeCl₂ in 200 ml of water. Then, the cellulose/rGO hydrogel was immediately added into the FeCl₃/FeCl₂ solution at room temperature for 2 h. The resultant hydrogel was transferred to 100 ml of NaOH solution (1 M) at room temperature for 10 min. Then, the cellulose/rGO/Fe₃O₄ hydrogel was taken out from the NaOH solution and washed with deionized water for 3 days. Finally, the cellulose/rGO/Fe₃O₄ films were achieved by fixing the hydrogels on a glass plate using Scotch® tape at room temperature for 6 h. The cellulose/rGO/Fe₃O₄ aerogels were obtained by lyophilizing the hydrogels in a freeze drier (Alpha 1-2 LDplus, Christ GmbH, Germany) for 48 h. We obtained cellulose/rGO/Fe₃O₄ composite films and aerogels with various rGO loadings of 3, 5, and 8 wt.% by adjusting the amount of added GO dispersion. The fabrication scheme of cellulose/rGO/Fe₃O₄ film and aerogel is shown in Fig. 3.2.3.

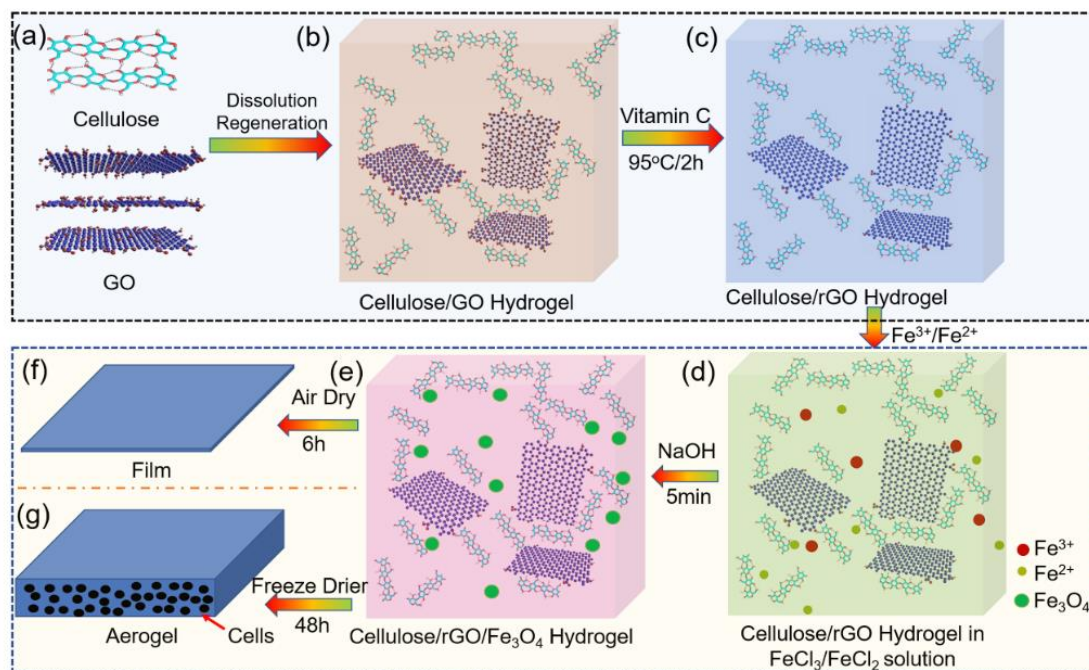


Fig. 3.2.3 Schematic diagram of the synthesis process of cellulose/rGO/Fe₃O₄ film and aerogel.

3.3. Instruments and characterization methods

3.3.1 Characterization of morphology and microstructure, and thermogravimetric analysis

Transmission electron microscopy (TEM) was performed on a LIBRA 200 FE (Carl Zeiss SMT, Oberkochen, Germany) at an accelerating voltage of 100 kV. The sample was prepared for TEM by embedding it into epoxy resin, and obtaining a thin section with the thickness of around 100 nm using a diamond knife. The scanning electron microscopy (SEM) was measured by an Ultra 55 (Carl Zeiss SMT AG, Germany). Before cryo-fracturing, the samples (films and aerogels) were immersed in liquid nitrogen for 5 minutes. The fracture surfaces were then coated with a thin gold layer. In order to investigate the crystal structure of samples, wide angle X-ray diffraction (WAXS) measurements were performed on a D/MAX-1200 (Rigaku Co., Japan) with a Lynx Eye as detector and Cu K α as source with an incident wavelength of 0.154 nm. The diffraction patterns were recorded in the range of 10 to 70° at a scanning

rate of $2\theta = 1^\circ \text{ min}^{-1}$. The power-like cellulose-based samples were measured in quartz glass capillary tubes. X-ray photoelectron spectroscopy (XPS) was carried out with an Axis ULTRA X-ray photoelectron spectrometer (Kratos Analytical, England) and a monochromatic Al K α was used as the source ($h\nu = 1486.6 \text{ eV}$). All XPS spectra were corrected using the adventitious carbon (C1s) line at 284.6 eV. Fourier-transform infrared spectroscopy (FTIR) was measured on a Spectrum 400 FT-IR/ATR Spectrometer (PerkinElmer, USA) with the wavenumber range of 4000-500 cm^{-1} . The Raman-spectra were obtained on a confocal Raman spectroscope alpha 300 R (WITec GmbH, Ulm, Germany) using a 532 nm laser source, a laser power of 1 mW and a $\times 20$ microscope. For better comparability, the Raman-spectra were normalized to the highest peak in the range of 800 to 2000 cm^{-1} .

Thermogravimetric analysis (TGA) was performed on a TGA Q5000 (TA Instruments, USA). The measurements were done from 30 to 800 $^\circ\text{C}$ under the protection of nitrogen with a heating rate of 10 $^\circ\text{C min}^{-1}$. UV-visible spectrophotometry using a Evolution 220 (Thermo Fisher Scientific) was carried out to investigate the in-situ reduction of GO to rGO at the transmittance wavelength of 800 nm.

3.3.2 Characterization of sensing abilities

The sensing performance of the cellulose/rGO composites responding to different external stimuli (temperatures, RH, tensile strains, liquids, and vapors) was tested by measuring the resistance change caused by the different stimuli using a Keithley 2001 multimeter, which monitored the DC electrical resistance. The cellulose/rGO composite films and aerogels for electrical resistance measurement were cut from the resultant composites by different dry methods (films: $10 \times 3 \times 0.05 \text{ mm}^3$, aerogels: $10 \times 3 \times 0.5 \text{ mm}^3$). The electrical resistance values of sample were collected every 1 s. Here, the relative electrical resistance change, R_{rel} , is defined by

Eq. 3.3.1 to compare the performance of sensors independently of the initial resistance,

$$R_{rel}(\%) = \frac{R_t - R_0}{R_0} \times 100 \quad (3.3.1)$$

where R_t stands for the transient resistance at time t and R_0 the initial resistance of the sample.

The temperature sensing performance was tested in a hot-stage (Linkam LTS350 Heating/Freezing, UK). The measurements were done from 280 to 380 K and then from 380 to 280 K with a scan rate of 1 K /min in nitrogen atmosphere. The temperature coefficient of resistance (TCR) is usually used to qualify a thermistor. Here, TCR is defined as

$$TCR = (1/R_0) \times (dR/dT) \quad (3.3.2)$$

where R_0 represents the sample resistance at initial temperature (280 K) and R the sample resistance at temperature T .

The relative humidity (RH) sensing performance was tested by exposing the sample to different RH values atmospheres, created through saturated solutions of different salts: KCl (86 %), NaCl (76 %), NaNO₂ (65 %), Ca(NO₃)₂·4H₂O (55 %), K₂CO₃ (45 %), and CaCl₂·6H₂O (35 %). Moreover, the samples were placed at a distance of ca. 100 mm from human nose to test the change of the resistance to human breathing cycles.

The strain sensing performance was performed on a Zwick 2.5 (Zwick Roell, Germany) tensile machine. The film sample underwent uniaxial tensile straining with the speed of 1 mm/min and with an initial gauge length of 30 mm, and a strain amplitude of 2 %. In order to detect the human motions, the film sample was fixed on the back of the forefinger and the human hand. Moreover, the film sample was also

used as strain sensor during the bending/relaxation process with a bending angle of about 90°.

The size of cellulose/rGO film for liquid sensor measurements is shown in Fig. 3.2.2.1. During immersion/drying cycles, the resistance values of samples were recorded every 1 s. Moreover, the samples were also placed in a heating/cooling bath to change and control the liquid temperature during immersion. During the drying process, the sample was placed at atmosphere of 50 % relative humidity at 23 °C. The different liquids chosen in this part were acetone, ethanol, water, and sodium chloride solution (0.5 wt.%, 1 wt.%, and 2 wt.%).

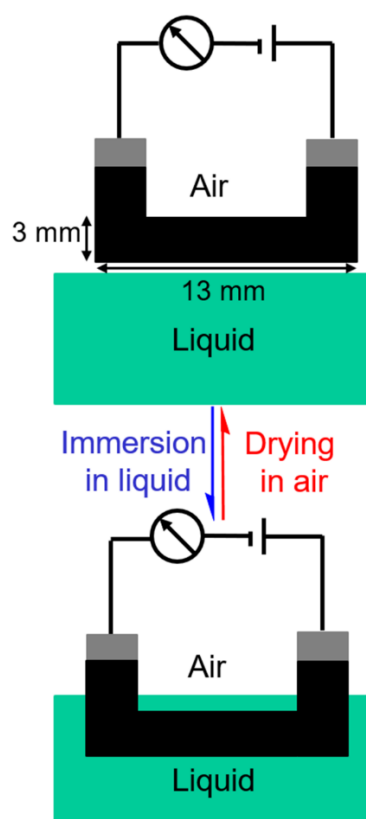


Fig. 3.2.2.1 Schematic of liquid sensing test.

Vapour sensing tests of aerogels were performed by recording the changes in the electrical resistance when the aerogel was exposed to cyclic flows of dry air and vapour. Samples used as vapour sensors ($13 \times 3 \times 0.5 \text{ mm}^3$) were cut from cellulose/rGO composite aerogels (Fig. 3.2.2.2), and coated using highly conductive silver paste

(Acheson Electrodeag 1415) over the sample edges to get sufficient contacts between electrodes and aerogels. The measurements were performed in a homemade experimental setup as presented in Fig. 3.2.2.2. A certain concentration of vapours was delivered to the chamber where the aerogel was placed to analysis. Here, dry air functions as the carrier for the vapours. The concentrations of diluted vapours, controlled by changing the flow rates using the flow contrallers MFC1 and MFC2, were then calculated by the following equation Eq. 3.3.3,

$$C(\%) = \frac{P_i}{P} \times \frac{f}{(f+F)} \times 100 \quad (3.3.3)$$

where P is the input air pressure and P_i is the saturated partial pressure of different solvents at 25 °C, f and F are the mass flow rates of MFC 1 and MFC 2, respectively. The overall flow rate was typically set to 30 L/min. Aerogels with different filler loadings (3 wt.%, 5 wt.%, and 8 wt.%), different vapours types (acetone, water, ethanol, toluene, methanol, chloroform, and tetrahydrofuran), and different vapour contents (25 %, 50 %, 75 %, 100 % of the saturated pressure) at 25 °C were tested. Each vapour/dry air cycle is performed by an exposure to vapours for 400 s and an exposure to dry air for 200 s.

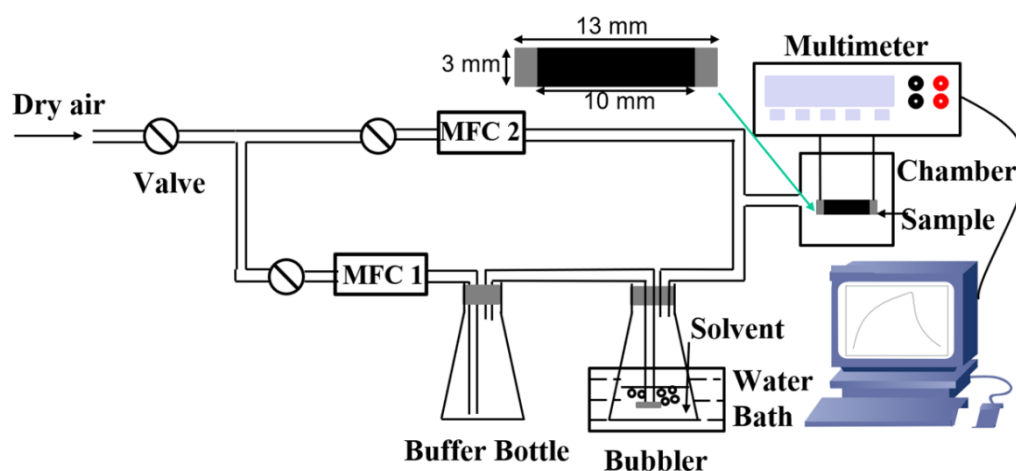


Fig. 3.3.2.2 Schematic of the homemade vapour sensor measurement system.

3.3.3 Characterization of catalytic activity

For the investigation of the effect of initial parameters (temperature T , H_2O_2 concentration $[H_2O_2]$, pH, and AO7 dye concentration $[AO7]$) on the catalytic activity, the cellulose/GO (8 wt.%)/ Fe_3O_4 hydrogel was selected as standard sample to test. For example, 5 g hydrogel ($120 \times 80 \times 0.5 \text{ mm}^3$) were immersed into 250 mL of AO7 solution and the catalytic performance was tested by monitoring of the AO7 degradation with reaction time. The concentration of AO7 was determined by testing the absorbance of the AO7 solution at a wavelength of 484 nm. The UV-vis spectra of the samples were obtained at room temperature in the range of 200 - 600 nm with a UV-vis spectrophotometer (Evolution 220, Thermo Fisher Scientific). It is worth noting that the optimisation of the experiment was carried out by changing one parameter and keeping the others constant. The range of parameters was determined as follows: $[H_2O_2] = 33, 22, 11, 5.5 \text{ mM}$; $[AO7] = 0.4, 0.3, 0.2, 0.1 \text{ mM}$; $T = 338, 318, 298 \text{ K}$; $pH = 4, 3.5, 3, 2.5, 2$.

Subsequently, in order to study the catalytic performance of different hydrogels (cellulose/ Fe_3O_4 , cellulose/GO, and cellulose/GO/ Fe_3O_4), the catalytic performance for AO7 degradation was tested at the same conditions (experimental conditions: $[\text{catalyst}] = 0.2 \text{ g L}^{-1}$, $T = 298 \text{ K}$, $[H_2O_2] = 22 \text{ mM}$, $pH = 3$, and $[AO7] = 0.1 \text{ mM}$). The initial pH of the AO7 solution was adjusted to 3 by using 1 M NaOH or 1 M HCl. After the adjustment of pH, 5 g hydrogel ($120 \times 80 \times 0.5 \text{ mm}^3$) was added into 250 mL of AO7 solution. It is worth noting that the mixture should be stirred in the dark for 30 min at 300 rpm to reach the adsorption equilibrium before the reaction. Then, H_2O_2 (22 mM) was added into the suspension. AO7 was degraded during the reaction and its concentration was analysed immediately after taking off the hydrogel sample from the AO7 solution. For the 20 consecutive cycles, the hydrogel sample was taken from the solution and washed thoroughly with deionized water, and then it was added into fresh AO7 solution.

3.3.4 Characterization of electrical, dielectric, magnetic, and EMI shielding abilities

The electrical conductivity of samples was tested by a Keithley 2001 multimeter. Samples were cut down from cellulose/rGO/Fe₃O₄ composite films (size 10 x 3 x 0.04 mm³) and aerogels (size 10 x 3 x 0.5 mm³). The sample edges were coated using highly conductive silver paste (Acheson Electrodag 1415) to get sufficient contacts between electrodes and samples. The values of electrical conductivity for each sample were tested at least five times and averaged. Dielectric measurements of the cellulose/rGO/Fe₃O₄ composite aerogels (size 10 x 3 x 0.5 mm³) and films (size 10 x 3 x 0.04 mm³) were done by a HP 8510C vector network analyzer (Keysight technologies, USA) in the frequency range of 8.2-12.4 GHz. Magnetic properties of cellulose/rGO/Fe₃O₄ composite aerogels (size 5 x 5 x 0.5 mm³) and films (size 5 x 5 x 0.04 mm³) were measured on a Lake Shore 7410 vibrating sample magnetometer (VSM, USA) at $T = 5$ and 300 K. In this measurement, the VSM system rapidly vibrates a sample between two pickup coils while applying a magnetic field. The created alternating magnetic field induces an electric bias, which defines the magnetic moment of the sample. The full hysteresis loop was obtained from -20 kOe to 20 kOe. The EMI shielding effectiveness of cellulose composite films and aerogels were performed on a Keycom waveguide WR-62 with Agilent vector network analyser (Anritsu MS4642A, USA) at ambient temperature in the range of 8.2-12.4 GHz (X band). The aerogel and film samples with diameters of 10 mm and different thicknesses were placed between two X-band waveguide parts that were connected to separate ports of the vector network analyser. Up to four samples were stacked on top to each other to vary the thicknesses between 0.5 and 2 mm (aerogels) or 0.04 to 0.16 mm (films).

4. Result and discussion

4.1. Cellulose/rGO composites for multiple sensing applications

Note: The results presented in chapter 4.1 are published in my paper “Smart cellulose/graphene composites fabricated by in-situ chemical reduction of graphene oxide for multiple sensing applications” (J. Mater. Chem. A, 2018, 6, 7777-7785) with the co-authors Petra Pötschke, Jürgen Pionteck, Brigitte Voit, and Haisong Qi.

4.1.1 Introduction

The continuous consumption of non-renewable resource and the “white pollution” caused by the non-degradability of plastic polymers motivate demands from renewable resources. Cellulose, the most abundant and inexhaustible biopolymer in nature, has recently gained enormous attention due to its good chemical stability, non-toxicity, biodegradability, low-cost, biocompatibility, availability, renewability, and hydrophilicity. It is of profound importance to develop functional and smart materials based on cellulose, because of cellulose as the robust and stable matrix or carrier has the ability to form stable and strong stiff-chain homomolecular structures [12, 13]. Specially, numerous functional and smart nanofillerintegrated cellulose materials can be easily fabricated by the process of mixing or coating inorganic materials in the form of nanotubes, nanowires, and nanocrystals. These functional and smart materials can be used in many applications such as sensors, electronic devices, for electromagnetic interference shielding and as supercapacitors [3, 100, 101].

Over the past decades, sensors based on nanofillers have attracted numerous interests due to their strain sensing performance. Strain sensors have plenty of applications in detecting deformation and human motion. It is necessary to fabricate a strain sensor material that exhibit excellent sensitivity in response to a small strain. For example, in monitoring human health, the signals to be detected are usually very small,

such as breath, pulse, and so on. Volatile organic compounds (VOCs) are organic chemicals with high vapour pressure at room temperature. Some VOCs are dangerous to human health or cause harm to the environment. Therefore, reliable, portable, and low-cost vapour sensors or liquid sensors play increasingly important role in plenty of applications in industrial production and safety, air quality monitoring, medical diagnostics, aircraft, space exploration, and so on [102-105]. Nowadays, vapour sensors or liquid sensors are of intense significance in promoting the combination properties of vapour and liquid sensing materials, such as ultrahigh sensitivity, fast response and recovery, high specificity, and good reversibility [106, 107]. So far, plenty of vapour or liquid sensor materials have been reported, for example semiconductors metal oxide (SMO), e.g., SnO₂ [108], ZnO [109], and α -Fe₂O₃ [110], nano-carbons, e.g., carbon nanotubes [111] and graphene [112], organic semiconductors [113], intrinsically conducting polymers (ICPs), e.g., poly(3,4-ethylenedioxythiophene) (PEDOT) [114], and conductive polymer (CPCs) [115]. The most important characteristic that determines the sensitivity of nanometric materials is the high surface-to-volume ratio. This is beneficial for the adsorption of vapours on sensing materials and can enhance the sensing properties of this vapour sensing material.

Graphene, a single nanosheet with sp²-hybridized carbon atoms, has received more and more attention in recent years because of its outstanding mechanical properties [116], chemical stability [117], superior electrical conductivity [118], and strong vapour/gas adsorption capacity [119]. Thus, the high-performance material shows great potential for many fields, e.g. in supercapacitors [120], lithium ion batteries [121], solar cells [122], and vapour/gas sensors [123]. The unique structure of this material renders it the electron transfer through graphene highly sensitive to the adsorption of vapour/gas molecules [124]. All of these features for graphene are beneficial for its sensing properties, rendering an ideal activity for humidity, liquid, and vapour testing and detection. The adsorption of vapour/gas molecules on the surface of graphene leads to changes in its electrical conductivity. However, the practical

application of graphene is severely restricted by their poor dispersion and secondary aggregation in the dispersion and mixing process, bringing about the hardship to preserve their superiority. There have been a lot of efforts to deal with the problem, including micromechanical exfoliation of graphite, chemical vapour deposition, reduction of GO, etc. [38, 39, 125, 126]. Among them, preparation of graphene from GO reduction is the most promising method for the cost-effective, large-scale production of graphene-based materials. Many oxygen-containing functional groups of GO sheets make them uniformly dispersible in water. Meanwhile, they offer favorable conditions for the in-situ reduction of GO. Considering the strong aggregations of graphene sheets, furthermore, GO is also used as the starting material in place of graphene. In general, the vapour sensing properties can be greatly improved by the increase of internal surface area between vapour molecules and the vapour sensor [127]. Aerogel is a synthetic porous ultralight material, which has a porous solid network that contains air pockets [128, 129]. Due to its specific performances, such as large open pores, high internal surface area, and low density, aerogel is very suitable for vapour adsorption and storage.

In this chapter, cellulose/rGO composite hydrogel was successfully fabricated by dissolving cellulose and dispersing GO in sodium hydroxide/urea/water solution, followed by the chemical reduction of GO with vitamin C as the reducing agent. The cellulose/rGO films and aerogels with various rGO contents were prepared by air-drying and freeze-drying of the prepared cellulose/rGO composite hydrogels. The cellulose/rGO composite films applied as multifunctional sensors responded to different external stimuli, such as temperature, humidity, stress/strain, and liquids. The vapour sensing properties of the resultant aerogels are tested by exposing them to five vapour/dry air cyclic runs. The influences of overall rGO contents, vapour types, and vapour concentrations on the sensing capacity was determined.

4.1.2 In-situ chemical reduction of GO

Cotton linters from cotton as shown in Fig. 4.1.1 (a) are taken as cellulose raw material for the regeneration of cellulose composites. The homogenous cellulose/GO hydrogels as starting material can be used for a large number of functional and smart materials. In this work, the in-situ chemical reduction of GO is performed to obtain the electrically conducting cellulose/rGO composites in an environmentally friendly, low-cost, and efficient way. It is well known that cellulose-based hydrogels prepared from similar sodium hydroxide/urea/water solutions contain more than 90 % of water and can form aerogels with the highly porous network structure [111, 130]. The cellulose-based hydrogel as schematically illustrated in Fig. 4.1.1 (b) provides ideal conditions for the easy diffusion of reduction agents and efficient reaction of reduction agents with GO. At the same time, the cellulose-based hydrogel can preserve its structure during the in-situ chemical reduction of GO and further can form by freeze-drying cellulose-based aerogel with the highly porous network structure as shown in Fig. 4.1.1 (c). During the in-situ chemical reduction, L-ascorbic acid (vitamin C) as a non-toxic and environmentally friendly reducing agent shows excellent reduction characteristics. For example, as shown in Fig. 4.1.1 (d) and (e), the color of cellulose/GO hydrogels changed rapidly from brown to black after only 3 minutes. Fig. 4.1.2 shows the UV-vis transmittance of cellulose/GO and cellulose/rGO film (thickness 0.5 mm) which illustrate the rapidity of in-situ chemical reduction. The UV-vis transmittance significantly dropped from 7.0 % to 0.3 % at the wavelength of 800 nm after several minutes and reached nearly zero after 60 min. The resultant cellulose/GO and cellulose/rGO films air-dried from the hydrogels as shown in Fig. 4.1.1 (d) and (e) are flexible and isotropic. These characteristics of the films are beneficial for the application of composite films as functional and smart material. The typical TEM image of cellulose/rGO (5 wt.%) composite film is shown in Fig. 4.1.1 (f). Obviously, the well-exfoliated rGO is efficiently dispersed in the cellulose matrix by

the environmentally friendly and efficient preparation. The thickness of individual rGO nanosheets is about 1.2 nm.

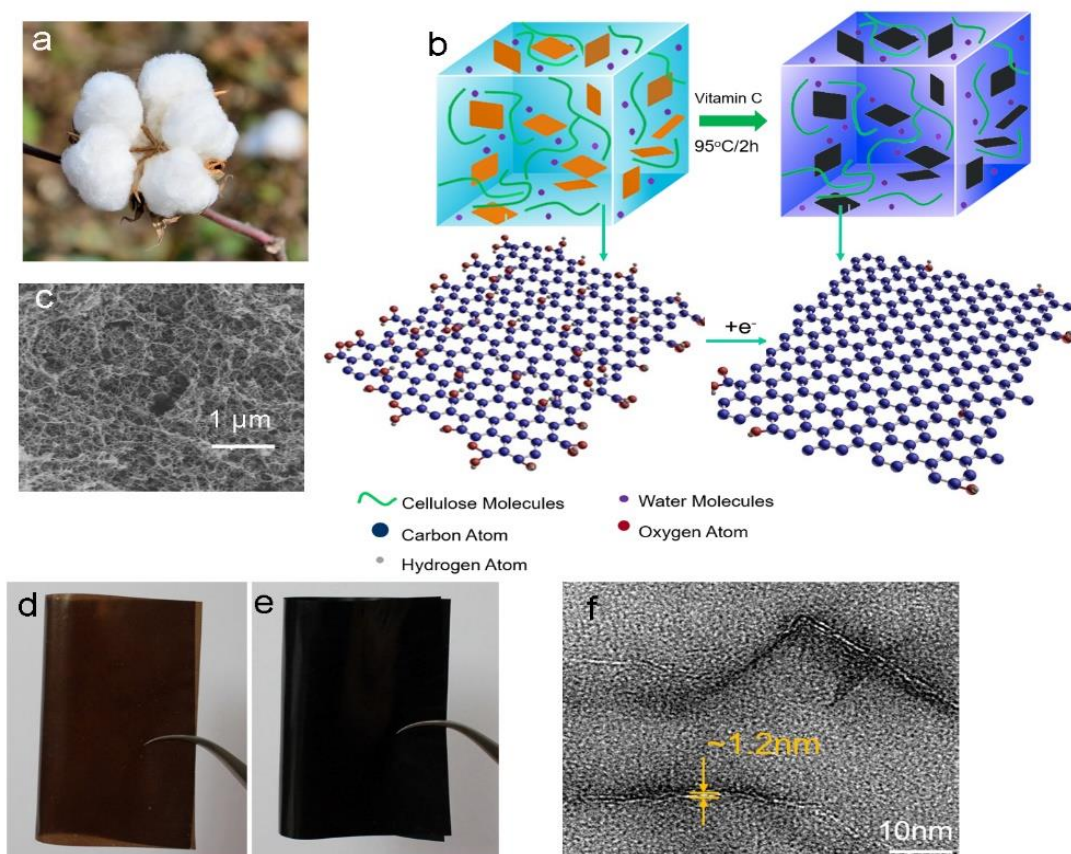


Fig. 4.1.1 Fabrication of cellulose/GO and cellulose/rGO composites. (a) The photograph of cotton linters. (b) Schematic of in-situ reduction of GO in cellulose-based hydrogels. (c) SEM image of cellulose/rGO composite hydrogel. (d) Photograph of the resultant cellulose/GO and (e) cellulose/rGO composite films (8 cm × 14 cm). (f) TEM image of cellulose/rGO composite film.

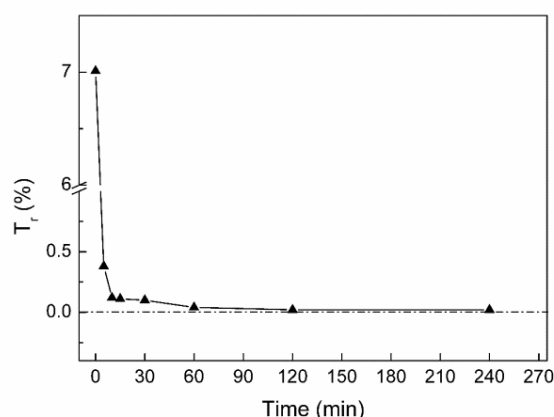


Fig. 4.1.2. Dependence of the optical transmittance (T_r , %, 800 nm) of the cellulose/rGO (5 wt.%) composite films on the time of reduction.

4.1.3 Properties of cellulose/GO and cellulose/rGO composites

In the XRD spectra (Fig. 4.1.3 (a)) is only diffraction pattern of cellulose visible in both cellulose/GO and cellulose/rGO composites, which can be due to the uniform dispersion of GO or rGO and strong hydrogen interactions between cellulose matrix and fillers. The properties and structures and cellulose/GO and cellulose/rGO composites are also characterized by the FTIR analysis in Fig. 4.1.3 (b). The FTIR spectrum of pure cellulose and GO shows peaks at 3360 cm^{-1} and 3365 cm^{-1} , corresponding to the hydroxyl groups. In FTIR spectrum of cellulose/rGO and cellulose/GO composites, the position moves to 3335 cm^{-1} and 3330 cm^{-1} , respectively. Therefore, the strong hydrogen bond interactions between cellulose matrix and fillers in cellulose/rGO and cellulose/GO composites, which led to the good compatibility of fillers and matrix, were demonstrated by XRD and FTIR spectroscopy.

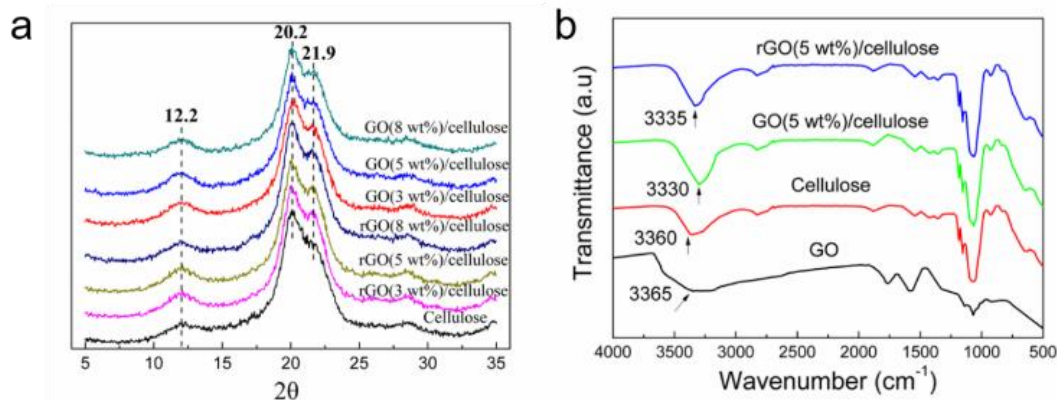


Fig. 4.1.3 (a) XRD pattern of cellulose, cellulose/GO, and cellulose/rGO composites. (b) FTIR spectra of GO, cellulose, cellulose/GO, and cellulose/rGO composites.

Raman characterization is a convenient and powerful technique of testing the reduction of GO. Raman spectra of graphene often consist of two main peaks: G peak (ca. 1604 cm^{-1}) arising from the in-plane vibration of sp^2 carbon atoms in the graphene sheets and D peak (ca. 1350 cm^{-1}) assigned to the sp^3 defects due to oxidation. Raman spectra of cellulose, cellulose/GO, and cellulose/rGO composites are shown in Fig. 4.1.4. The D/G intensity ratio of rGO is around 1.54, while the result of GO is around 1.01. This result contradicts the general expectation. During in-situ reduction, the D/G intensity ratio should decrease as the number of sp^3 defects decreases due to the reduction. However, the opposite effect has often been found in the literature [131, 132], and is explainable by the creation of small sp^2 domains with large fraction of graphene edges at lower GO reduction degrees. At higher reduction degrees, the small domains merge to larger ones with less edges and thus the D/G intensity will decrease, as expected.

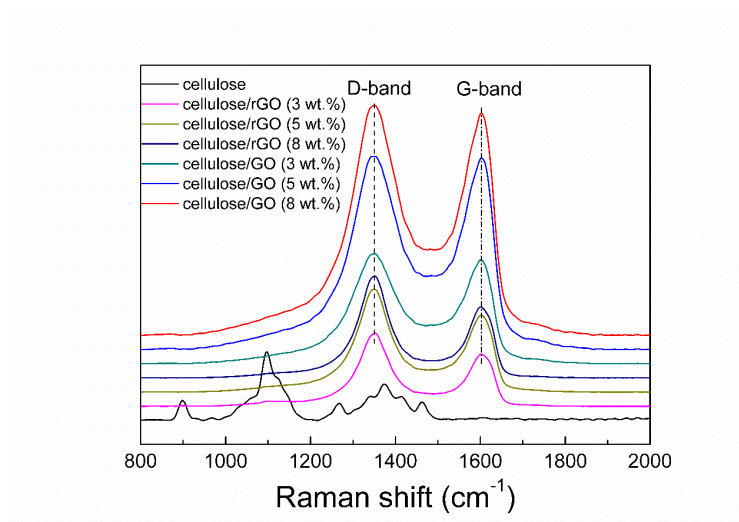


Fig 4.1.4 Raman spectra of cellulose, cellulose/GO and cellulose/rGO composites.

The electrical conductivity of cellulose/rGO composite films can be adjusted by changing the content of filler. As shown in Fig. 4.1.5, the electrical conductivity of cellulose/rGO composite films enhances significantly with the increased filler loading. For example, the electrical conductivity of cellulose/rGO (5 wt.%) film is $8.1 \times 10^{-5} \text{ S cm}^{-1}$ and cellulose/rGO (8 wt.%) film is $6.3 \times 10^{-4} \text{ S cm}^{-1}$, respectively. The electrical conductivity of cellulose/rGO (5 wt.%) aerogel is $5.7 \times 10^{-6} \text{ S cm}^{-1}$ and cellulose/rGO (8 wt.%) aerogel is $1.9 \times 10^{-5} \text{ S cm}^{-1}$, respectively. The electrical conductivity of different composite films and aerogels also confirm the successful chemical reduction and ensure the potential application in sensing filed. In this work, cellulose/rGO (5 wt.%) films and cellulose/rGO (8 wt.%) aerogels were chosen for sensor tests, which is ascribed to its suitable electrical conductivity (the electrical conductivity is not too high and just above the percolation value).

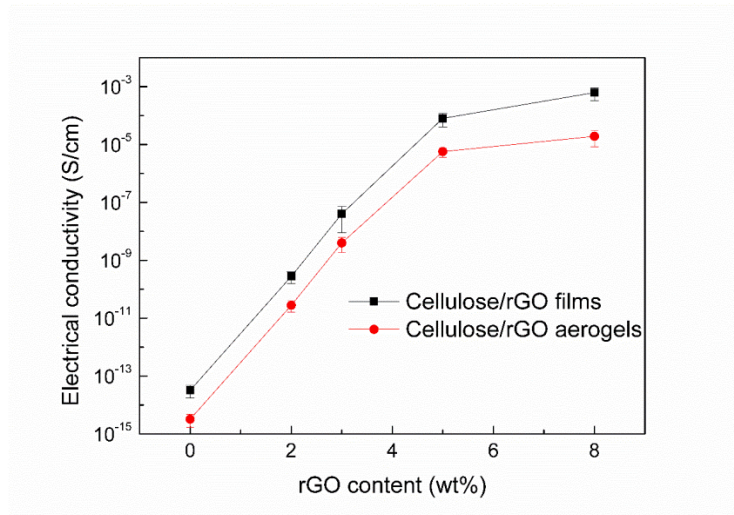


Fig. 4.1.5 Electrical conductivity of cellulose/rGO films and aerogels in dependence on filler content.

4.1.4 Temperature and humidity sensor of cellulose/rGO composites

Fig. 4.1.6 (a) shows the R_{rel} of cellulose/rGO (5 wt.%) composite film under two temperature sweeps (warming up and cooling down cycles). R_{rel} of cellulose/rGO (5 wt.%) composite film decreases monotonically with increasing of temperature, indicating that our cellulose/rGO composite film has the potential as a temperature sensor. The negative temperature coefficient (NTC) is ascribed to semiconductor characteristics of our temperature sensor. With increasing temperature, electron transferred from valence states to conduction states in rGO sheets by thermal activation [133]. The value of temperature coefficient of resistance (TCR) is about $-4.9 \times 10^{-4} \text{ K}^{-1}$. The result is corresponding with other composites reported by other authors, such as the value of multiwall carbon nanotube (MWCNT) based temperature sensors which is about $-7.0 \times 10^{-4} \text{ K}^{-1}$ or $-1.8 \times 10^{-4} \text{ K}^{-1}$ [134, 135]. The good reproducibility of the temperature sensing of this cellulose/rGO composite film is also shown in Fig. 4.1.6 (a), where the sensing signal of the film is plotted for two temperature sweeps. This result

indicates that the filler contacts are not damaged during the temperature sweeps, thus one can apply this cellulose/rGO composite film in the temperature sensing fields.

The resistance changes of cellulose/rGO composite films as function of humidity are shown in Fig. 4.1.6 (b). R_{rel} of cellulose/rGO (5 wt.%) composites monotonically increase with increasing of relative humidity (RH). The relationship between R_{rel} of cellulose/rGO (5 wt.%) composites and relative humidity can be defined as: $R_{rel} \propto \exp(b \cdot RH)$; here b represents a positive constant. In this work, b equals 2.6. This result is corresponding with that of glass fibers/MWCNTs ($b = 4.0$) [136]. In general, the electrical conductivity of this vapour sensor is due to the electron transfer between rGO sheets. The increase of R_{rel} can be ascribed to two mechanisms: adsorption of liquid molecules on the surface of rGO sheets and swelling of the cellulose matrix. On one hand, we marked the change of electrical resistance from swelling as ΔR_S . The adsorption of water immediately leads to the swelling of matrix, which destroys the connection between rGO sheets, which brings about the decrease of the electrical conductivity of the composite film. On the other hand, water molecules on rGO sheets change the carrier concentrations of rGO, resulting in enhanced of electrical resistance. We called the change of electrical resistance from absorption as ΔR_A . As shown in Fig. 4.1.6 (b), R_{rel} of cellulose/rGO (5 wt.%) composite films can increase to about 40 %, which is similar to that of glass fibers/MWCNTs composites [136].

Furthermore, it would be interesting to explore whether the cellulose/rGO composite is suitable for humidity sensing. The relative humidity RH of the air in the lab was about 35 %, while RH of human exhaled breath is about 80 % [137]. As illustrated in Fig. 4.1.6 (c), the cellulose/rGO composite film was placed at a distance of about 100 mm from human nose over several breathing continuous cycles. The response of R_{rel} of cellulose/rGO composite film over 11 breathing continuous cycles is recorded in Fig. 4.1.6 (d). R_{rel} increases and recovered rapidly corresponding to human breath exhalation and inhalation cycles, due to the reversible adsorption-desorption

process of water molecules on the rGO sheets and the reversible hygroscopic swelling of the cellulose matrix. Notedly, the maximum of R_{rel} is about 10 % during the breathing continuous cycles, which is corresponding with that of glass fiber/GNP composites (14 %) [137].

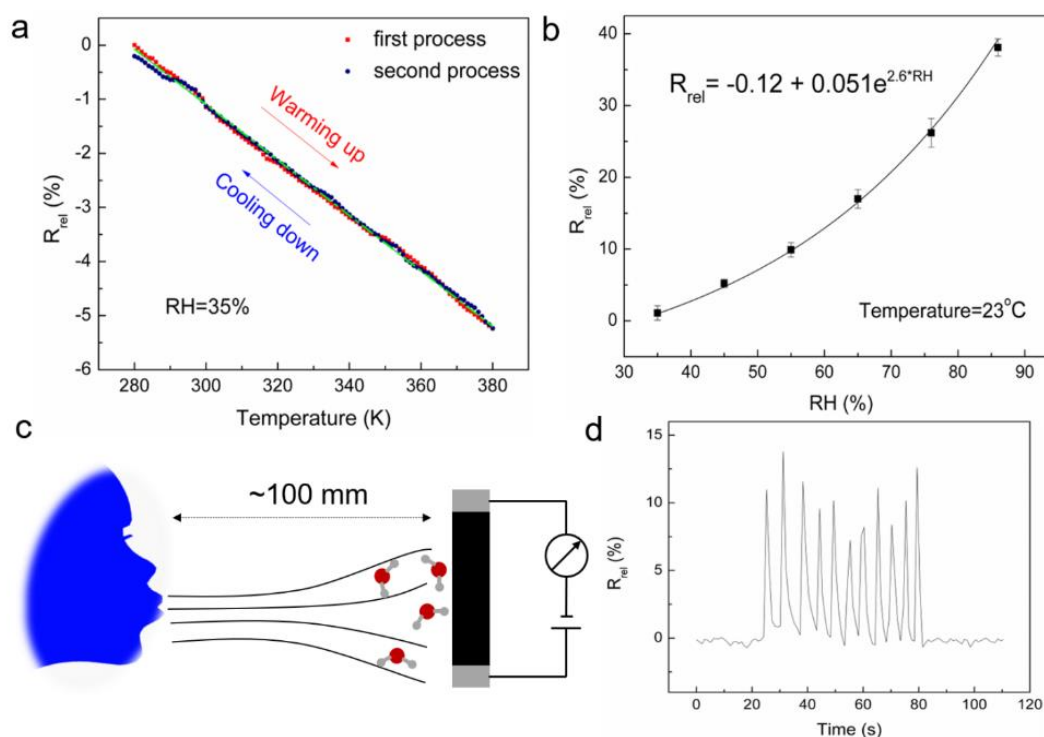


Fig. 4.1.6 Sensitivity of cellulose/rGO (5 wt.%) composite film to temperature and humidity: (a) The temperature dependence of the R_{rel} in the temperature range of 280-380 K. (b) The humidity dependence of R_{rel} . (c) Schematic for in-situ monitoring electrical resistance changes of cellulose/rGO (5 wt.%) composite film placed at a distance up to 100 mm from one's nose. (d) Dependence of R_{rel} on time for in-situ monitoring human breathing cycles of inhalation and exhalation.

4.1.5 Strain sensor of cellulose/rGO composites

To explore whether cellulose/rGO composite is sufficient for strain sensing, the R_{rel} of cellulose/rGO (5 wt.%) composite film was recorded with the strain rate at 1 mm/min (Fig. 4.1.7 (a)). With the increasing of strain, R_{rel} of the composite increases monotonously. Furthermore, a nearly linear relationship between R_{rel} and strain remains

nearly until the final fracture. To proof the reproducibility of cellulose/rGO composite film for strain sensing, Fig. 4.1.7 (b) illustrates the R_{rel} of cellulose/rGO (5 wt.%) composite film over 10 consecutive stretching/releasing cycles. The result demonstrated the good repeatable strain sensing performance of cellulose/rGO (5 wt.%) composite, despite a certain level of irreversible changes. Notedly, the nonflexible and soft contacts between rGO resulted in a consolidation process during the first cycle.

Cellulose/rGO (5 wt.%) composite film has the potential application in detecting human hand motions, such as stretching/releasing and bending/relaxation, since the film has excellent strain sensing properties such as high resistance response, bendability, and flexibility. In human hand motions, the high stress values result from the high strain rates [138]. As shown in Fig. 4.1.7 (c), R_{rel} increases and recovered rapidly corresponding to closing and opening a fist, whereby cellulose/rGO (5 wt.%) composite film was attached on back of hand. R_{rel} was also increased and decreased when the sample is under bending/relaxation continuous cycles (Fig. 4.1.7 (d)). Moreover, cellulose/rGO (5 wt.%) composite film also indicates fast responses to human finger bending and stretching. These curves show reproducible response of R_{rel} over several cycles. The reproducible responses of R_{rel} can be attributed to the reproducible change of rGO distances, thereby resulting in the change of electrical resistance. The maximum value of R_{rel} for our cellulose/rGO (5 wt.%) composite film is about 1 %, 2 %, and 8 % in three different human motions. Similar results are reported by other researchers. For example, the maximum value of R_{rel} of a PDMS/SWCNT film is between 3 % and 11 % [139]. The cellulose/rGO composite films with high strain sensing response and flexible properties expand its application in strain sensing fields to distinguish out different human motion by analyzing the resistance response.

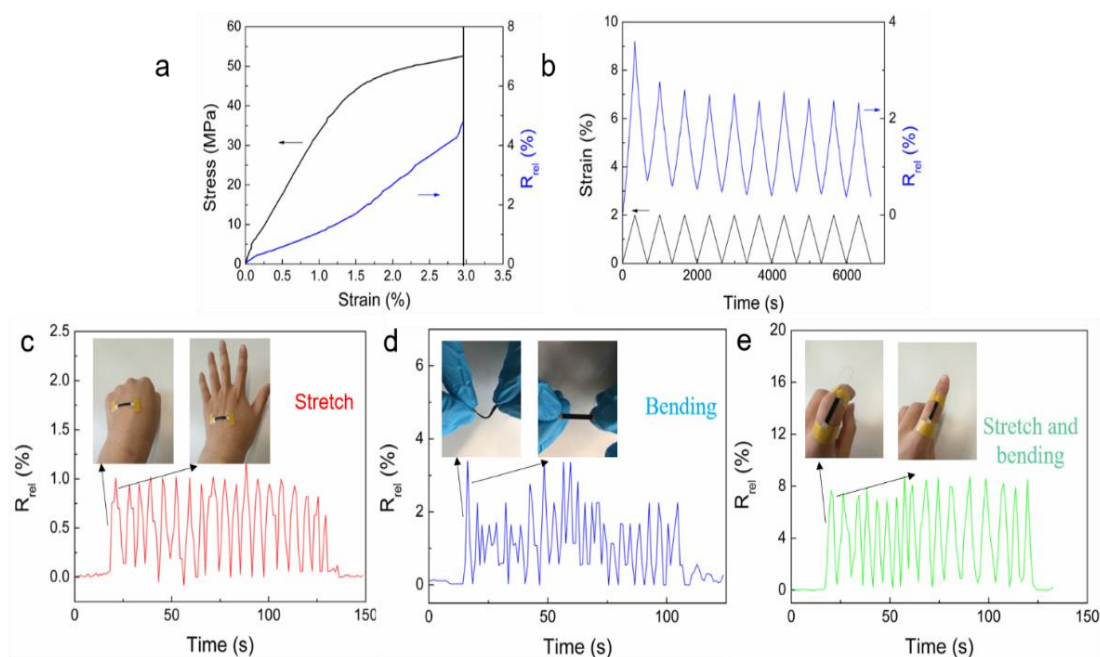


Fig. 4.1.7 The electrical responses to external strain for cellulose/rGO (5 wt.%) composite film. (a) Stress development (black) and resulting R_{rel} changes (blue). (b) R_{rel} (blue) and tensile strain (black) versus time during cyclic stretching to a fixed strain of 2 %. (c) R_{rel} in dependence of cyclic hand motions from stretch to clench. (d) R_{rel} as result of a cyclic bending/relaxation processes. (e) R_{rel} as result of finger motions from stretch to clench.

4.1.6 Liquid sensor of cellulose/rGO composites

Fig. 4.1.8 showed the R_{rel} of cellulose/rGO (5 wt.%) composite films when the sample was immersed in water and dried in air, in order to test whether cellulose/rGO composites can be applied in liquid sensing. As shown in Fig. 4.1.8, when the sample was immersed in water, R_{rel} of the sample significantly and fast increased during the first 20 s, and then it slowly reached a plateau value of ca. 460 % (150 s). Then, when the sample was dried in air, R_{rel} of the sample slowly reached the initial state (350 s). Interestingly, there is a small increase when the sample was just taken from water, which is due to water flow effects on the surface and the fast water removal. The adsorption-desorption of water on graphene surface and hygroscopic swelling-shrinking process of the cellulose matrix are completely reversible and result

in the good recovery. Further, R_{rel} of the cellulose/rGO (5 wt.%) composite film under 10 continuous water exposure-drying cycles is shown in Fig. 4.1.9 (a). Apparently, the maximum of R_{rel} reached almost the same value and the responses of R_{rel} are reproducible during 10 successive cycles. The cellulose/rGO composite films in this work show excellent water sensitivity: quick response and high sensitivity. For example, the maximum value of R_{rel} can reach as high as 460 %. This sensitivity is remarkably higher than other liquid sensing polymer-based materials. For example, PCL/MWCNT (0.5 wt%) composites exhibited the maximum value of R_{rel} at about 3.5 % [140]. PLA /MWCNT (2 wt.%) composites gave a maximum value of R_{rel} of about 6 % [141]. This high sensitivity and fast response indicate that our sensing material is very suitable as a water sensor.

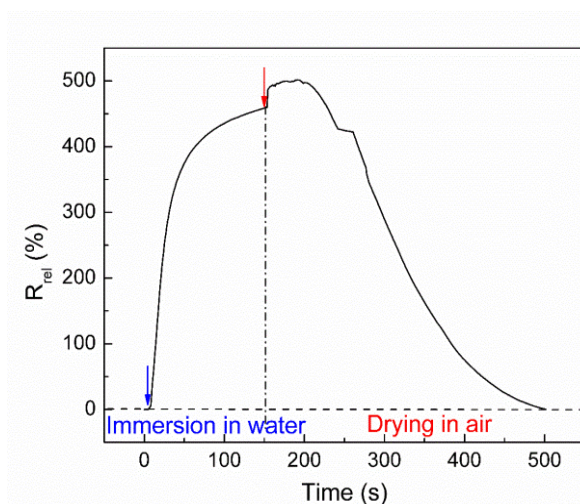


Fig. 4.1.8 Relative resistance change (R_{rel}) of cellulose/ rGO (5 wt.%) composite film during immersion/drying (150 s/350 s) cycle in water at 20 °C.

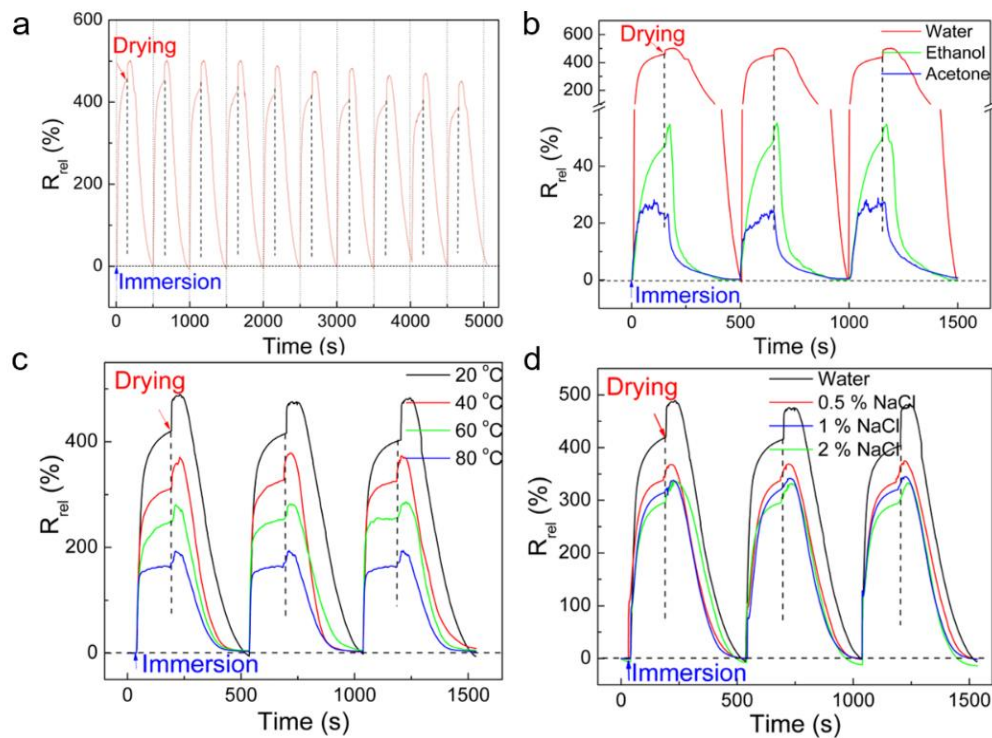


Fig. 4.1.9 Sensitivity of cellulose/rGO (5 wt.%) composite film to liquids. (a) R_{rel} changes with time during 10 immersion/drying (150 s/350 s) cycles in water (20 °C). (b) R_{rel} changes with time during 3 immersion/drying (150 s/350 s) cycles in different solvents (20 °C). (c) R_{rel} changes with time during 3 immersion/drying (150 s/350 s) cycles in water at different temperatures. (d) R_{rel} changes with time during 3 immersion/drying (150 s/350 s) cycles in aqueous NaCl solutions (20 °C) at different salt concentration.

Fig. 4.1.10 schematically illustrated the water sensing mechanisms of cellulose/rGO composites. Before cellulose/rGO composite film is immersed into water, the SEM image of the sample shows the network-like structure. The samples for SEM test were prepared by flash freezing in liquid nitrogen after being immersed in water for 150 s. This method can preserve the swollen state of cellulose/rGO composite film as it was in water and shows a much more open structure than that before immersion in water. The mechanism of the liquid sensing performance is in consistency with that of RH sensing performance described before. On the one hand, the liquid

molecules absorbed on the surface of rGO decrease the transfer of electron, as shown in Fig. 4.1.10 (b), and thereby decreasing the electrical conductivity of cellulose/rGO composite film. On the other hand, the swelling behaviors of the cellulose matrix by liquid increases the distance between rGO sheets as shown in Fig. 4.1.10 (c), and thereby decreasing the electrical conductivity of the cellulose/rGO composite film.

Fig. 4.1.9 (b) illustrated the R_{rel} changes as function of time for cellulose/rGO (5 wt.%) composite films in different liquids, in order to distinguish water from other liquids over 3 successive cycles. All curves for different liquids are reproducible. Importantly, the maximum value of R_{rel} and the shape of the curves are different, which is ascribed to the varied swelling behavior of cellulose in different solvents. For example, when the composite film is immersed in water, the maximum value of R_{rel} is 460 %, while the value is 20 % when the film is immersed in acetone.

Furthermore, the temperature of the liquid is also another important factor for liquid sensing performance. Fig. 4.1.9 (c) showed the R_{rel} changes as function of time for cellulose/rGO (5 wt.%) composite films in water with temperature over 3 continuous cycles. All curves for different water temperature are reproducible. However, with increasing water temperature, the maximum value of R_{rel} decreases drastically. The relationship between the maximum value of R_{rel} and water temperature is linear, as shown in Fig. 4.1.11. Therefore, our liquid sensor can be used in a wide range of temperature. In addition, the negative temperature coefficient (NTC) is ascribed to semiconductor characteristics of our liquid sensor. With increasing the liquid temperature, the electron transfer from valence states to conduction states in rGO sheets is thermally activated.

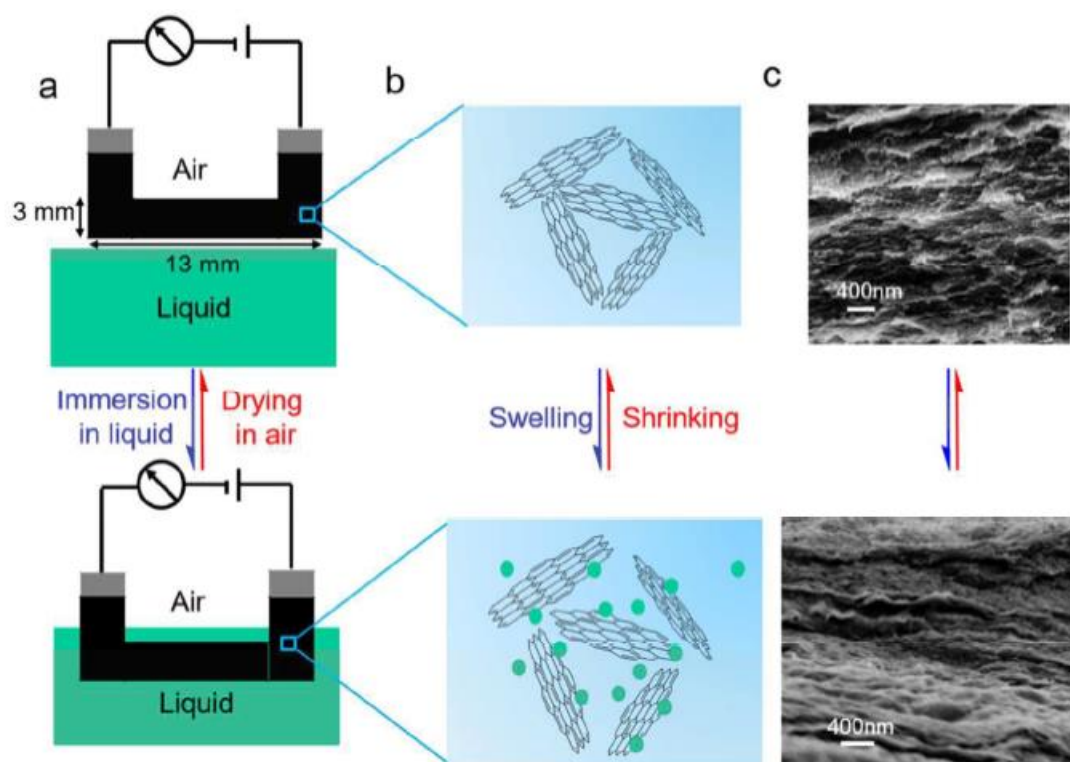


Fig. 4.1.10 (a) Schematic of liquid sensing test. (b) Schematic and (c) SEM images of the cross-section of the cellulose/rGO composite film used for liquid sensing before (top) and after (bottom) immersion into a liquid (150 s).

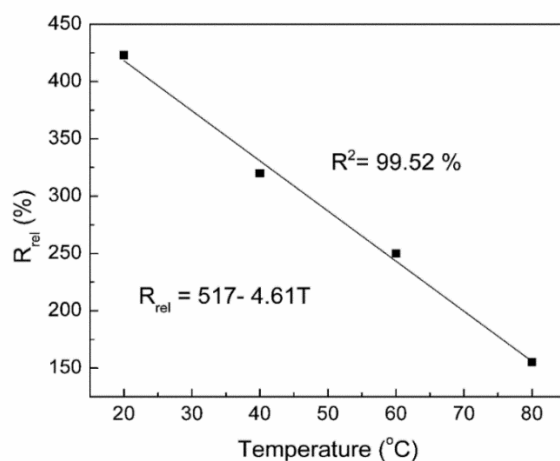


Fig. 4.1.11 R_{rel} after 150 s immersion of the cellulose/rGO (5 wt.%) composites into water depending on water temperature.

Apart from liquid type and temperature, ion concentration detection in liquid is another significant task for liquid sensors. Fig. 4.1.9 (d) shows the R_{rel} changes as function of time for cellulose/rGO (5 wt.%) composite films in water with different NaCl contents over 3 continuous cycles. All curves for all NaCl contents are reproducible. However, with increasing NaCl contents, the maximum value of R_{rel} decreases drastically. The different resistance response of cellulose/rGO (5 wt.%) composite films with different salt concentration can be attributed to the conductivity of the salt water which contributes to the electron transport. Therefore, it can expand the application of our liquid sensors in many fields, such as monitoring of body fluid, seawater, sweat, and so on. For example, our flexible liquid sensors can monitor human sweat to analyze human health by recording the salt concentration.

4.1.7 Vapour sensor of cellulose/rGO composites

The response and recovery properties, as significant factors for assessing the capability of vapour sensors, were investigated. In the vapour sensing part, aerogels are very suitable for vapour adsorption and storage, due to their unique features such as low density, large open pores, and high internal surface area. Thus, we choose composite aerogel instead of composite film. Fig. 4.1.12 (a) displays the resistance response of cellulose/rGO (8 wt.%) aerogels to saturated methanol vapour at room temperature. Before the exposure to methanol vapour, the resistance change was collected for 200 s exposure to dry air to obtain an unwavering R_0 . Then, the aerogel was exposed to methanol vapour and dry air for ten cycles. As we can see, once the aerogel is contacted with methanol vapour, the R_{rel} value of the aerogel increases immediately and reaches about 20 % after about 50 s. After 400 s the R_{rel} value is about 40 %. As shown in Fig. 4.1.12 (b), R_{rel} reached a plateau value (about 45 %) after about 1000 s of exposure. Notedly, it needs a long time to reach the plateau for methanol vapour. For better comparison with other vapours and evaluation of vapour sensitivity in a shorter time, each vapour/dry air cycle is performed by an exposure interval of 400 s followed by a

recovery interval of 200 s in dry air. The fast response performance of the vapour sensor suggests that the cellulose/rGO composite is very sensitive to methanol vapour. Subsequently, the R_{rel} value sharply decreased and quickly recovered to the initial value during the following 200 s of exposure of the cellulose/rGO aerogel to dry air. The curve of the resistance change displays a small hysteresis (2 %) to R_0 , resulting from methanol molecules remaining in the aerogel and some unrecoverable destruction of the initial rGO network caused by swelling. Resistance changes were recorded for ten cyclic runs of methanol vapour exposure and recovery to confirm further the reproducibility. As can be seen from Fig. 4.1.12 (a), very consistent results with each cycle are observed. It is observed that the resistance changes of aerogels and maximum resistance change (about 40 %) are quite stable and reproducible after several cyclic runs of methanol vapour and dry air, suggesting that cellulose/rGO aerogels show a high repeatability characteristic. Clearly, the cellulose/rGO composites show a positive vapour coefficient to methanol vapour. The result is similar to other rGO-based materials for vapour/gas sensing [142, 143]. It is reported previously that the resistance change ΔR of vapour sensor mostly can be divided into two parts: (1) we marked the resistance change resulting from swelling as ΔR_S . The absorption of vapour or gas molecules immediately leads to the swelling of the cellulose matrix, which destroys the electrical connections between the rGO sheets, and this brings about the decrease of the electrical conductivity of the composite aerogel. (2) On the other hand, the adsorbed vapour molecules or gas molecules on the surface of rGO also change the charge carrier concentration of rGO, leading also to an increase of the electrical resistance. We called the resistance change from absorption as ΔR_A . Thereby, $\Delta R = \Delta R_A + \Delta R_S$. The open-porous structure of the cellulose matrix provides some advantages for vapour diffusion and penetration because of their large surface area and numerous vapour channels. Therefore, swelling and de-swelling of the cellulose matrix as well as adsorption and desorption of the vapour molecules on the rGO sheets are fast and effective, which is favorable for triggering the electrical resistance changes.

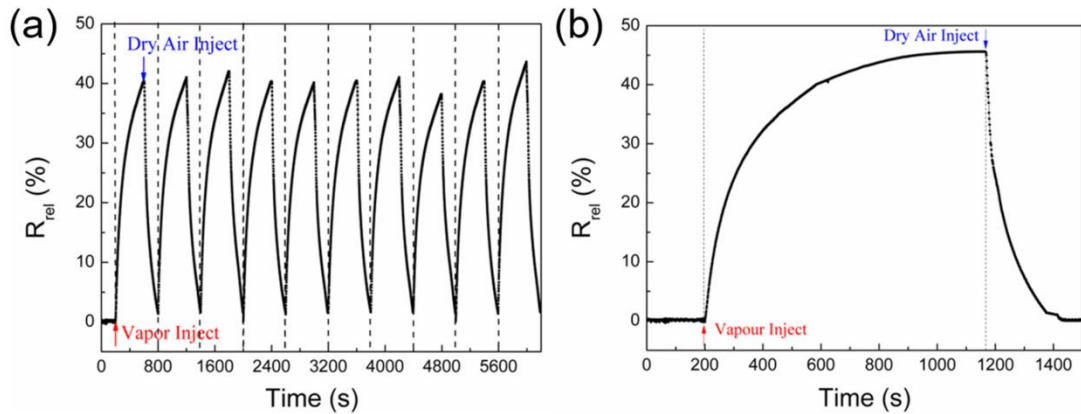


Fig. 4.1.12 The response of resistance of cellulose/rGO (8 wt.%) aerogels to methanol vapour ($C_i = 27.6\%$) at $25\text{ }^\circ\text{C}$. (a) Ten cycles by an exposure interval of 400 s followed by a recovery interval of 200 s in dry air; (b) One complete cycle with the plateau.

The sensitivity of cellulose/rGO aerogel sensor in dependence on filler content was also investigated for methanol. Fig. 4.1.13 shows the R_{rel} values of cellulose/rGO composites with different rGO content. Larger R_{rel} are observed at higher rGO loadings. Similar findings are reported in previous literature with carbon nanotubes (CNTs) [144] and carbon black (CB) [145] containing systems. Notedly, similar resistance changes (35.3 %, 40.2 %) were observed for these composites with 5 wt.% and 8 wt.% rGO loading. On the one hand, a higher rGO loading decreases the probability of destruction of already formed rGO connections through the expansion of cellulose. Thus, ΔR_S is as higher as lower the density of the conductive network is, i.e. just above the electrical percolation concentration. On the other hand, the three-dimensional open porous network of this cellulose aerogel offers efficient contact between methanol vapour and rGO sheets. A higher loading of rGO strongly enhances the relative resistance change driven by the absorption of methanol vapour on rGO sheets. Here, obviously, ΔR_A plays an important role, which relates to an efficient destruction of already formed rGO networks resulting from the absorption of methanol vapour on rGO sheets.

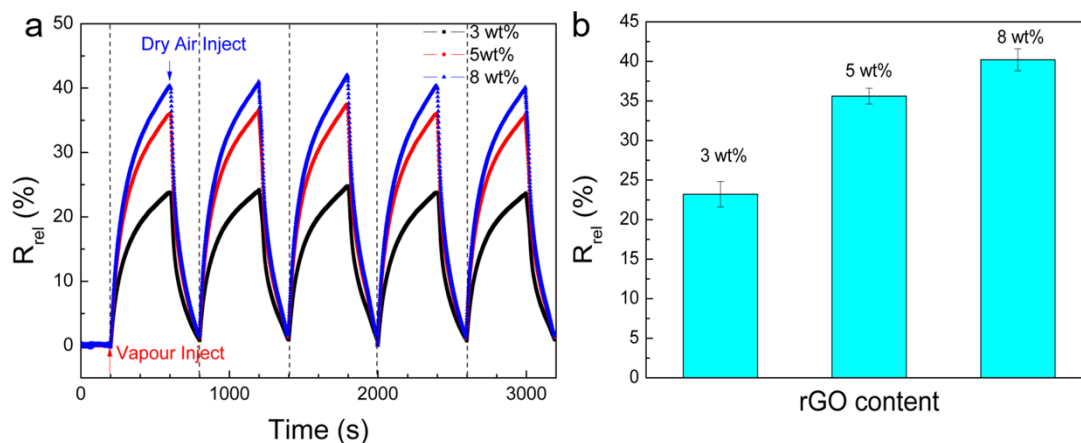


Fig. 4.1.13 (a) R_{rel} of cellulose/rGO composites in dependence on different rGO loadings during exposure to methanol vapour; (b) Mean maximum R_{rel} values of composites with different rGO loadings.

Since the selectivity is an important factor for the evaluation of the vapour sensor performance, different vapours with different polarity, e.g., methanol, ethanol, acetone, water, chloroform, toluene, and tetrahydrofuran (THF) have been studied (Table 4.1.1). From Fig. 4.1.14 (a), the R_{rel} of cellulose/rGO (8 wt.%) composites exposed to four different vapours for five runs are displayed. All curves show positive vapour coefficient and good reproducibility. Moreover, the difference in the maximum resistance changes and the curve shape demonstrate different interactions between the aerogel and vapour molecules. Therefore, it is achievable to distinguish different vapour behaviors when in contact to the aerogel. For example, once the aerogel is in contact with acetone vapour, R_{rel} increased immediately and R_{rel} reached a plateau value after short exposure time. R_{rel} can hardly increase further since the rGO surface sites are already occupied by the acetone molecules reaching a saturated state. Meanwhile, the swelling of cellulose matrix also reached a saturated state. Otherwise, R_{rel} increases steadily during exposure to water molecules, which indicated the slow adsorption of water molecules and slow swelling of cellulose matrix. The mean of the maximum R_{rel} of 5 cyclic exposures of the aerogels to seven different vapours for 400 s versus polar solubility parameter (δ_p) are compared in Fig. 4.1.14 (b). Cellulose, as the

polar material, has affinity to polar solvents (such as water, ethanol, acetone, and methanol), but the correlation to the polarity of the solvent vapours is poor since the signal intensity depends also on the vapour concentration, i.e. the partial vapour pressure of the saturated gases. As shown in Fig. 4.1.14 (b), the polar vapours cause relatively high resistance change responses, with R_{rel} value being about 21-40 %. Despite the relatively low saturated vapour concentration of only 3.2 %, water vapour shows relatively high responses, with R_{rel} value being about 19.6 %. Water molecules lead to a very pronounced swelling of the cellulose matrix, resulting in rather high resistance change. The low vapour pressure of water also explains the steadily increase of R_{rel} during the exposure to water molecules (Fig. 4.1.14 (a)), where no equilibrium is reached after 400 s, but the recovery is fast and nearly complete after 200 s in dry air. Otherwise, vapours with lower polarity such as chloroform and THF show similar relative electrical resistance change response, with the R_{rel} value being about 25.7 and 34.3 %. These solvents have high vapour pressure, resulting in fast filling of the aerogel gels, where they can interact with the matrix and rGO. Consequentially, the vapour with the lowest partial pressure and lowest polarity, in our case toluene, has the smallest effect on the resistivity of the aerogel. Overall, their highly open-porous network structure endows the composite aerogels good sensing performance to both polar and nonpolar vapours, which expands the application potential.

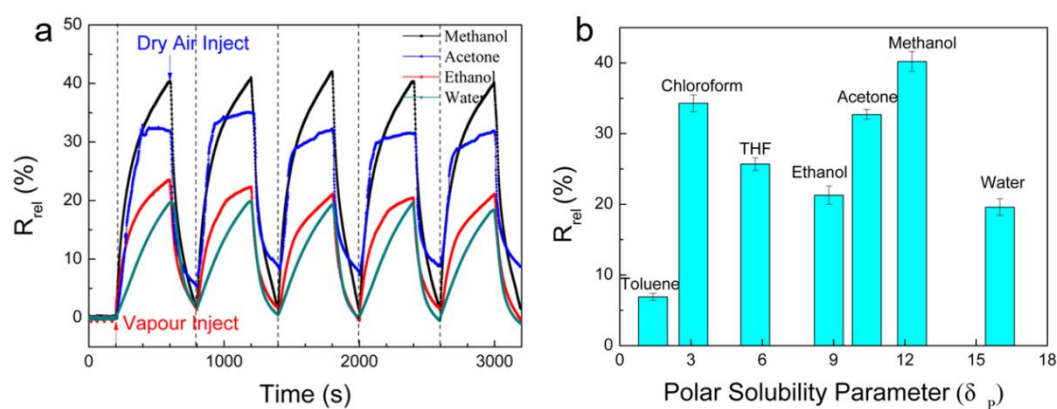


Fig. 4.1.14 (a) R_{rel} of cellulose/rGO aerogels during five vapour/air exposure cycles at 25 °C; (b) the mean R_{rel} values after exposure to vapours for 400 s.

Table 4.1.1 Different solvents with chemical formulas, solubility parameter from polar bonds between the molecules (δ_p) [146], saturated partial pressure (P_i), saturated vapour concentration (C_i), and the mean of the maximum relative electrical resistance change (R_{rel}) after 400 s at 25 °C.

Solvent	Chemical formulas	δ_p (MPa)	P_i (kPa)	C_i (%)	R_{rel} (%)
Water	H ₂ O	16.0	3.2	3.2	19.6
Methanol	CH ₃ OH	12.3	28.0	27.6	40.2
Ethanol	CH ₃ CH ₂ OH	8.8	8.0	7.9	21.3
Acetone	CH ₃ OCH ₃	10.4	30.6	30.2	32.7
Toluene	C ₆ H ₅ CH ₃	1.4	3.8	3.8	6.9
THF	(CH ₂) ₄ O	5.7	23.5	23.2	25.7
Chloroform	CHCl ₃	3.1	80.7	79.6	34.3

Finally, the quantitative performance of cellulose/rGO (8 wt.%) aerogels for vapour sensing was also tested. Fig. 4.1.15 displays the real-time resistance measurement of the vapour sensor with different contents of methanol vapour at 25 °C. The cycling test is carried out with different methanol vapour concentrations in order of 6.9 %, 13.8 %, 20.7 % and 27.6 % and then conversely from high to low concentration. Each vapour/dry air cycle is performed by an exposure interval of 400 s followed by a recovery interval of 200 s in dry air. The aerogel shows good recovery and fast response for methanol vapours with different concentrations. A clear correlation of the R_{rel} is observed with increasing and, more important, with decreasing methanol vapour concentration. This demonstrates that the aerogel has the potential for quantitative tests of vapour contents at room temperature. Moreover, the R_{rel} values show nearly linear growth with methanol vapour concentrations, as shown in Fig. 4.1.15 (b), while an exponential increase is observed in other materials as vapour sensors [147, 148]. For

such CPC sensor types, the exponential increase could be explained by a well-established sorption model reported by Feller et al. [149] and is due to solubility increase along with cellulose swelling and penetrant clustering of vapour molecules [150]. Here, this model is not applicable since adsorption and desorption on the conductive filler are dominating the resistance change.

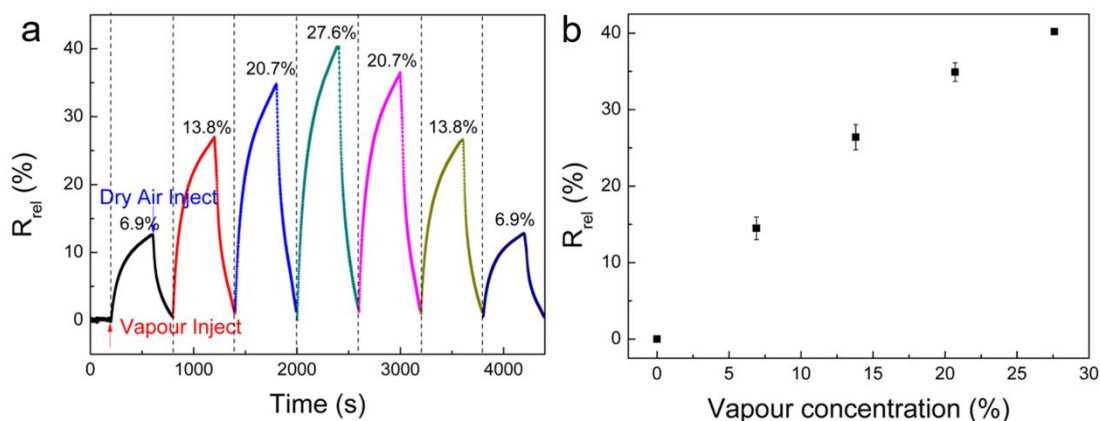


Fig. 4.1.15 (a) R_{rel} of the cellulose/rGO (8 wt.%) composites with different contents of methanol vapour at 25 °C; (b) the mean R_{rel} values after exposure to vapours for 400 s with different contents of methanol vapour at 25 °C.

4.1.8 Summary

The cellulose/rGO composite films and aerogels are fabricated by NaOH/urea solution to dissolve cellulose and disperse GO and followed by in-situ reduction of GO. Vitamin C, which is used here as the reduction agent, shows not only good reduction characteristics but also stands out as an eco-friendly and non-toxic materials. The resultant cellulose/rGO composite prepared by this efficient and simple method show high resistance sensitivity to environmental temperature, humidity, liquid, vapour, and strain stress. At the same time, the cellulose/rGO films can be applied in detecting the human motions and human breath cycles. Liquid temperature, liquid type, and ion concentration were also detected by our cellulose/rGO films. Moreover, the composite aerogels prepared from the same material have the capability of being fast response,

extremely sensitive, and good repeatable sensors for vapours detection and testing. It was also revealed that discriminating and quantitative responses can be obtained in various vapours and different contents of vapour. For methanol vapour, the aerogel shows linear response to the vapour concentration. This makes the cellulose/rGO composite aerogel to a candidate to quantify methanol vapour. The efficient, scalable, and environmentally friendly preparation of novel and high-performance of vapour sensing materials with high reproducibility is believed to develop an efficient method and approach to achieve material for vapour sensing application.

As an outlook, besides the excellent potential applications in sensors, the approach is also applicable for other functional properties for application in fields such as catalysis, photonics, and optoelectronics. The presence of functional groups on GO also provides opportunities for tailoring its chemical functionality. Thus, the cellulose/GO hydrogel can also serve as a novel platform, which can design various materials based on GO (or rGO, modified GO, and modified rGO) and cellulose. Furthermore, by combining highly open-porous cellulose matrix with the nature of rGO, cellulose/rGO composite aerogels serve as a new platform for designing a new class of multifunctional sensing materials.

4.2. Cellulose/GO/Fe₃O₄ hydrogels for advanced catalytic materials for the heterogeneous Fenton-like reaction

Note: The results presented in chapter 4.2 are published in my paper “Fe₃O₄ Nanoparticles Grown on Cellulose/GO Hydrogels as Advanced Catalytic Materials for the Heterogeneous Fenton-like Reaction” (ACS Omega 2019, 4, 5117-5125) with the co-authors Petra Pötschke, Jürgen Pionteck, Brigitte Voit, and Haisong Qi.

4.2.1 Introduction

At present, dye wastewaters generated by textile, paper, and plastic industries are a major source of water pollution. The dye compounds are difficult to destruct and very stable, due to their aromatic structure. Recently, advanced oxidation processes (AOPs), as a promising and robust approach, were widely used to decontaminate dye wastewater. AOPs have many attractive advantages such as high degradation efficiency and low toxicity. The mechanism of AOPs in destruction of dye is based on the formation of highly reactive hydroxyl radicals (HO•) to break down dye into smaller and non-toxic substances [151]. Among AOPs, Fenton's agent, based on hydrogen peroxide (H₂O₂) and ferrous ion (Fe²⁺), is an attractive and efficient source for the generation of HO• and the non-selective degradation of dye compounds [152, 153]. It should be noted that the homogeneous Fenton- or Fenton-like methods still have many disadvantages such as, the expensive treatment of iron hydroxide sludge and the difficulties in recycling of the catalyst [154, 155]. Therefore, heterogeneous Fenton-like catalysts were designed to overcome these disadvantages. In general, the iron species are coated on the surface of catalyst supports, such as silica [156], alumina [157, 158], clay [159, 160], zeolite [161], and carbonaceous materials [162, 163]. Specially, carbonaceous materials, such as CNTs [164, 165], carbon aerogels [166, 167], activated carbon (AC) [168, 169], and mesoporous carbon [170] have been well proven as promising catalyst carriers, due to their special catalytic performance as co-catalyst with the iron species. Recently, Voitko et al. [171] investigated the degradation performance of GO, which is much better than

that of CNTs and AC. This phenomenon is due to functional groups on the surface of GO sheets. Due to the difficulty in recycling of the catalyst, using GO in heterogeneous Fenton-like catalysts has been scarcely reported. Zubir et al. [172] prepared GO/Fe₃O₄ composites as a co-catalyst. Synergistic effect of GO and Fe₃O₄ bring about good and stable catalytic properties. However, this co-catalyst also has many disadvantages, such as the limitation of the convenient use and difficulty in taking off the co-catalyst.

Here, we prepared cellulose/GO/Fe₃O₄ hydrogel by coating cellulose/GO hydrogel with Fe₃O₄ for use in a Fenton-like reaction system. As described in Part 4.1, we have successfully prepared cellulose/GO hydrogels as the starting material by NaOH/urea solution. On the one hand, the cellulose/GO hydrogel is beneficial for the diffusion and reaction of Fe²⁺ and Fe³⁺. On the other hand, the hydrogel can maintain its structure and shape during the degradation process. Therefore, we can easily take the hydrogel off after degradation process, which avoids secondary pollution. Moreover, cellulose/GO/Fe₃O₄ hydrogel as the catalytic material can control the start and end of the reaction by taking in and off cellulose/GO/Fe₃O₄ hydrogel during the reaction process. In this work, acid orange 7 (AO7) is chosen as a model pollutant, a widely used dye in the textile, paper, and pulp industry. Therefore, the aim of this work was to evaluate the catalytic performance of cellulose/GO/Fe₃O₄ to degrade AO7. Moreover, the influence of initial pH, initial AO7 dye concentration, temperature, and the initial concentration of H₂O₂ on the catalytic performance was studied.

4.2.2 Structure and morphological analysis of cellulose/GO/Fe₃O₄ composites

The preparation of cellulose/GO/Fe₃O₄ composites is shown in experimental part (Fig. 3.2.2). We used the NaOH/urea aqueous solution in the first step to prepare the cellulose/GO hydrogel since the NaOH/urea aqueous solution was found to facilitate good dispersion of GO in the cellulose matrix. When the cellulose/GO hydrogel was immersed in the FeCl₃/FeCl₂ solution, Fe³⁺/Fe²⁺ were adsorbed around the carboxyl and hydroxyl groups of the cellulose and the GO sheets. Afterwards, when NaOH was

added into the solution, $\text{Fe}^{3+}/\text{Fe}^{2+}$ were hydrolysed to generate $\text{Fe}(\text{OH})_3/\text{Fe}(\text{OH})_2$. After the condensation of $\text{Fe}(\text{OH})_3/\text{Fe}(\text{OH})_2$, Fe_3O_4 were immobilized in the cellulose/GO hydrogel.

The structure and morphology of cellulose/GO/ Fe_3O_4 composites were characterized by TEM, XPS, FTIR, and XPS measurements (Fig. 4.2.1). As shown in Fig. 4.2.1 (a) and (b) on thin cuts of the composites, the interface of cellulose matrix and GO sheets are densely and evenly coated by Fe_3O_4 with a narrowly distributed average size of 10~13 nm (Fig. 4.2.1 (c)). The wide scan XPS spectra of cellulose/GO and cellulose/GO/ Fe_3O_4 composites are shown in Fig. 4.2.1 (d) to confirm the generation of Fe_3O_4 . The spectra of different cellulose/GO/ Fe_3O_4 composites display three characteristic peaks at 711, 530, and 285 eV, representing Fe 2p, O 1s and, C 1s respectively. More detailed XPS information of cellulose, cellulose/GO, and cellulose/GO/ Fe_3O_4 composites are given in Fig. 4.2.2. The high-resolution scan of Fe 2p XPS spectra are illustrated in Fig. 4.2.2 (b). The spectra of different cellulose/GO/ Fe_3O_4 composites and pure Fe_3O_4 all show two characteristic peaks at 724.7 and 711.2 eV, which are corresponding to Fe $2p_{1/2}$ and Fe $2p_{3/2}$, respectively. These results agree with the case reported in the literature for Fe_3O_4 [173]. Moreover, the charge transfer satellite of Fe $2p_{3/2}$ at about 720 eV was not detected, indicating the generation of Fe_3O_4 in the cellulose/GO hydrogel. FTIR spectra of cellulose/GO and cellulose/GO/ Fe_3O_4 composites are shown in Fig. 4.2.1 (e) to confirm the generation of Fe_3O_4 . The FTIR spectrum of cellulose/GO (8 wt.%)/ Fe_3O_4 composite shows a characteristic peak at around 584 cm^{-1} , which is corresponding to Fe-O. Fig. 4.2.1 (f) shows the XRD spectra of cellulose/GO and cellulose/GO/ Fe_3O_4 composites to study the crystal structure of Fe_3O_4 and confirm the formation of Fe_3O_4 . The XRD diffraction peak of cellulose/GO (8 wt.%)/ Fe_3O_4 composite at $2\theta = 30.3^\circ, 35.4^\circ, 43.3^\circ, 53.6^\circ, 57.2^\circ,$ and 62.9° , corresponding to (220), (311), (400), (422), (511), and (440) planes, respectively. All the peaks in cellulose/GO (8 wt.%)/ Fe_3O_4 composite reveal the formation of Fe_3O_4 , as reported in the literature [174, 175].

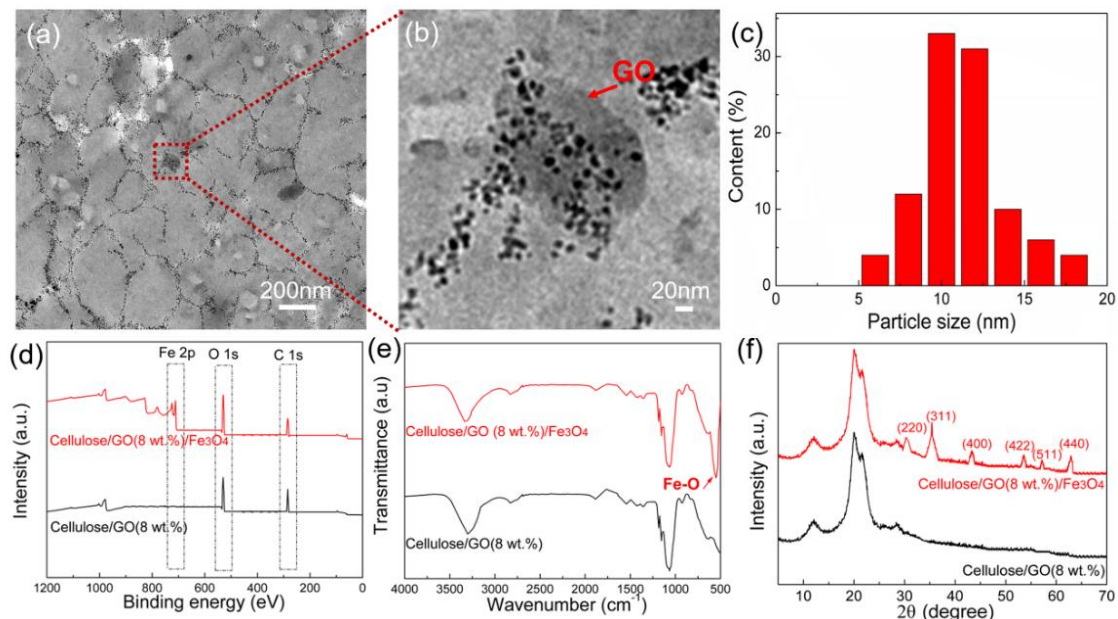


Fig. 4.2.1 (a) Low magnification and (b) high magnification TEM images of Fe₃O₄ nanoparticles grown on GO sheets. (c) Fe₃O₄ nanoparticles size distribution as determined from TEM micrographs. (d) Wide scan XPS spectra of cellulose/GO (8 wt.%) and cellulose/GO (8 wt.%) / Fe₃O₄. (e) FTIR spectra of cellulose/GO (8 wt.%) and cellulose/GO (8 wt.%) / Fe₃O₄. (f) XRD spectra of cellulose/GO (8 wt.%) and cellulose/GO (8 wt.%) / Fe₃O₄.

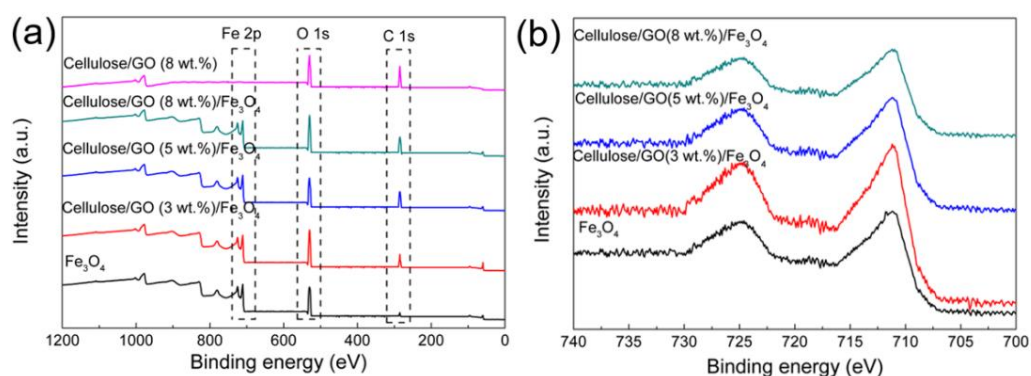


Fig. 4.2.2 (a) Wide scan XPS spectra and (b) high resolution Fe 2p spectra of different nanocomposites and Fe₃O₄ nanoparticles.

To calculate the content of Fe₃O₄ nanoparticles, the thermal degradation behavior of cellulose, cellulose/GO, and cellulose/GO/Fe₃O₄ composites was studied with raising temperature from room temperature to 800 °C under nitrogen atmosphere (Fig. 4.2.3 (a)). The residues of different composites with and without Fe₃O₄ determined from Fig. 4.2.3 (a) are presented in Fig. 4.2.3 (b). The content of Fe₃O₄ in different cellulose/GO/Fe₃O₄ composite increased by increasing GO contents. With more addition of GO which contain plenty of oxygen-containing groups into cellulose-based hydrogel, more Fe³⁺/Fe²⁺ were adsorbed around the carboxyl and hydroxyl groups of the GO sheets and thus more Fe₃O₄ nanoparticles were generated during the preparation method.

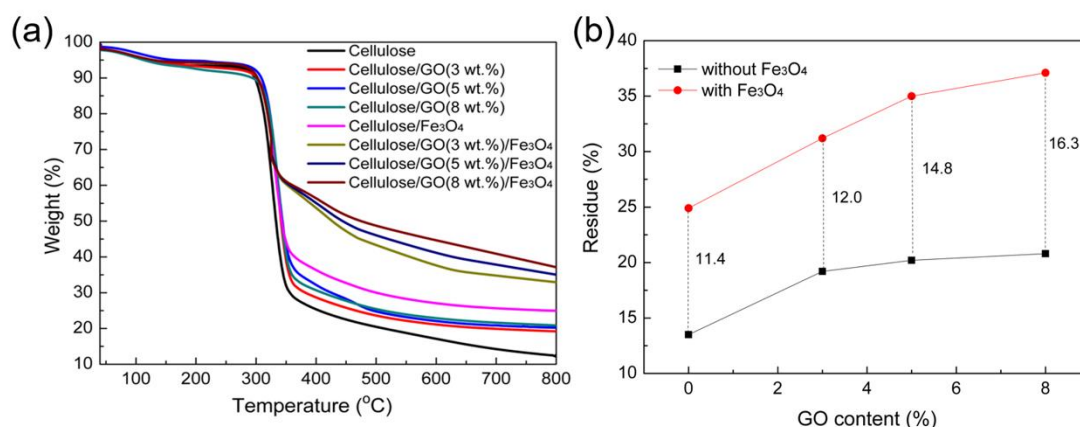


Fig. 4.2.3 (a) TGA curves of different composites and cellulose. (b) Residues of cellulose/GO and cellulose/GO/Fe₃O₄ composites.

4.2.3 Optimization analysis of the AO7 degradation conditions

Here, cellulose/GO (8 wt.+)/Fe₃O₄ hydrogel was selected as a standard sample for the optimization of the AO7 degradation conditions. The degradation behavior of AO7 as function of the initial concentration of AO7 is described in Fig. 4.2.4 (a). The degradation rate of AO7 decreased with increasing the AO7 concentration. This

phenomenon is attributed to that the active sites of the hydrogel were surrounded by excess AO7 when the concentration of AO7 was high, resulting the retarding effect. The degradation performance of AO7 as function of the temperature is described in Fig. 4.2.4 (b). High temperature is beneficial for the fast rate of AO7 degradation. For example, it takes 15 minutes at 338 K to reach 64 % degradation of AO7, while, it needs as long as 45 minutes to reach the same degradation of AO7 at 298 K. This result is ascribed to that the diffusion and mobility of AO7 and H₂O₂ in the cellulose/GO (8 wt.%)/Fe₃O₄ hydrogel was promoted by high temperature. Thus, high temperature is conducive to the acceleration of AO7 degradation. However, for the sake of energy saving, 298 K was still chosen as the reaction temperature in further optimization of the degradation conditions. Fig. 4.2.4 (c) shows the effect of the H₂O₂ concentration on the degradation of AO7. The degradation of AO7 concentration after 180 min. increased from 80 % to 98 % with the increasing of H₂O₂ concentration from 5.5 mM to 22 mM. However, further increase of the H₂O₂ concentration to 33 mM resulted in only 82 % degradation of AO7, indicating that the resulting HO• can be consumed by excess H₂O₂ to form hydroperoxyl radicals (HOO•) [176]. Fig. 4.2.4 (d) illustrates the influence of initial pH on the AO7 oxidation. Obviously, the best pH value for the degradation of AO7 is around 3. The degradation of AO7 decreased with the increasing of pH, when pH is greater than 3. It demonstrated that more H₂O₂ was decomposed to molecular oxygen. Conversely, the degradation of AO7 increased with the increasing of pH, when pH is less than 3. This phenomenon is due to the scavenging effect of HO• caused by excess H⁺. Therefore, the experimental condition selected for in the following catalytic activity tests of different cellulose/GO, cellulose/Fe₃O₄, and cellulose/GO/Fe₃O₄ composites are: [AO7] = 0.1 mM, T = 298 K, [H₂O₂] = 22 mM, and pH = 3.

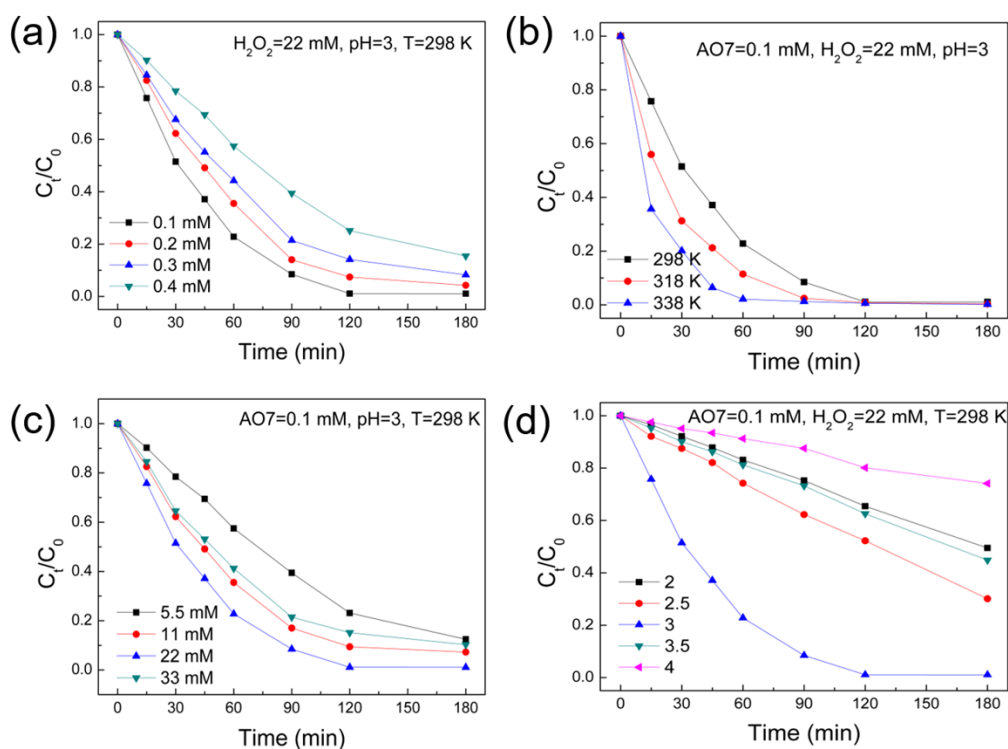


Fig. 4.2.4 (a) Effect of the initial AO7 concentration on the degradation of AO7 by H_2O_2 catalysed with cellulose/GO (8 wt.)/ Fe_3O_4 composite. (b) Effect of temperature on the degradation of AO7 by H_2O_2 catalysed with cellulose/GO (8 wt.)/ Fe_3O_4 composite. (c) Effect of H_2O_2 content for AO7 oxidation by H_2O_2 catalysed with cellulose/GO (8 wt.)/ Fe_3O_4 composite. (d) Effect of pH on the degradation of AO7 by H_2O_2 catalysed with cellulose/GO (8 wt.)/ Fe_3O_4 composite.

4.2.4 Catalytic activity of cellulose/GO/ Fe_3O_4 hydrogels

Fig. 4.2.5 (a) displays UV-vis absorption spectra of cellulose/GO (8 wt.)/ Fe_3O_4 catalyzed AO7 degradation by H_2O_2 . The two AO7 structures are characterized by two bands in visible region located at 484 and 430 nm, respectively. These absorbance peaks are ascribed to hydrazine and azo form of AO7, respectively. The other two bands in the ultraviolet region located at 230 and 310 nm are due to the benzene and naphthalene rings of AO7, respectively [34]. With increased reaction time, these four

characteristic bands significantly reduced with reaction time and almost disappeared after 120 min. These results indicate that the auxochromic and chromophoric structures of the AO7 dye was totally destructed during the heterogeneous Fenton-like reactions.

Fig. 4.2.5 (b) illustrates the removal of AO7 as function of reaction time for different systems. In the presence of only H₂O₂, the degradation of the AO7 dye was negligible during the non-catalysed reaction. This phenomenon can be ascribed to the low oxidation potential of H₂O₂ as compared to HO• radicals. For cellulose/GO (8 wt.%) and cellulose/Fe₃O₄ systems, 23 % and 64 % removal of AO7 dye was achieved after 180 min of reaction, respectively. When both GO and Fe₃O₄ are present in the cellulose composites, 71 to 98 % AO7 were removed after 180 min., increasing with the GO content in the composite.

The higher AO7 removal caused by cellulose/GO/Fe₃O₄ composites compared to cellulose/GO and cellulose/Fe₃O₄ composites is attributed to the co-effect between GO and Fe₃O₄. Firstly, since AO7 contains aromatic units as shown in Fig. 4.2.5 (a), the aromatic ring structures of GO sheets are beneficial for the adsorption of AO7 by π - π interactions. Therefore, it can increase the concentration of AO7 near the active sites [174] and boost the degradation of AO7 in the direct neighborhood [162]. Secondly, the electron transport between Fe₃O₄ and GO is beneficial for acceleration of redox cycle and thereby achieve the regeneration of Fe²⁺, which is a crucial factor for the generation of more HO• radicals. Concluding, the high catalytic cellulose/GO/Fe₃O₄ hydrogels performance for degradation of AO7 is due to the morphological and structural interactions between GO and Fe₃O₄.

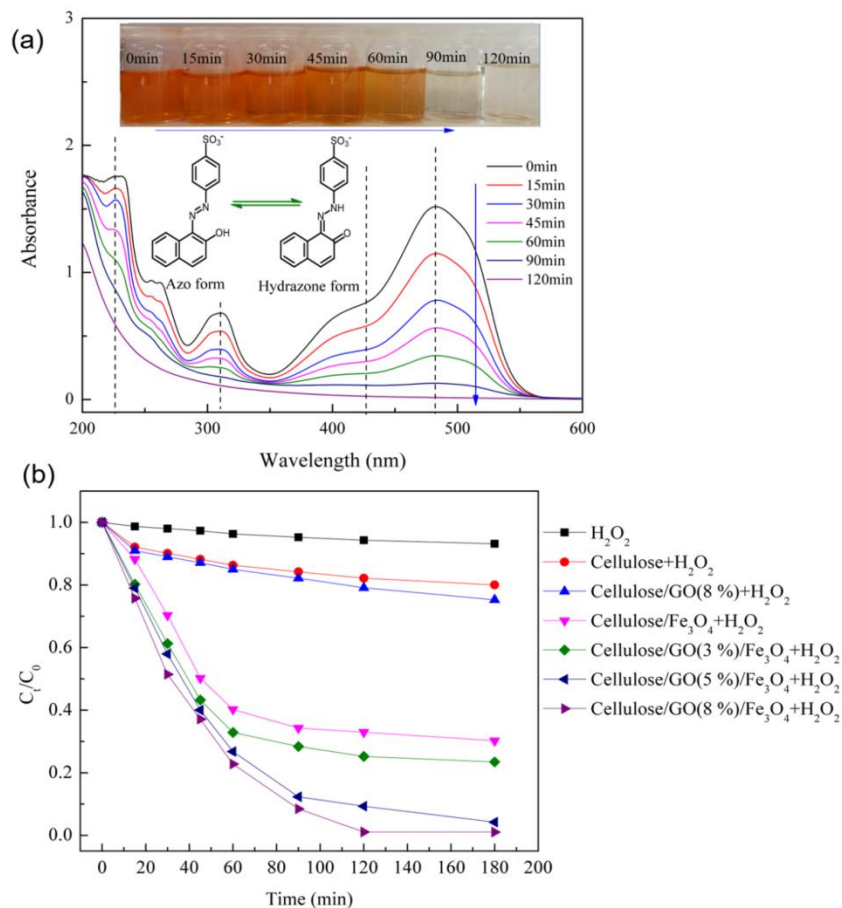


Fig. 4.2.5 (a) UV-vis analysis of the degradation of AO7 by H_2O_2 catalyzed with cellulose/GO (8 wt.%)/ Fe_3O_4 composite. (b) Effect of catalysts on degradation profiles of AO7 ($[\text{AO7}] = 0.1 \text{ mM}$, $[\text{catalyst}] = 0.2 \text{ g L}^{-1}$, $\text{pH} = 3$, $[\text{H}_2\text{O}_2] = 22 \text{ mM}$, and $T = 298 \text{ K}$).

To demonstrate the durability of our hydrogel as the catalyst, Fig. 4.2.6 (a) shows the removal of AO7 as function of reaction time for cellulose/GO/ Fe_3O_4 hydrogels over 20 consecutive cycles with each cycle lasting 180 min. After each cycle, hydrogel was taken from the solution, washed thoroughly with deionized water, and then used for the degradation of a fresh AO7 solution. As shown in Fig. 4.2.6 (a), the decrease of AO7 removal is negligible over 5 consecutive cycles. There is only small decrease of AO7 removal after 20 consecutive cycles, demonstrating the durability of our hydrogel as catalyst.

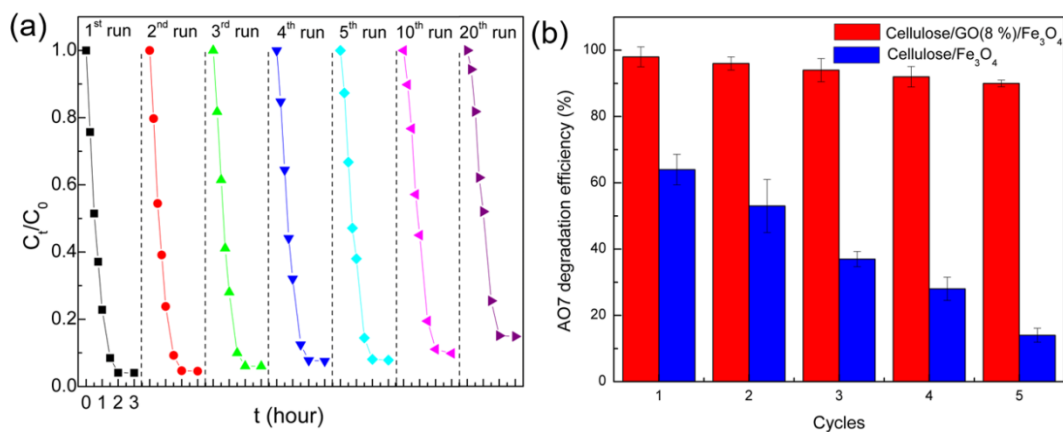


Fig. 4.2.6 (a) Consecutive cycles of AO7 degradation using cellulose/GO (8 wt.)/Fe₃O₄ composites. (b) The long-term stability of the catalytic activity of the composites was tested by repeated use for AO7 degradation.

As shown in Fig. 4.2.6 (b), the cellulose/GO (8 wt.)/Fe₃O₄ hydrogels show better stability in the removal of AO7 dye over 5 consecutive cycles as compared with cellulose/Fe₃O₄ hydrogel, which is not just less effective in AO7 degradation but also exhibits less catalytic stability. Using cellulose/Fe₃O₄ hydrogel as catalyst, in the first cycle 64 % of AO7 are destroyed, while the degradation reduces to just 14 % in the fifth cycle. The durability performance of cellulose/GO/Fe₃O₄ hydrogels for the degradation of AO7 dye over 20 consecutive cycles was greatly due to the syngenetic effect between Fe₃O₄ and GO. The formation of passivated Fe₃O₄ on the surface of the cellulose/Fe₃O₄ hydrogel resulted in the ineffective regeneration of Fe²⁺ and thereby brought about the low AO7 removal over 20 consecutive cycles. In the case of cellulose/GO/Fe₃O₄ hydrogels, the electron transport between Fe₃O₄ and GO is beneficial for acceleration of the redox cycle and thereby regeneration of Fe²⁺, which result in the loss of surface passivation of our hydrogels and thus durability of the catalyst.

The regeneration of Fe^{2+} in different systems was demonstrated by the detailed XPS results. As shown in Fig. 4.2.7 (a) and (b), the Fe 2p spectra of cellulose/GO (8 wt.%)/ Fe_3O_4 hydrogels and cellulose/ Fe_3O_4 hydrogels show two peaks at 724.6 eV and 711.1 eV, which are corresponding to $\text{Fe } 2p_{1/2}$ and $\text{Fe } 2p_{3/2}$, respectively. The deconvolution of these two peaks into Fe^{3+} and Fe^{2+} demonstrated the regeneration of Fe^{2+} by quantifying the ratio of $\text{Fe}^{3+}/\text{Fe}^{2+}$. Table 4.2.1 summarizes the detailed information of Fe^{2+} and Fe^{3+} peaks and the calculated ratios of $\text{Fe}^{3+}/\text{Fe}^{2+}$. In the cellulose/ Fe_3O_4 system, the ratio of $\text{Fe}^{3+}/\text{Fe}^{2+}$ significantly increased from 2.02 to 4.56 after 20 cycles of use for AO7 degradation, but in the cellulose/GO/ Fe_3O_4 system the ratio of $\text{Fe}^{3+}/\text{Fe}^{2+}$ remains nearly unchanged during 20 consecutive cycles, which is attributed to the efficient regeneration of Fe^{2+} during 20 consecutive cycles.. These XPS results plausibly demonstrate the excellent regeneration of Fe^{2+} of cellulose/GO/ Fe_3O_4 hydrogels. These XPS results are in line with the high removal performance of cellulose/GO/ Fe_3O_4 hydrogels, as shown in Fig. 4.2.5 and Fig. 4.2.6.

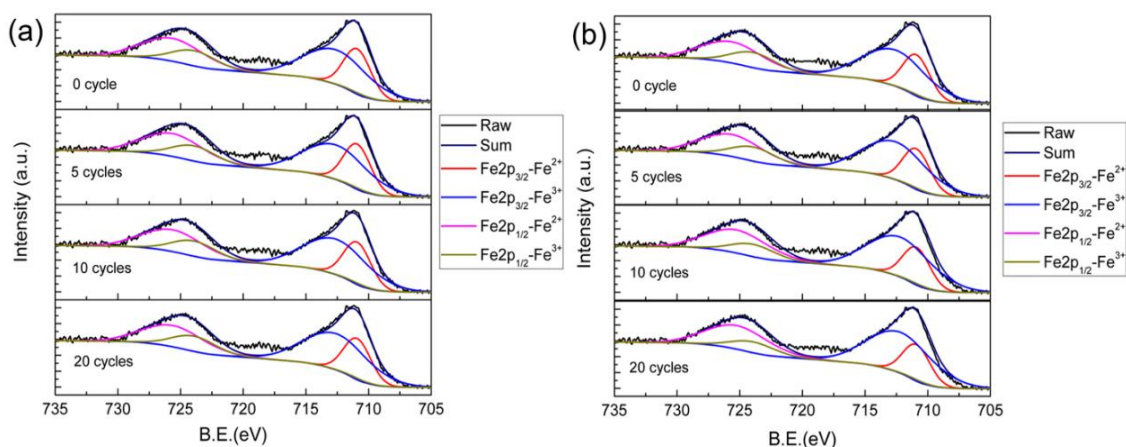


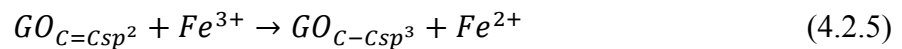
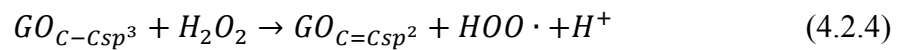
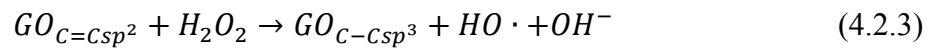
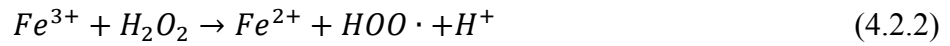
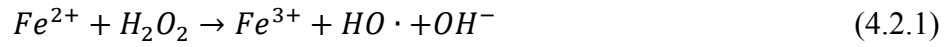
Fig. 4.2.7 XPS spectra of (a) cellulose/GO (8 wt.%)/ Fe_3O_4 composites and (b) cellulose/ Fe_3O_4 composites taken after different cycle numbers of use for AO7 degradation.

Table 4.2.1 The atomic iron composition and calculated $\text{Fe}^{3+}/\text{Fe}^{2+}$ ratio of cellulose/GO (8 wt.%)/ Fe_3O_4 and cellulose/ Fe_3O_4 composites in dependence of cycle number.

Samples	Cycles	Fe 2p _{1/2}		Fe 2p _{3/2}		$\text{Fe}^{3+}/\text{Fe}^{2+}$ ratio
		Fe^{3+} (%)	Fe^{2+} (%)	Fe^{3+} (%)	Fe^{2+} (%)	
Cellulose/GO/ Fe_3O_4	0	22.1	8.14	44.7	24.9	2.02
	1	21.4	7.36	45.4	25.7	2.02
	3	22.5	8.01	44.2	25.2	2.01
	5	22.4	7.95	44.2	25.3	2.00
	10	22.4	7.75	44.4	25.3	2.02
	20	22.9	8.10	43.4	25.5	2.05
Cellulose/ Fe_3O_4	0	22.0	7.77	44.7	25.4	2.02
	1	21.9	8.45	48.1	21.5	2.34
	3	22.4	8.35	49.5	19.7	2.56
	5	21.9	6.14	54.0	18.0	3.14
	10	24.1	3.60	55.3	16.8	3.89
	20	24.9	3.62	57.1	14.4	4.56

In summary, the cellulose/GO/ Fe_3O_4 hydrogels used for the removal of AO7 exhibits excellent durability and high performance. A proposed mechanism explaining these results is illustrated in Fig. 4.2.8. The reaction mechanism is given in Eq. 4.2.1 to 4.2.5 [177]. Firstly, the formation of $\text{HO}\cdot$ radicals mainly arises from the degradation

of absorbed H_2O_2 on the active sites of Fe_3O_4 (Eq. 4.2.1 and 4.2.2). Secondly, apart from Fe_3O_4 , the formation of $HO\cdot$ radicals also results from the degradation of absorbed H_2O_2 due to the electron transfer mechanism in GO sheets [178] (Eq. 4.2.3 and 4.2.4). Thirdly, since GO contains many π -conjugated sp^2 carbon domains [179], π electrons on the surface of GO bring about electron transfer between Fe_3O_4 and GO [180]. The feasibility of this electron transfer between Fe_3O_4 and GO is due to that the standard reduction potential of Fe^{3+}/Fe^{2+} (+0.771 V) [164] is much higher than that of GO (-0.19 V) [181]. Thus, in the presence of GO sheets Fe^{2+} regenerates spontaneously from Fe^{3+} . The possible regeneration of Fe^{2+} by H_2O_2 , as show in Eq. 4.2.2, is difficult to achieve, but the interaction between Fe_3O_4 and GO sheets speeds up the redox cycles and the regeneration of Fe^{2+} (Eq. 4.2.5). This efficient regeneration of Fe^{2+} greatly promoted the formation of $HO\cdot$ radicals. Overall, the redox cycle from Fe^{3+} to Fe^{2+} is a key factor in the excellent and stable catalytic degradation of AO7.



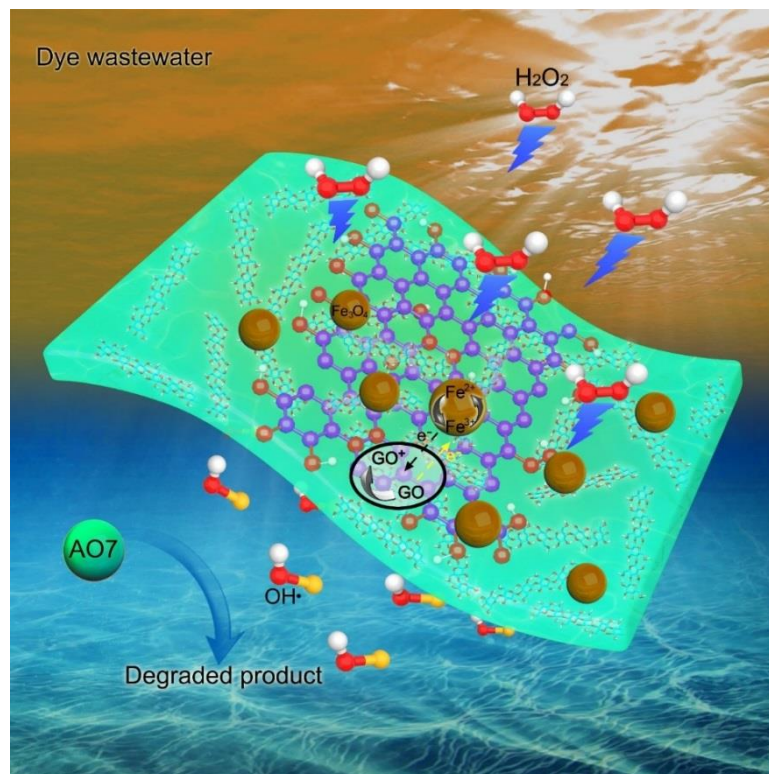


Fig. 4.2.8 Proposed mechanism of cellulose/GO/Fe₃O₄ hydrogel as catalyst to degrade AO7.

The stability of our cellulose/GO/Fe₃O₄ hydrogel and the percentage of AO7 removal is compared with other works reported in literature in Table 4.2.2 at similar operational conditions to have a rough estimation. Our cellulose/GO/Fe₃O₄ hydrogel is comparatively stable and achieved high AO7 removal. Here, another obvious convenience of our system is that the cellulose/GO/Fe₃O₄ hydrogel structure could be maintained over several cycles. This convenience will not bring about secondary pollution. Our hydrogel can be easily removed from the reaction solution after the degradation reaction. Cellulose/GO/Fe₃O₄ hydrogel as the catalytic material can control the start and end of the reaction by taking in and off cellulose/GO/Fe₃O₄ hydrogel during the reaction process. Obviously, our cellulose/GO/Fe₃O₄ hydrogel is very useful for the removal of AO7.

Table 4.2.2 Degradation performance and stability of different systems

Dyes	Catalyst	Percentage of removal	Stability	Conditions	Refs.
AO7	GO/Fe ₃ O ₄	80.0 % in 20 min 98.0 % in 180 min		pH 3; 0.1 mM dye; 22 mM H ₂ O ₂ ; 298 K	[172]
AO7	BiOI/ZnFe ₂ O ₄	90.5 % in 180 min		pH 5; 20 mg L ⁻¹ dye; 298 K	[182]
AO7	Pillared saponite clay impregnated with Fe(II) acetylacetonate	91.8 % in 180 min		pH 5; 0.1 mM dye; 20 mM H ₂ O ₂ ; 303 K	[183]
AO7	BiOI-BiOCl/C ₃ N ₄	96.6 % in 140 min	87.4 % in 140 min after the 4 th run	pH 6; 0.1 mM dye; 20 mM H ₂ O ₂ ; 303 K	[184]
AO7	CdO-ZnO	69 % in 140 min		pH 7; 20 mg L ⁻¹ dye; 298 K	[185]
AO7	Cd-TiO ₂	95 % in 120 min		pH 2; 20 mg L ⁻¹ dye; 298 K	[186]
AO7	Ag-ZnO/CNT	98 % in 120 min	95 % in 120 min after the 4 th run	pH 5; 20 mg L ⁻¹ dye; 298 K	[187]
AO7	Cellulose/GO (8 wt%)/Fe ₃ O ₄ hydrogel	97 % in 120 min 98 % in 180 min	90 % in 180 min after the 20 th run	pH 3; 0.1 mM dye; 22 mM H ₂ O ₂ ; 298 K	This work

4.2.5 Summary

In conclusion, we have successfully presented an effective, facial, simple, and scalable method to form Fe₃O₄ nanoparticles onto cellulose/GO hydrogels. XRD, FTIR, XPS, and TEM indicated that Fe₃O₄ nanoparticles with good dispersion and uniform size were successfully coated on cellulose matrix and GO sheets. The optimized experimental conditions for AO7 degradation are: [AO7] = 0.1 mM, T = 298 K, [H₂O₂] = 22 mM, and pH = 3. Under these conditions, the resulting hydrogels display 97 % AO7 removal within 120 min and retained strong degradation performance after twenty consecutive cycles of reuse. Especially, the detailed XPS analysis of cellulose/GO/Fe₃O₄ and cellulose/Fe₃O₄ composites indicated that the cellulose/GO/Fe₃O₄ hydrogel retains its high degradation activity by keeping the ratio of Fe³⁺/Fe²⁺ at 2 during the 20 heterogeneous Fenton-like reaction cycles. Therefore, the cellulose/GO/Fe₃O₄ hydrogel is recommended to treat other dye-contaminated wastewaters.

4.3. Cellulose/rGO/Fe₃O₄ aerogels for EMI shielding application

Note: The work described in chapter 4.3 has been submitted for publication to ACS Applied Materials & Interfaces and is presently under revision: “Multifunctional Cellulose/Graphene/Fe₃O₄ Composite Aerogels for Electromagnetic Interference Shielding”. Co-authors: Petra Pötschke, Jürgen Pionteck, Brigitte Voit, and Haisong Qi.

4.3.1 Introduction

Over the past decade, high performance electromagnetic interference (EMI) shielding materials gained increasingly attention for application in civil and military fields, such as aircraft applications, communication equipment, and electronic equipment [188-191]. It is of increasing importance to fabricate high performance and unique EMI shielding materials to protect against electromagnetic radiation [192, 193]. Recently, many works have been carried out to develop light weight and high-performance EMI shielding materials using polymer composites mixed with conductive filler such as carbon nanofibers and CNTs [194-201]. As an ideal alternative to CNTs, graphene is widely studied as EMI shielding material, which is due to its electrical conductivity and the high aspect ratio. Moreover, many investigations have been carried out to introduce inorganic substances into graphene derivatives [202-206]. In addition to the separate performance of the graphene derivatives and of the inorganic fillers, the graphene derivatives modified by inorganic fillers can also exhibit a combined functionality [204, 207]. High-performance EMI shielding materials demand both conductive and magnetic components to improve impedance matching. Therefore, in addition to conductive graphene derivatives, such as reduced graphene oxide (rGO), magnetic fillers are also required to improve the EMI shielding effect (SE). Because of their outstanding properties, magnetic nanoparticles have been widely applied in electronic, biological, and environmental processes. Due to their low toxicity, good biocompatibility and wave absorbing properties, Fe₃O₄ nanoparticles are

frequently used today as EMI shielding materials. Synergistic effects between graphene and Fe_3O_4 nanoparticles are beneficial for the enhancement of the complex permeability of composite [208], and thereby for increasing the electromagnetic wave absorption ability [209-211]. Moreover, due to their high resistivity, the addition of Fe_3O_4 nanoparticles also can disrupt the interconnections of graphene and thus avoid the electromagnetic waves to enter the material easily, which could decrease the electrical conductivity and increase the EMI shielding ability [210]. Thus, the addition of Fe_3O_4 /graphene hybrids into a polymer matrix can result in high performance in EMI shielding materials.

In order to attain excellent and lightweight EMI shielding materials, an ideal candidate matrix is cellulose aerogel, which is a porous solid network. Cellulose, the most abundant and inexhaustible biopolymer in nature, have recently gained enormous attention due to its good chemical stability, non-toxicity, biodegradability, low-cost, biocompatibility, availability, renewability, and hydrophilicity. Due to its excellent properties, cellulose aerogel is very suitable for the preparation of EMI shielding aerogels. In the previous work of research (chapter 4.1 and 4.2), the in-situ reduction of GO to rGO and in-situ grow of Fe_3O_4 onto cellulose matrix was successfully achieved. In this work, we aimed to fabricate cellulose/rGO/ Fe_3O_4 aerogels for the application of EMI shielding fields by forming Fe_3O_4 in the cellulose/rGO composites.

4.3.2 Characterizations of cellulose/rGO/ Fe_3O_4 composites

Fig. 4.3.1 displays SEM and TEM images of different composites. SEM images (Fig. 4.3.1 (a-c)) show the morphologies of cellulose/rGO (5 wt.%)/ Fe_3O_4 film, cellulose/rGO (5 wt.%) aerogel, and cellulose/rGO (5 wt.%)/ Fe_3O_4 aerogel. Compared to the cellulose/rGO (5 wt.%)/ Fe_3O_4 film, the cellulose/rGO (5 wt.%) and cellulose/rGO (5 wt.%)/ Fe_3O_4 aerogels own open and highly porous structures with diameters of 300-500 nm. Fe_3O_4 nanoparticles locate densely and uniformly in the cell walls (Fig. 4.3.1 (d)). The TEM image of the cellulose/rGO (5 wt.%)/ Fe_3O_4 aerogel

reveals the formation of narrowly distributed Fe_3O_4 nanoparticles (with a mean diameter at about 12 nm, Fig. 4.3.2) located in the cellulose matrix, which forms the cell walls.

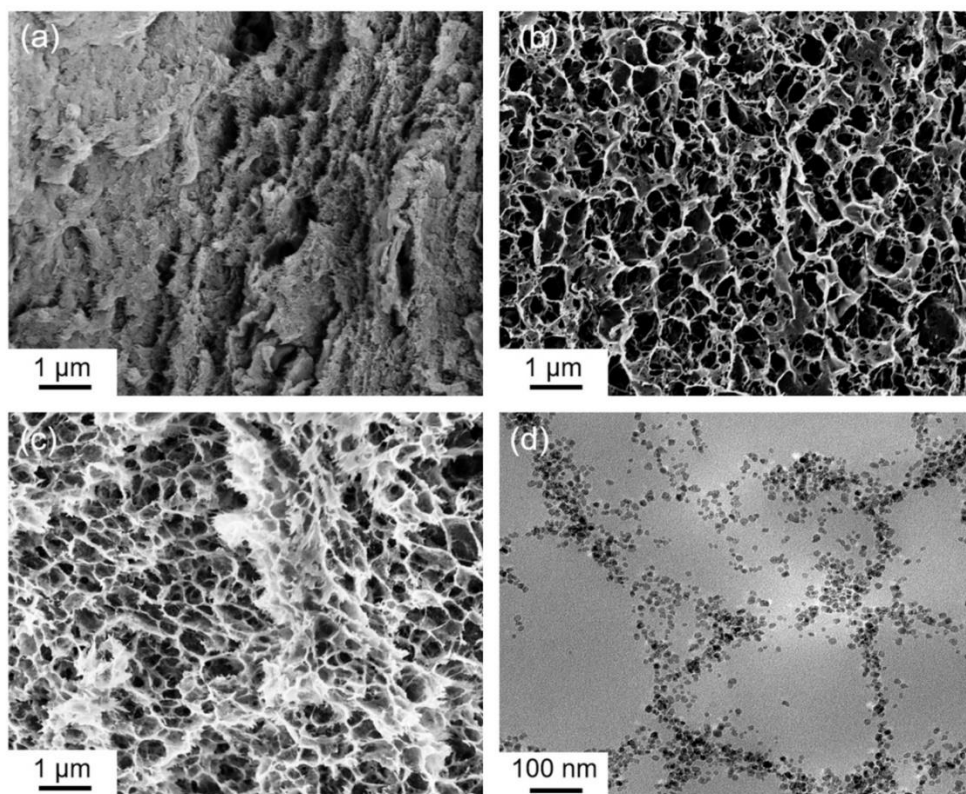


Fig. 4.3.1 Typical SEM images of different films and aerogels: (a) cellulose/rGO (5 wt.)/ Fe_3O_4 film; (b) cellulose/rGO (5 wt.%) aerogels; and (c) cellulose/rGO (5 wt.)/ Fe_3O_4 aerogel; (d) TEM image of cellulose/rGO (5 wt.)/ Fe_3O_4 composite aerogel.

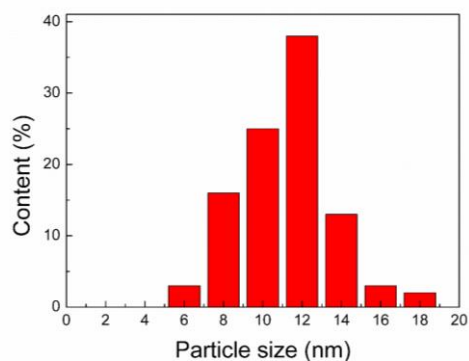


Fig.4.3.2 Size distributions of Fe_3O_4 nanoparticles in the cellulose/rGO (5 wt.)/ Fe_3O_4 aerogel.

The XRD diffractograms of the prepared composites are shown in Fig. 4.3.3 (a) to confirm the formation of Fe_3O_4 . The XRD diffraction peak of cellulose/rGO (5 wt.%)/ Fe_3O_4 composite at $2\theta = 30.3^\circ, 35.4^\circ, 43.3^\circ, 53.6^\circ, 57.2^\circ,$ and 62.9° correspond to (220), (311), (400), (422), (511), and (440) planes, respectively. All the peaks in cellulose/rGO (5 wt.%)/ Fe_3O_4 composite reveal the formation of Fe_3O_4 , as reported in the literature [174, 175]. Furthermore, the XRD diffraction peak at $21.9^\circ, 20.2^\circ,$ and 12.2° existed in both cellulose/rGO and cellulose/GO composites[63]. This result indicated their small size and their fine dispersion of fillers.

As is well known, Raman characterization is a convenient and powerful technique of testing the reduction of GO. Two fundamental vibrations can be observed in Raman spectra: D vibration band which is formed from a breathing mode of j-point photons of A_{1g} symmetry and G vibration band from first-order scattering of E_{2g} phonons by sp^2 carbon [212]. Raman spectrums of cellulose/GO, cellulose/rGO, and cellulose/rGO/ Fe_3O_4 composites are shown in Fig. 4.3.3 (b). The G-band shown in cellulose/rGO/ Fe_3O_4 and cellulose/rGO composites red-shifted from 1596 to 1579 and 1588 cm^{-1} , respectively, compared with cellulose/GO composite. This result can be attributed to the successfully in-situ reduction of GO to rGO and in-situ formation of Fe_3O_4 nanoparticles [213, 214]. The intensity ratio of D-band and G-band reflects the ratio of disordered sp^3 and ordered sp^2 carbon domains. The D/G intensity ratio of cellulose/rGO is around 1.54, while the result of cellulose/GO is around 1.01. This result contradicts the general expectation. During in-situ reduction, the D/G intensity ratio should decrease as the number of sp^3 defects decreases due to the reduction. However, the opposite effect has often been found in the literature [131, 132], and is explainable by the creation of small sp^2 domains with large fraction of graphene edges at lower GO reduction degrees. At higher reduction degrees, the small domains merge to larger ones with less edges and thus the D/G intensity will decrease, as expected. The wide scan XPS spectra of different composites are shown in Fig. 4.3.3 (c) to confirm the formation of Fe_3O_4 . The XPS spectrum of cellulose/rGO (5 wt.%)/ Fe_3O_4 displays

three characteristic peaks at 711, 530, and 285 eV, respect to Fe 2p, O 1s and, C 1s respectively. Moreover, the XPS spectrum of cellulose/rGO (5 wt.)/Fe₃O₄ displays two characteristic peaks at 724.7 and 711.2 eV, which is corresponding to Fe 2p_{1/2} and Fe 2p_{3/2}, respectively. These results agree with the case reported in the literature for Fe₃O₄ [173]. As shown in Fig. 4.3.3 (d), FTIR spectra of different composites also confirm the formation of Fe₃O₄ nanoparticles. Compared with the spectrum of cellulose/rGO (5 wt.%) and cellulose/GO (5 wt.%) composites, a new prominent band appeared at about 584 cm⁻¹ for cellulose/rGO (5 wt.)/Fe₃O₄ composites, which is due to the stretching mode of Fe-O.

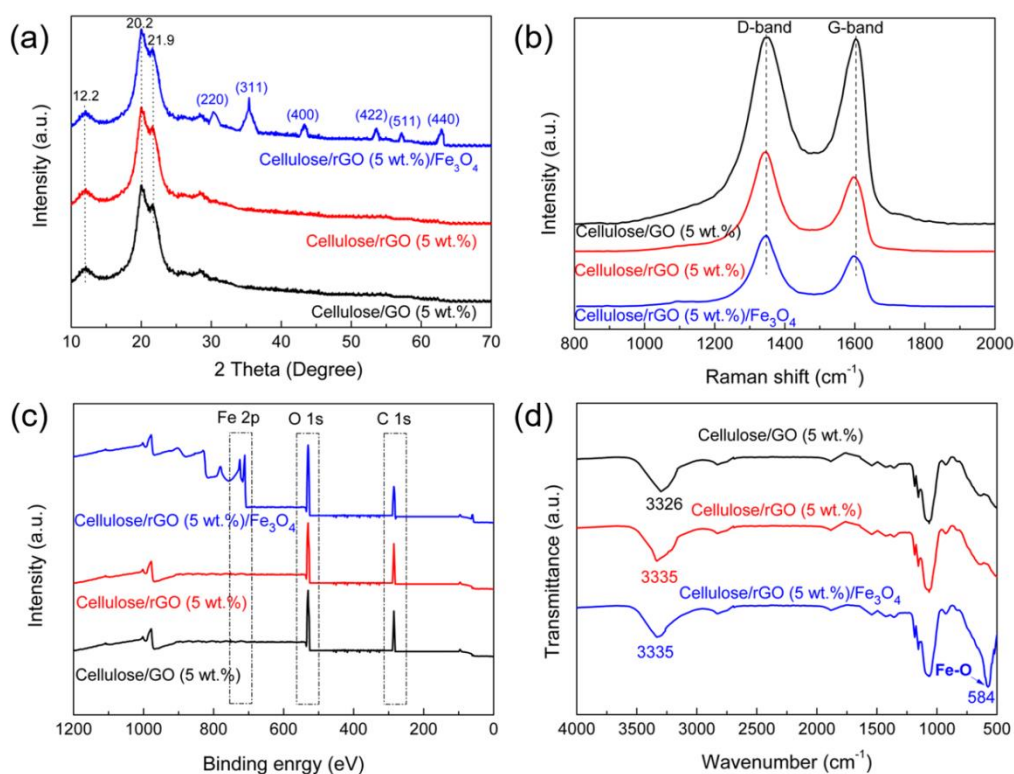


Fig. 4.3.3 (a) XRD pattern, (b) Raman spectra, (c) survey XPS spectra, and (d) FTIR spectra of cellulose/GO (5 wt.%), cellulose/rGO (5 wt.%), and cellulose/rGO (5 wt.)/Fe₃O₄.

Besides, the thermal stability of different composites with temperature from room temperature to 800 °C under nitrogen atmosphere is shown in Fig. 4.3.4 (a) to calculate the content of Fe₃O₄ nanoparticles. The residues after thermal degradation of different composites with and without Fe₃O₄ are recorded in Fig. 4.3.4 (b). The content of Fe₃O₄ in the different cellulose/rGO/Fe₃O₄ composite is about 15 wt.% and independent of the rGO content. The residues of the cellulose/rGO composites are also increasing with increasing rGO content, but a quantification overestimates the rGO content. Possibly, rGO stabilizes cellulose against degradation.

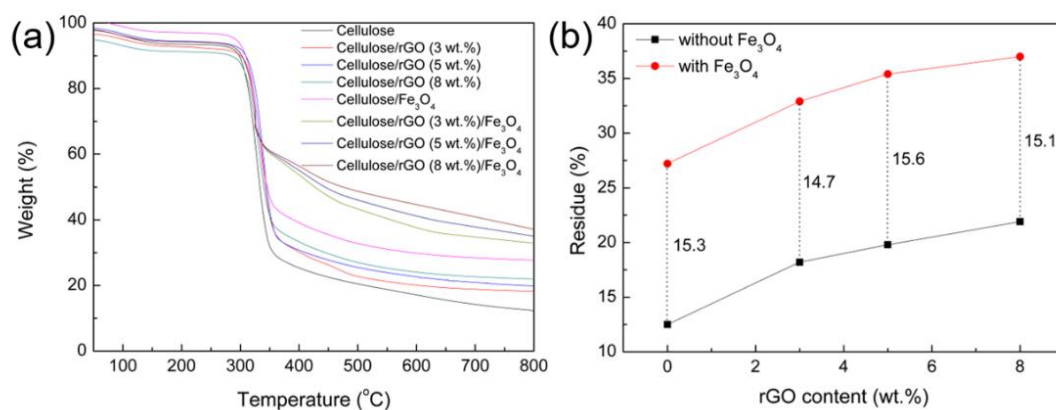


Fig. 4.3.4 (a) TGA curves of different composite films and cellulose. (b) Residues of cellulose/rGO and cellulose/rGO/Fe₃O₄ composite films.

4.3.3 Electrical conductivity of different samples

Fig. 4.3.5 shows electrical conductivity properties of cellulose/rGO/Fe₃O₄ and cellulose/rGO aerogels and films. While the composites without rGO are electrically insulating, the addition of 3 wt.% rGO increases the conductivity to the range of about 10^{-8} to 10^{-7} S/cm and 8 wt.% rGO addition to the range of 10^{-5} and 10^{-3} S/cm. The increase in film conductivity already at a content of 3 wt.% confirms a sufficiently good dispersion and suitable distribution of the rGO sheets in the cellulose matrix. Compared to cellulose/rGO composites, cellulose/rGO/Fe₃O₄ composites exhibit a small decrease

in conductivity at the same content of rGO. The intrinsically non-conductive Fe_3O_4 coated on the surface of rGO can weaken the formed rGO network and impede the transfer of electrons. Compared to cellulose/rGO and cellulose/rGO/ Fe_3O_4 films, the aerogels show a decrease in conductivity by more than one order of magnitude due to the presence of the microcellular structure in the aerogels. During drying at air, the film sample volume shrinks. Thus, the volume concentration of the dispersed particles increases reducing the particle distance. The homogeneous dispersed rGO narrow each other forming a dense, conductive network. In aerogels, the filler concentration in the solid phase is same as in films, but the only few 10 nm thick walls cause much stronger orientation of the rGO. The dimensions of the conductive paths through the volume of aerogel are changed and much longer and thinner compared to the film, thus reducing the conductivity.

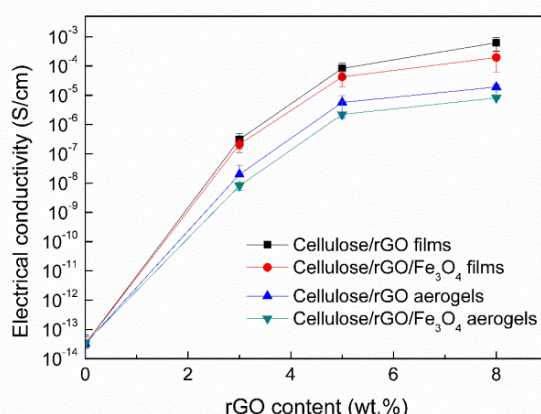


Fig. 4.3.5 Electrical conductivity with different rGO loadings for different cellulose composites.

4.3.4 Dielectric properties of different films and aerogels

Figure 5 shows the dielectric constant ϵ and its real (ϵ') and imaginary (ϵ'') part of cellulose/rGO and cellulose/rGO/ Fe_3O_4 films and aerogels ($\epsilon = \epsilon' + i \epsilon''$). The dielectric constant of different cellulose/rGO/ Fe_3O_4 composites decreases with

frequency. The frequency-dependent nature of the dielectric constant of conductive polymer composites is due to the dissipation of the charge at the polymer matrix/conductive filler interface into heat.[215, 216] For composite films and aerogels, increased rGO content enhanced the real and imaginary permittivity. This result is attributed to that higher rGO content tends to form more micro capacitors and subsequently results in higher dielectric constant. Moreover, the increased rGO content also increased both the cellulose-rGO interface area and interfacial polarization density.[217, 218] In the systems free of rGO only marginal differences between the film and aerogel can be seen, emphasizing the importance of the conductive filler on the permittivity. In presence of rGO, the microcellular structure of aerogels significantly improved the real and imaginary part of permittivity. rGO plates will be more oriented in the pore walls compared to their orientation in films. In combination with some agglomeration and the longer path lengths in aerogel walls, an increased number of micro capacitors will be formed, and increased interspace distance between the adjacent rGO plates leads to the higher dielectric constants of the composite aerogels.

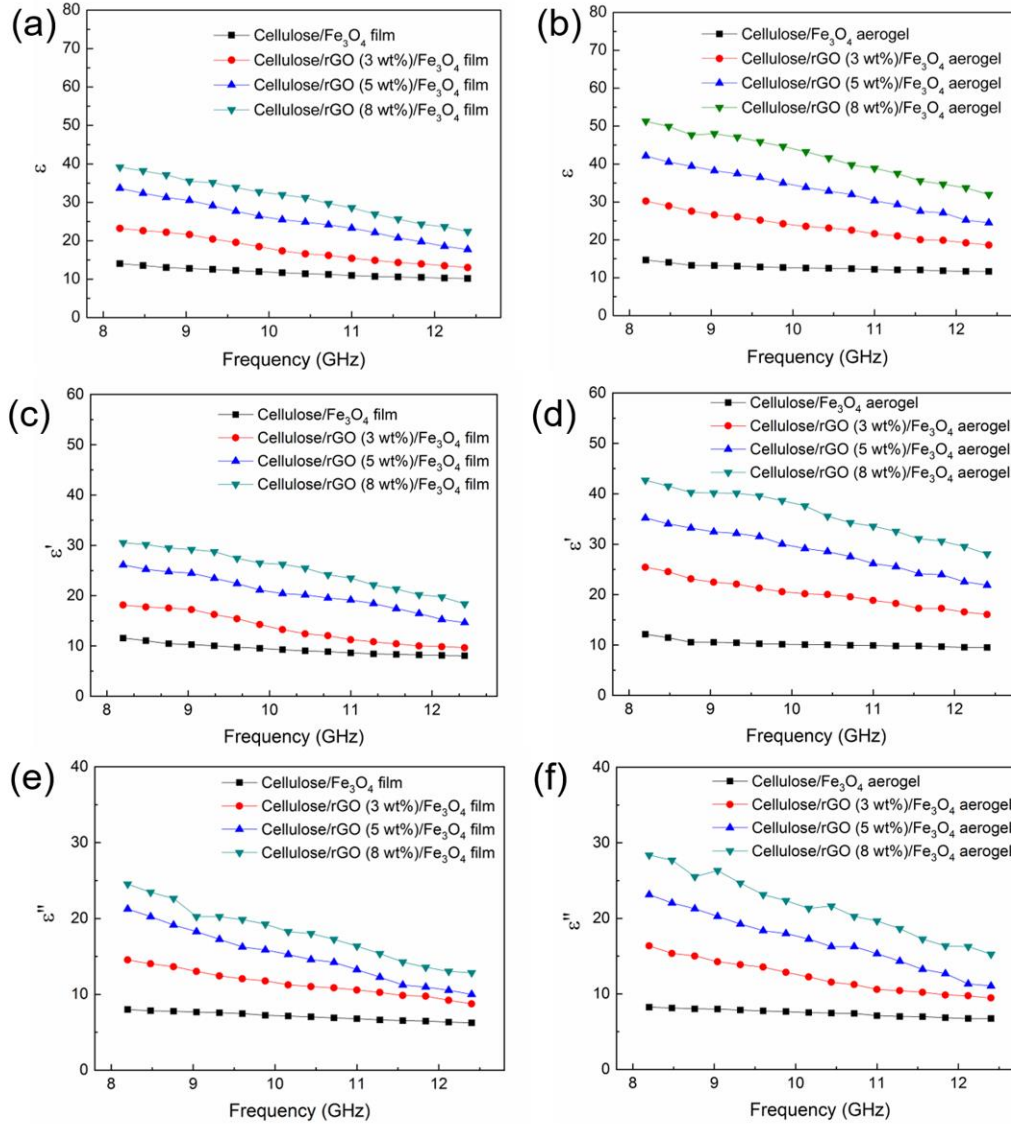


Fig.4.3.6 Dielectric constant ϵ and its real part ϵ' and imaginary part ϵ'' of different cellulose composite films and aerogels as a function of frequency.

4.3.5 Magnetic properties of different films and aerogels

The magnetic properties of cellulose/rGO/ Fe_3O_4 and cellulose/ Fe_3O_4 aerogels and films was measured at 300 K and in the range of -20000 to 20000 Oe. As shown in Fig. 4.3.7 (a) and (b), with increasing the rGO loading, the M_s (saturation magnetization) of cellulose/rGO/ Fe_3O_4 composite films and aerogels obviously decreased to the range of 2.2-4.0 emu/g. The M_s values of cellulose/rGO/ Fe_3O_4 composites are lower than those of cellulose/ Fe_3O_4 composites, which is corresponding with literature [208, 219, 220].

For cellulose/Fe₃O₄ and cellulose/rGO/Fe₃O₄ aerogels, the hysteresis loops show similar curves and values of M_s to those of the films, indicating that the microcellular structure has not significantly influenced the magnetic properties of samples. Cellulose/rGO/Fe₃O₄ films and aerogels were prepared from the same cellulose/rGO/Fe₃O₄ hydrogel, just by using different drying methods. The weight content and the size of Fe₃O₄ of the composite films and aerogels are the same. The distribution of Fe₃O₄ nanoparticles in the cellulose matrix in aerogels and films may be different due to the preparation methods. However, these changed distributions of the Fe₃O₄ nanoparticles are not strong enough to affect the magnetic properties. Interestingly, both the composite films and aerogels exhibit the property of superparamagnetism since there is no significant hysteresis in the M_s, as shown in Fig. 4.3.7. Fig. 4.3.8 is just part of Fig. 4.3.7 from -400 to 400 Oe to show coercivities of different composites clearly. The coercivities of cellulose/rGO/Fe₃O₄ composites as well as of cellulose/Fe₃O₄ were in the range of 30-40 Oe. This clearly proves that the superparamagnetism was not affected by the presence of rGO in the films or aerogels. Thus, the cellulose/rGO/Fe₃O₄ films and aerogels can be attracted in a magnetic field. Fig. 4.3.7 (insert) shows that the cellulose/rGO(5 wt. %)/Fe₃O₄ film and aerogel are attracted by a magnet.

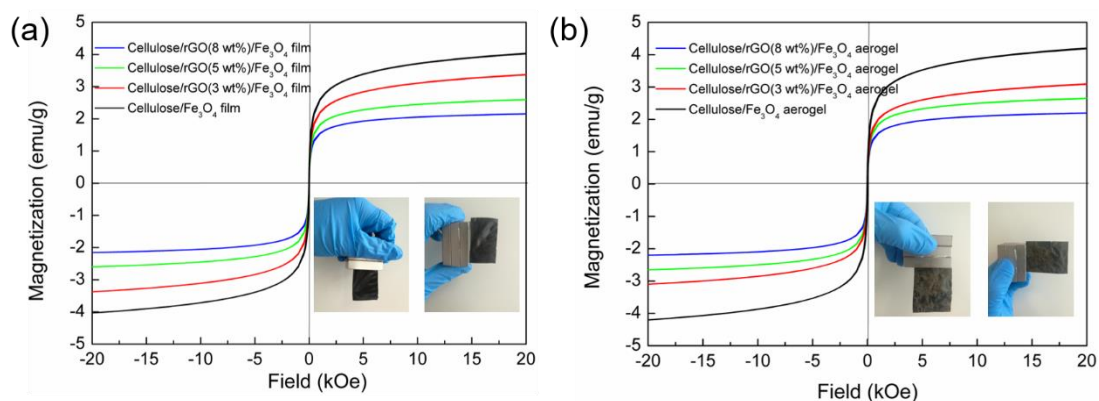


Fig. 4.3.7 Magnetization of cellulose/Fe₃O₄ and cellulose/rGO/Fe₃O₄ (a) films (about 0.04 mm thickness) and (b) aerogels (about 0.5 mm thickness). The inset show demonstrates the magnetic attraction of the samples.

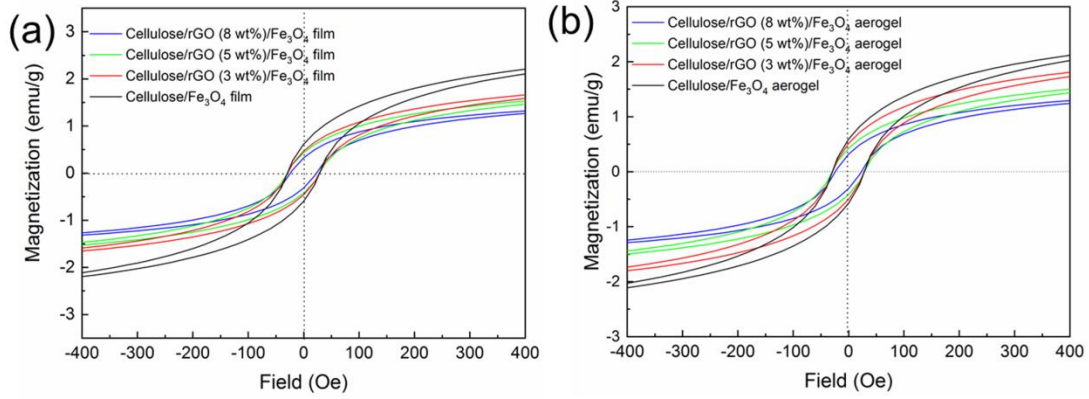


Fig. 4.3.8 Magnetization of cellulose/Fe₃O₄ and cellulose/rGO/Fe₃O₄ (a) films (about 0.04 mm thickness) and (b) aerogels (about 0.5 mm thickness) from -400 Oe to 400 Oe.

4.3.6 EMI shielding performance of different films and aerogels

The electromagnetic interference shielding efficiency (EMI SE) of cellulose/rGO/Fe₃O₄ aerogels and films with different thickness were tested in the 8.2-12.4 GHz range. This frequency range is used in various practical fields such as microwaves, medical electronic devices, signal transmission, and cell phones. It is well known that the total value of EMI SE (SE_{total}) is the sum of the reflection at the sample surface and backside (SE_R), the multiple internal reflection of microwaves (SE_M), and the absorption of electromagnetic energy (SE_A). The measured scattering parameters (S_{11} (reflection coefficient) and S_{12} (isolation)) were used to calculate reflectivity (R), absorptivity (A), and transmissivity (T) as follows: $R = S_{11}^2$, $T = S_{12}^2$, $A + R + T = 1$. SE_{total} , SE_R , and SE_A can be expressed by:

$$SE_{total} = -10 \log T \quad (4.3.1)$$

$$SE_R = -10 \log(1 - R) \quad (4.3.2)$$

$$SE_A = SE_{total} - SE_R - SE_M \quad (4.3.3)$$

The experimental setup did not allow to differentiate between SE_M and SE_A but SE_M may be negligible when the value of SE_A is higher than 10 dB. On the basis of shielding theory, SE is determined as follow:[221]

$$SE_{total}(dB) = 20d \left(\frac{\mu_r \omega \sigma}{2} \right)^{\frac{1}{2}} \log_{10}(e) + 10 \log_{10} \left(\frac{\sigma}{16 \mu_r \omega \epsilon_0} \right) \quad (4.3.4)$$

$$SE_A(dB) = 20d \left(\frac{\mu_r \omega \sigma}{2} \right)^{\frac{1}{2}} \log_{10}(e) \quad (4.3.5)$$

$$SE_R(dB) = 10 \log_{10} \left(\frac{\sigma}{16 \mu_r \omega \epsilon_0} \right) \quad (4.3.6)$$

where μ_r is real permeability of samples, σ is electrical conductivity of samples, d is thickness of samples, ω is angular frequency, e is the Euler's number (2.718), and ϵ_0 is dielectric constant of vacuum. According to the eq. (4.3.4) to (4.3.6), high electrical conductivity and high thickness of samples are beneficial for the EMI SE [222-224].

4.3.6.1 The influence of rGO contents

Fig. 4.3.9 illustrates the EMI SE of cellulose/rGO/Fe₃O₄ composite films and aerogels with different loading of rGO. All film thicknesses are constant and about 0.04 mm, and all aerogel thicknesses are constant and about 0.5 mm. As shown in Fig. 4.3.9 (a) and (b), all composite aerogels and films exhibited frequency dependencies EMI SE performance [225]. The SE_{total} of cellulose/Fe₃O₄ films, in the 8.2 -12.4 GHz frequency range, is 7.3-8.8 dB, for the corresponding aerogel it is 21.2-23.1 dB. The EMI shielding efficiency of both films and aerogels improve with rGO loading. For examples, the SE_{total} improves from 21.2-23.1 dB for the rGO free cellulose/Fe₃O₄ aerogels to 25.3-29.7 dB and even 32.4-40.1dB for cellulose/rGO (5 wt.%)/Fe₃O₄ and cellulose/rGO (8 wt.%)/Fe₃O₄ aerogels, respectively. This increase of SE_{total} driven by the introduction of rGO can be explained with the following mechanism: Firstly, the addition of rGO in the cellulose improves its electrical conductivity. As shown in Fig. 4.3.5, the electrical conductivity enhances with rGO loading from 8.9×10^{-13} S/cm in the cellulose/Fe₃O₄ aerogel to 6.9×10^{-6} S/cm and 1.2×10^{-5} S/cm in the cellulose/Fe₃O₄ aerogels with 5 or 8 wt.% rGO loading, respectively. This increase of electrical conductivity by increase of rGO loading weakens entered waves by the formation of a

conducting filler network [226-228], visible as an increase of the imaginary part of the permittivity (Fig. 4.3.6 (e) and (f)). Secondly, a larger number of micro capacitors may have been formed by rGO not participating in the conductive network or the changed dispersion of the Fe_3O_4 particles in presence of rGO enhances their absorbing efficiency, both increasing the real part of the permittivity (Fig. 4.3.6 (c) and (d)).

In all cases, the SE values of the aerogels are about twice as high as that of the corresponding films. The large surface area of the inner cell walls of the porous aerogels causes multiple-reflection at the inner surfaces of the aerogels and provide thus the high-efficient EMI shielding performance. The SE_{total} of cellulose/rGO (8 wt.%)/ Fe_3O_4 aerogel is 32.4-40.1dB which by far exceeds the requirements for the practical use of electromagnetic shielding materials, specified in the literature to be 20 dB [208]. This shows that our aerogel is very suitable for the practical application. Compared to other similar systems reported in literature, the SE_{total} value of cellulose/rGO (8 wt.%)/ Fe_3O_4 aerogel is obviously higher than those (13-19 dB) of graphene/polymethylmethacrylate (PMMA) composite aerogels reported by Zhang et al. [229] and those (18.7-22.5 dB) of CNTs/cellulose composite foams reported by Huang et al. [230].

SE_{total} , SE_{R} , and SE_{A} value of cellulose/rGO/ Fe_3O_4 composite films and aerogels at 10.2 GHz are summarized in Fig. 4.3.9 (c) and (d). All composite films and aerogels showed that the value of SE_{A} is much higher than SE_{R} , indicating that the absorption of microwaves is the dominant EMI shielding mechanism. For example, SE_{A} and SE_{R} value of cellulose/rGO (8 wt.%)/ Fe_3O_4 aerogel are 34.8 dB and 3.8 dB, respectively. All results display that the value of SE_{A} is higher than SE_{R} , demonstrating that the absorption of microwaves plays the major role in the EMI shielding mechanism of these cellulose composite films and aerogels.

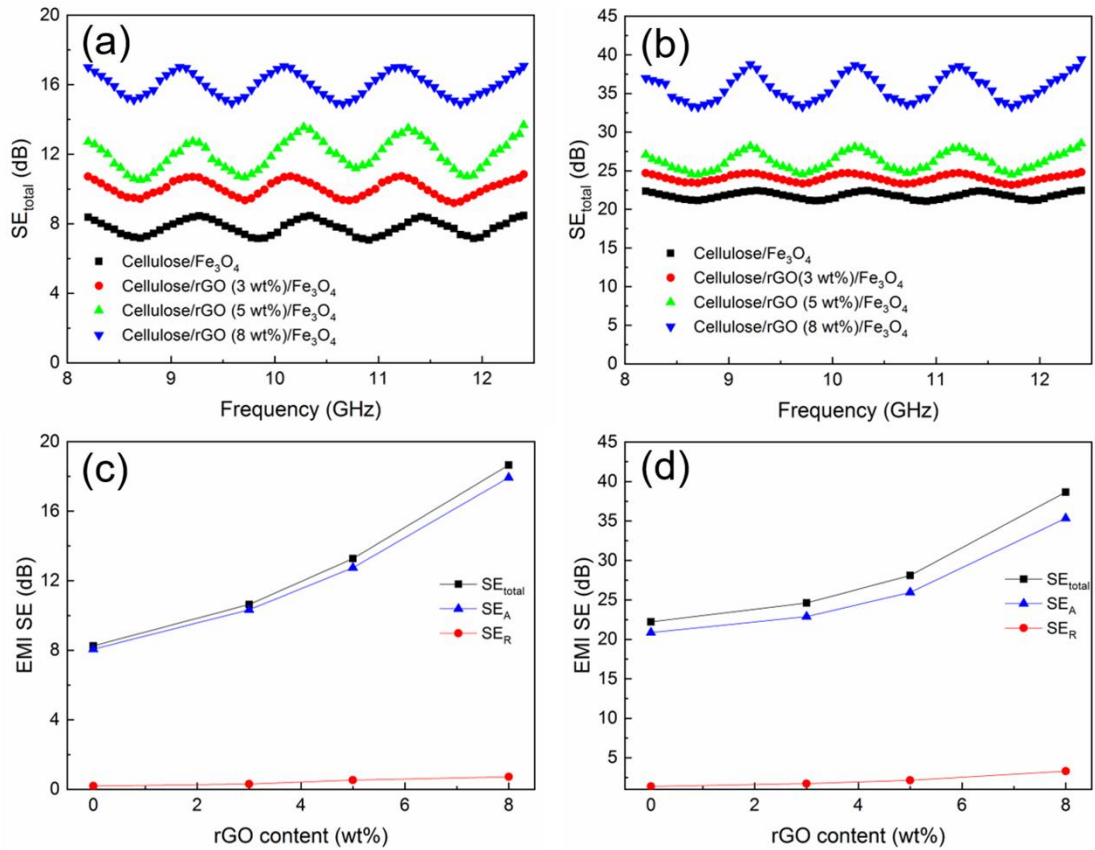


Fig. 4.3.9 EMI SE of cellulose/Fe₃O₄ and cellulose/rGO/Fe₃O₄ (a) films (about 0.04 mm thickness) and (b) aerogels (about 0.5 mm thickness). SE_{total}, SE_R, and SE_A at 10.2 GHz of cellulose/Fe₃O₄ and cellulose/rGO/Fe₃O₄ (c) films (about 0.04 mm thickness) and (d) aerogels (about 0.5 mm thickness) with various rGO concentrations.

4.3.6.2 The effect of sample thickness

The influence of thickness on the SE_{total} values of cellulose/rGO/Fe₃O₄ films is displayed in Fig. 4.3.10 (a). As demonstrated in eq. (4.3.4), the value of SE_{total} depends not only on the content of fillers, but also on the thickness of samples. Different thicknesses were realized by stacking of up to 4 specimens. With increasing of film thickness, SE_{total} values of cellulose/rGO/Fe₃O₄ composite films significantly increased. For example, SE_{total} value of cellulose/rGO (5 wt.%)/Fe₃O₄ film increased from 10.2-13.1 dB to 12.6-16.4 dB, 16.2-19.7 dB, and 17.4-22.4 dB, respectively. The influence of thickness on the SE_{total} values of cellulose/rGO/Fe₃O₄ aerogels is shown in Fig. 4.3.10 (b). Also the SE_{total} value of cellulose/rGO (5 wt.%)/Fe₃O₄ aerogel

improved from 24.8-29.1 dB to 31.6-34.4 dB, 40.2-43.7 dB, and 49.4-52.4 dB, respectively. With increasing film and aerogel thickness, the interior surface area increases, leading to the attenuation of the entered microwaves. The increasing amount of Fe_3O_4 nanoparticles and rGO plates with increased film thickness gives more opportunities for interference of the incoming electromagnetic waves with the filler particles, and also waves penetrating deeper in the material can be attenuated. The multiple-reflection effect at the inner surfaces of the cell walls contributes to the high-efficient EMI shielding performance of the aerogels.

SE_{total} , SE_{R} , and SE_{A} values of cellulose/rGO (5 wt.%)/ Fe_3O_4 films and aerogels with different sample thicknesses at 10.2 GHz are summarized in Fig. 4.3.10 (c) and (d). As shown in Fig. 4.3.10 (c), the SE_{A} value of cellulose/rGO (5 wt.%)/ Fe_3O_4 films improved from 12.6 dB to 14.1dB, 17.3 dB, and 21.2 dB, respectively, while SE_{R} value of cellulose/rGO (5 wt.%)/ Fe_3O_4 films remained nearly constant at around 0.6 dB. Based on eq. (4.3.5) and (4.3.6), the thickness of the sample affects the SE_{A} whereas SE_{R} is hardly affected by the thickness. Fig. 4.3.10 (d) shows the relationship between the sample thickness and the SE_{A} values for cellulose/rGO (5 wt.%)/ Fe_3O_4 composite aerogels. With increasing sample thickness, SE_{A} of cellulose/rGO (5 wt.%)/ Fe_3O_4 composite aerogels increase from 25.2 dB to 30.1 dB, 38.7 dB and, 41.8 dB, while SE_{R} is around 2.6 dB with a just slight tendency to increase with sample thickness. In films as well as in aerogels the dependency of SE_{A} is not linear. Possibly most of the waves penetrating into the material attenuate already near the surface and the added thickness contributes less to the shielding.

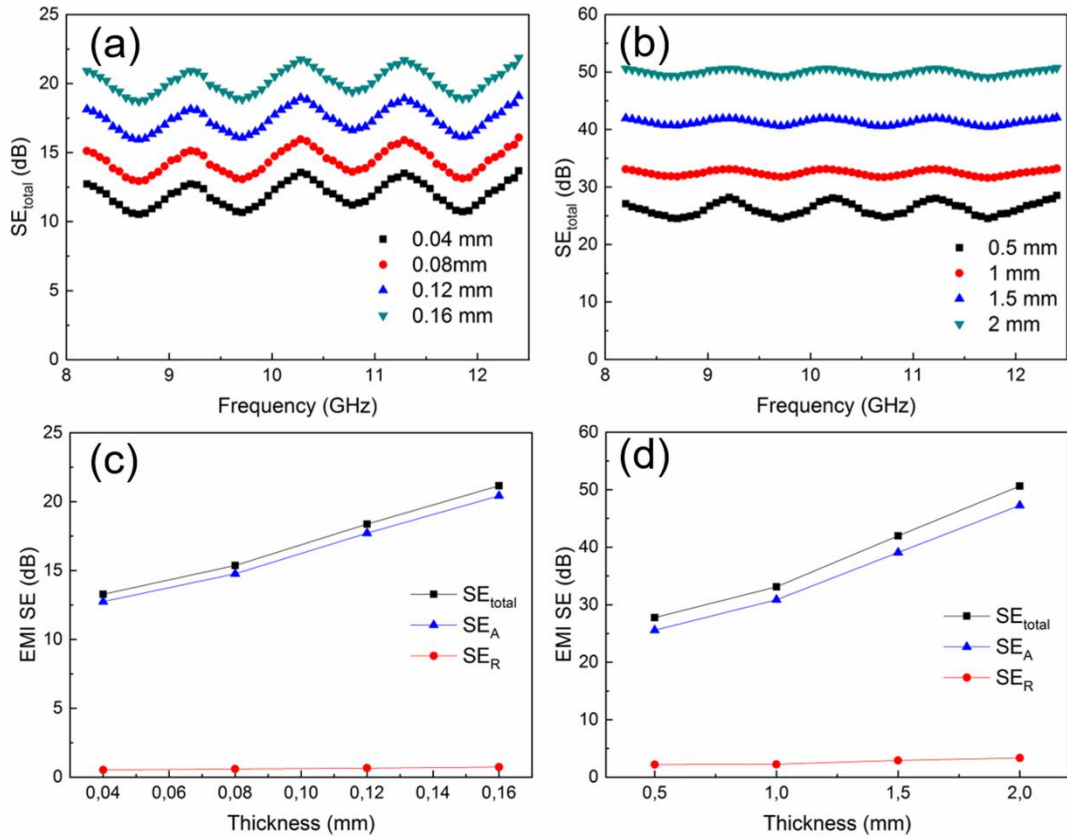


Fig. 4.3.10 Thicknesses dependence of the EMI SE of (a) cellulose/rGO (5 wt.)/Fe₃O₄ films and (b) cellulose/rGO (5 wt.)/Fe₃O₄ aerogels in the 8.2-12.4 GHz frequency range. SE_{total}, SE_R, and SE_A with various thicknesses for (c) cellulose/rGO (5 wt.)/Fe₃O₄ films and (d) cellulose/rGO (5 wt.)/Fe₃O₄ aerogels at 10.2 GHz.

4.3.7 The possible EMI shielding mechanism

The EMI shielding mechanism of our cellulose/rGO/Fe₃O₄ aerogels is schematically illustrated in Fig. 4.3.11. The electromagnetic microwave behaviour across the cellulose/rGO/Fe₃O₄ aerogel is sketched in Fig. 4.3.11 (a). On the one hand, the porous structure of cellulose/rGO/Fe₃O₄ aerogel (Fig. 4.3.11 (c)) exhibit large interfacial area between the cell walls and the pores in the aerogel. The electromagnetic waves entering the aerogel will reflect and scatter repeatedly at the surfaces of the cell walls, and thus they are trapped in the cellulose/rGO/Fe₃O₄ aerogel where they will

attenuate (Fig. 4.3.11 (b)). Additionally, as depicted in Fig. 4.3.11 (e), the entered microwaves will scatter and reflect several times at parallel oriented rGO sheets with large aspect ratio, which further contributes to the wave attenuation. On the other hand, impedance matching is another important wave absorbing mechanism. The introduction of Fe_3O_4 nanoparticles (Fig. 4.3.11 (d)) lowers the electrical conductivity of the aerogel, and improves the values of the electromagnetic parameters, which helps to improve the level of impedance matching and thus the wave absorption in the cellulose/rGO/ Fe_3O_4 aerogel. Concludingly, the multireflection of microwaves and impedance matching bring about the high-efficiency EMI shielding performance of aerogels caused by their porous structure and the presence of rGO sheets and Fe_3O_4 nanoparticles. The absorption plays the major role in the EMI shielding mechanism for cellulose/rGO/ Fe_3O_4 aerogels and in films. In summary, these cellulose/rGO/ Fe_3O_4 aerogels are ideal candidates for efficient and lightweight EMI shielding applications.

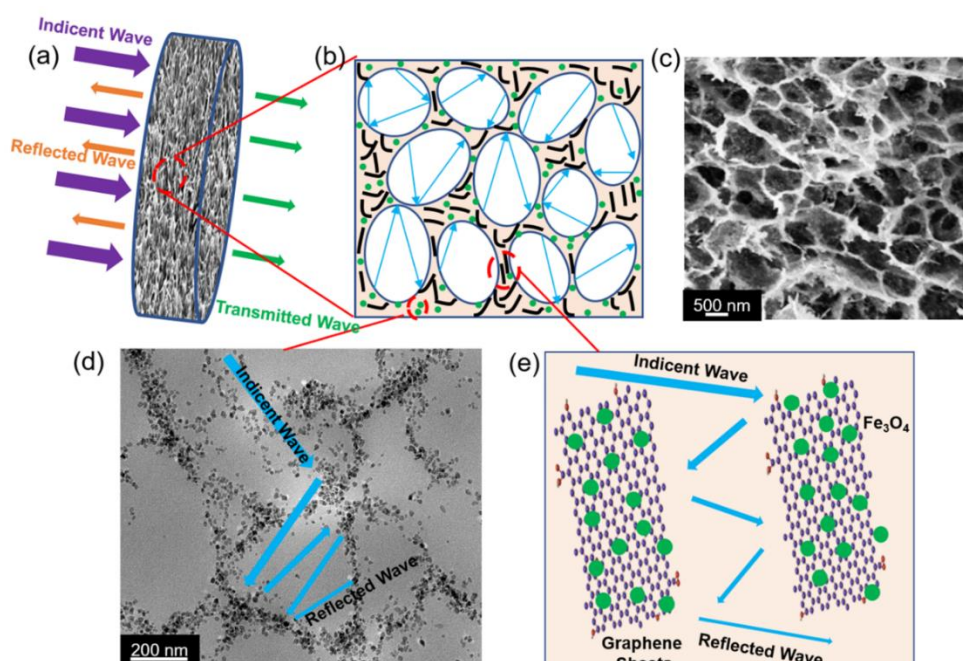


Fig. 4.3.11 (a) and (b) Schematic image of the EMI shielding mechanism of a cellulose/rGO/ Fe_3O_4 aerogel; (c) SEM image of cellulose/rGO (5 wt.)/ Fe_3O_4 aerogel; (d)

TEM image of cellulose/rGO (5 wt.)/Fe₃O₄ aerogel with sketched microwave absorption mechanism at Fe₃O₄ nanoparticles; (e) multiple reflection and absorption mechanism at two parallel rGO/Fe₃O₄ sheets.

4.3.7 Summary

Cellulose/rGO/Fe₃O₄ films and aerogels were successfully fabricated by the in-situ preparation of Fe₃O₄ nanoparticles in a cellulose solution containing rGO, which is a simple, efficient and environmentally friendly method. Films were obtained by drying while freeze-drying resulted in the formation of aerogels. Aerogels are much more effective for EMI shielding application than the same weight of the corresponding film due to the high amount of inner interface between the pores and the cell walls, which cause multiple electromagnetic wave scattering and reflection. Cellulose/rGO (8 wt.)/Fe₃O₄ aerogels with the thickness of 0.5 mm exhibit high EMI shielding performance with an EMI SE of 32.4-40.1 dB in the 8.2-12.4 GHz frequency range. High loadings with rGO and large thicknesses of the composites are beneficial for the EMI shielding performance of films and aerogels.

The absorption plays the major role in the EMI shielding mechanism for both cellulose/rGO/Fe₃O₄ films and aerogels. In the aerogels, the combined effect of multireflection of microwaves at the pore surfaces and the impedance matching due to the presence of Fe₃O₄ nanoparticles in the Cellulose/rGO composite brings about their high-efficient EMI shielding performance. The lightweight aerogels are suitable for the practical EMI shielding applications e.g. in spacecraft, aircraft, energy conversion application, and energy storage.

5. Summary

This thesis focused on the synthesis and characterization of novel functional materials based on cellulose and graphene derivatives. Cellulose/GO hydrogels were produced as the starting material by dissolving cellulose and dispersing GO in NaOH/urea solution. This method is considered as an efficient, simple, environmentally friendly, and low-cost method. Novel functionalities, such as sensing, catalytic and EMI shielding properties have been “built-in” to cellulose/GO hydrogels.

The thesis is summarized from three chapters. In the first chapter, cellulose/rGO composite films and aerogels were successfully fabricated by dissolving cellulose and dispersing GO in NaOH/urea solution, followed by the chemical reduction with vitamin C as the reducing agent. The cellulose/rGO films and aerogels with various rGO contents were prepared by air-drying and freeze-drying of the prepared cellulose/rGO composite hydrogels. The resultant cellulose/rGO composites prepared by this efficient and simple method show high resistance sensitivity to environmental stimuli like temperature, humidity, liquids, vapours, and strain stress. Thus, the cellulose/rGO films can be applied in detecting human motions and human breath cycles. Liquid temperature, liquid type, and ion concentration also can be determined by our cellulose/rGO films. Moreover, the composite aerogels are fast responding and extremely sensitive sensors for vapour detection and testing with good repeatability. It was also revealed that discriminating and quantitative responses can be obtained when analyzing various vapours and different vapour concentrations. For methanol vapour, the aerogel shows linear response to the vapour concentration. Thus cellulose/rGO composite aerogel can be used to quantify methanol vapour concentrations. The efficient, scalable, and environmentally friendly preparation of novel and high-performance vapour sensing materials with well reproducibility is promising to achieve practical vapour sensing applications.

In second chapter, the thesis has successfully presented an effective, facial, simple, and scalable method to form Fe₃O₄ nanoparticles onto cellulose/GO hydrogels. XRD, FTIR, XPS and TEM indicated that Fe₃O₄ nanoparticles with good dispersion and uniform size are successfully coated on cellulose matrix and GO sheets. This material was tested as catalyst for the cleaning of dye-contaminated water by oxidation with H₂O₂. The optimized experiment conditions for AO7 degradation are: [AO7] = 0.1 mM, T = 298 K, [H₂O₂] = 22 mM, and pH = 3. Under these conditions, the resulting hydrogels display 97 % AO7 removal within 120 min and retained strong degradation performance after twenty consecutive cycles of reuse. Especially, the detailed XPS analysis of cellulose/GO/Fe₃O₄ and cellulose/Fe₃O₄ composites indicated that the cellulose/GO/Fe₃O₄ hydrogel retain its high degradation activity by keeping the ratio of Fe³⁺/Fe²⁺ at 2 during the 20 heterogeneous Fenton-like reaction cycles. Therefore, the cellulose/GO/Fe₃O₄ hydrogel is recommended to test the treatment of other dye-contaminated wastewaters.

In the third chapter, cellulose/rGO/Fe₃O₄ films and aerogels were successfully fabricated by the in-situ grown of Fe₃O₄ nanoparticles within a cellulose matrix containing rGO sheets. Thus, materials useful for the EMI shielding applications were obtained through a simple, efficient, and environmentally friendly method. Cellulose/rGO (8 wt.%)/Fe₃O₄ aerogels with the thickness of 0.5 mm exhibited high EMI shielding performance with the EMI SE value at 32.4-40.1 dB in the 8.2-12.4 GHz frequency range (X-band). High loading of rGO and large thickness of the composites are beneficial for the excellent EMI shielding performance of our aerogels. The lightweight aerogel is suitable for the practical application as EMI shielding materials such as spacecraft, aircraft, energy conversion application, and energy storage.

6. Outlook

This research has exhibited the potential applications of functional and smart materials based on cellulose and graphene derivatives as multifunctional sensors, for wastewater treatment, and EMI shielding. However, some other works also should be perfected in the future.

In the first chapter, the cellulose/rGO films used as strain sensors can distinguish between different human hand motions by different shapes of the responsive curves and maximum R_{rel} , when the film was attached on the back of hand and finger. Moreover, other human motions such as knee flexion, elbow flexion, and facial movement are also worth to detect. The cellulose/rGO films as liquid sensors can distinguish different NaCl contents in water by the maximum R_{rel} . It is also interesting to explore different salt types with same content in water.

In the second chapter, apart from AO7 dye, there are also many other dyes in wastewaters which are difficult to degrade. The degradation mechanism for Fenton or Fenton-like reactions is similar. Therefore, there is a window of opportunity to explore the catalytic performance of cellulose/GO/Fe₃O₄ hydrogels for the degradation of other dyes. Furthermore, the influence of Fe₃O₄ content on removal of AO7 is also worth to be studied. In this work, the content of Fe₃O₄ in cellulose/GO/Fe₃O₄ hydrogels is controlled at around 12 wt.%. Different contents of Fe₃O₄ can be obtained by changing the content of FeCl₃ and FeCl₂ and the immersion time during the preparation process.

In the third chapter, the EMI shielding performance of cellulose/rGO and cellulose/rGO/Fe₃O₄ aerogels are compared. Furthermore, the influence of Fe₃O₄ content on the EMI shielding performance is worth to be investigated.

Finally, by introducing titanium dioxide or other functional materials into cellulose/GO hydrogels, photo-catalytic activity of the composites may be reached,

useful in effective photocatalytic degradation and physical adsorption materials. By adding fluorescent compounds or other functional materials into cellulose/GO hydrogels, fluorescent cellulose films or hydrogels can be fabricated for the photo-functional application. In a word, cellulose/GO hydrogels as starting materials have great potential for simple, effective, environmentally friendly, and low-cost preparation of functional materials for various applications.

Bibliography

1. Gavillon, R. and T. Budtova, *Aerocellulose: new highly porous cellulose prepared from cellulose-NaOH aqueous solutions*. *Biomacromolecules*, 2007. **9**(1): p. 269-277.
2. Yang, Q., et al., *Transparent cellulose films with high gas barrier properties fabricated from aqueous alkali/urea solutions*. *Biomacromolecules*, 2011. **12**(7): p. 2766-2771.
3. Qi, H., et al., *Multifunctional films composed of carbon nanotubes and cellulose regenerated from alkaline-urea solution*. *Journal of Materials Chemistry A*, 2013. **1**(6): p. 2161-2168.
4. Isogai, A. and R. Atalla, *Dissolution of cellulose in aqueous NaOH solutions*. *Cellulose*, 1998. **5**(4): p. 309-319.
5. Fink, H.-P., et al., *Structure formation of regenerated cellulose materials from NMMO-solutions*. *Progress in Polymer Science*, 2001. **26**(9): p. 1473-1524.
6. Zhu, S., et al., *Dissolution of cellulose with ionic liquids and its application: a mini-review*. *Green Chemistry*, 2006. **8**(4): p. 325-327.
7. Swatloski, R.P., et al., *Dissolution of cellose with ionic liquids*. *Journal of the American Chemical Society*, 2002. **124**(18): p. 4974-4975.
8. Kosan, B., C. Michels, and F. Meister, *Dissolution and forming of cellulose with ionic liquids*. *Cellulose*, 2008. **15**(1): p. 59-66.
9. McCormick, C.L., P.A. Callais, and B.H. Hutchinson Jr, *Solution studies of cellulose in lithium chloride and N, N-dimethylacetamide*. *Macromolecules*, 1985. **18**(12): p. 2394-2401.
10. Striegel, A., *Theory and applications of DMAc/LiCl in the analysis of polysaccharides*. *Carbohydrate polymers*, 1997. **34**(4): p. 267-274.

11. Faruk, O., et al., *Biocomposites reinforced with natural fibers: 2000-2010*. Progress in polymer science, 2012. **37**(11): p. 1552-1596.
12. Kim, J., S. Yun, and Z. Ounaies, *Discovery of cellulose as a smart material*. Macromolecules, 2006. **39**(12): p. 4202-4206.
13. Shi, Z., G.O. Phillips, and G. Yang, *Nanocellulose electroconductive composites*. Nanoscale, 2013. **5**(8): p. 3194-3201.
14. Thiemann, S., et al., *Cellulose-Based Ionogels for Paper Electronics*. Advanced Functional Materials, 2014. **24**(5): p. 625-634.
15. Moon, R.J., et al., *Cellulose nanomaterials review: structure, properties and nanocomposites*. Chemical Society Reviews, 2011. **40**(7): p. 3941-3994.
16. Klemm, D., et al., *Cellulose: fascinating biopolymer and sustainable raw material*. Angewandte Chemie International Edition, 2005. **44**(22): p. 3358-3393.
17. Habibi, Y., L.A. Lucia, and O.J. Rojas, *Cellulose nanocrystals: chemistry, self-assembly, and applications*. Chemical Reviews, 2010. **110**(6): p. 3479-3500.
18. Hu, L., et al., *Highly conductive paper for energy-storage devices*. Proceedings of the National Academy of Sciences, 2009. **106**(51): p. 21490-21494.
19. Peng, C., Y. Thio, and R. Gerhardt, *Conductive paper fabricated by layer-by-layer assembly of polyelectrolytes and ITO nanoparticles*. Nanotechnology, 2008. **19**(50): p. 505603.
20. Pushparaj, V.L., et al., *Flexible energy storage devices based on nanocomposite paper*. Proceedings of the National Academy of Sciences, 2007. **104**(34): p. 13574-13577.

21. Tai, Y.-L. and Z.-G. Yang, *Fabrication of paper-based conductive patterns for flexible electronics by direct-writing*. Journal of Materials Chemistry, 2011. **21**(16): p. 5938-5943.
22. Russo, A., et al., *Pen-on-paper flexible electronics*. Advanced Materials, 2011. **23**(30): p. 3426-3430.
23. Hu, L., et al., *Transparent and conductive paper from nanocellulose fibers*. Energy & Environmental Science, 2013. **6**(2): p. 513-518.
24. Weng, Z., et al., *Graphene-cellulose paper flexible supercapacitors*. Advanced Energy Materials, 2011. **1**(5): p. 917-922.
25. Zheng, G., et al., *Nanostructured paper for flexible energy and electronic devices*. MRS Bulletin, 2013. **38**(04): p. 320-325.
26. Terzopoulou, Z., G.Z. Kyzas, and D.N. Bikiaris, *Recent advances in nanocomposite materials of graphene derivatives with polysaccharides*. Materials, 2015. **8**(2): p. 652-683.
27. Dikin, D.A., et al., *Preparation and characterization of graphene oxide paper*. Nature, 2007. **448**(7152): p. 457-460.
28. Li, D. and R.B. Kaner, *Graphene-based materials*. Nat Nanotechnol, 2008. **3**: p. 101.
29. Bunch, J.S., et al., *Electromechanical resonators from graphene sheets*. Science, 2007. **315**(5811): p. 490-493.
30. Geim, A.K. and K.S. Novoselov, *The rise of graphene*. Nature Materials, 2007. **6**(3): p. 183-191.
31. Liu, Z., et al., *Organic photovoltaic devices based on a novel acceptor material: graphene*. Advanced Materials, 2008. **20**(20): p. 3924-3930.
32. Si, Y. and E.T. Samulski, *Synthesis of water soluble graphene*. Nano Letters, 2008. **8**(6): p. 1679-1682.

33. Stankovich, S., et al., *Synthesis and exfoliation of isocyanate-treated graphene oxide nanoplatelets*. Carbon, 2006. **44**(15): p. 3342-3347.
34. Stankovich, S., et al., *Graphene-based composite materials*. nature, 2006. **442**(7100): p. 282-286.
35. Niyogi, S., et al., *Solution properties of graphite and graphene*. Journal of the American Chemical Society, 2006. **128**(24): p. 7720-7721.
36. Xu, Y., et al., *Flexible graphene films via the filtration of water-soluble noncovalent functionalized graphene sheets*. Journal of the American Chemical Society, 2008. **130**(18): p. 5856-5857.
37. Kim, K.S., et al., *Large-scale pattern growth of graphene films for stretchable transparent electrodes*. Nature, 2009. **457**(7230): p. 706-710.
38. Mao, S., H. Pu, and J. Chen, *Graphene oxide and its reduction: modeling and experimental progress*. RSC Advances, 2012. **2**(7): p. 2643-2662.
39. Reina, A., et al., *Large area, few-layer graphene films on arbitrary substrates by chemical vapor deposition*. Nano Letters, 2008. **9**(1): p. 30-35.
40. Sutter, P.W., J.-I. Flege, and E.A. Sutter, *Epitaxial graphene on ruthenium*. Nature Materials, 2008. **7**(5): p. 406-411.
41. Kim, C.-J., et al., *Graphene oxide/cellulose composite using NMMO monohydrate*. Carbohydrate polymers, 2011. **86**(2): p. 903-909.
42. Valentini, L., et al., *A novel method to prepare conductive nanocrystalline cellulose/graphene oxide composite films*. Materials Letters, 2013. **105**: p. 4-7.
43. You, F., et al., *In situ thermal reduction of graphene oxide in a styrene-ethylene/butylene-styrene triblock copolymer via melt blending*. Polymer International, 2014. **63**(1): p. 93-99.
44. Gao, W., et al., *New insights into the structure and reduction of graphite oxide*. Nature Chemistry, 2009. **1**(5): p. 403-408.

45. Dreyer, D.R., et al., *The chemistry of graphene oxide*. Chemical Society Reviews, 2010. **39**(1): p. 228-240.
46. Pei, S. and H.-M. Cheng, *The reduction of graphene oxide*. Carbon, 2012. **50**(9): p. 3210-3228.
47. Wilkes, J.S., *A short history of ionic liquids-from molten salts to neoteric solvents*. Green Chemistry, 2002. **4**(2): p. 73-80.
48. Feng, L. and Z.-l. Chen, *Research progress on dissolution and functional modification of cellulose in ionic liquids*. Journal of Molecular Liquids, 2008. **142**(1): p. 1-5.
49. Li, D., et al., *Processable aqueous dispersions of graphene nanosheets*. Nature Nanotechnology, 2008. **3**(2): p. 101-105.
50. Hu, K., et al., *Graphene-polymer nanocomposites for structural and functional applications*. Progress in Polymer Science, 2014. **39**(11): p. 1934-1972.
51. Titelman, G., et al., *Characteristics and microstructure of aqueous colloidal dispersions of graphite oxide*. Carbon, 2005. **43**(3): p. 641-649.
52. Kim, H., A.A. Abdala, and C.W. Macosko, *Graphene/polymer nanocomposites*. Macromolecules, 2010. **43**(16): p. 6515-6530.
53. Peng, H., et al., *Simultaneous reduction and surface functionalization of graphene oxide by natural cellulose with the assistance of the ionic liquid*. The Journal of Physical Chemistry C, 2012. **116**(30): p. 16294-16299.
54. Zhang, T., et al., *Effect of cellulose solubility on the thermal and mechanical properties of regenerated cellulose/graphene nanocomposites based on ionic liquid 1-allyl-3-methylimidazolium chloride*. RSC Advances, 2015. **5**(93): p. 76302-76308.
55. Tariq, M., et al., *Surface tension of ionic liquids and ionic liquid solutions*. Chemical Society Reviews, 2012. **41**(2): p. 829-868.

56. Crowhurst, L., et al., *Solvent-solute interactions in ionic liquids*. Physical Chemistry Chemical Physics, 2003. **5**(13): p. 2790-2794.
57. Petkovic, M., et al., *Ionic liquids: a pathway to environmental acceptability*. Chemical Society Reviews, 2011. **40**(3): p. 1383-1403.
58. Battista, O. and P. Smith, *Microcrystalline cellulose*. Industrial & Engineering Chemistry, 1962. **54**(9): p. 20-29.
59. Ye, W., et al., *Green fabrication of cellulose/graphene composite in ionic liquid and its electrochemical and photothermal properties*. Chemical Engineering Journal, 2016. **299**: p. 45-55.
60. Wang, H., G. Gurau, and R.D. Rogers, *Ionic liquid processing of cellulose*. Chemical Society Reviews, 2012. **41**(4): p. 1519-1537.
61. Cai, J., et al., *Dynamic self-assembly induced rapid dissolution of cellulose at low temperatures*. Macromolecules, 2008. **41**(23): p. 9345-9351.
62. Cai, J. and L. Zhang, *Rapid dissolution of cellulose in LiOH/urea and NaOH/urea aqueous solutions*. Macromolecular Bioscience, 2005. **5**(6): p. 539-548.
63. Qi, H., C. Chang, and L. Zhang, *Properties and applications of biodegradable transparent and photoluminescent cellulose films prepared via a green process*. Green Chemistry, 2009. **11**(2): p. 177-184.
64. Ruan, D., et al., *Structure and properties of novel fibers spun from cellulose in NaOH/thiourea aqueous solution*. Macromolecular Bioscience, 2004. **4**(12): p. 1105-1112.
65. Qi, H., et al., *The dissolution of cellulose in NaOH-based aqueous system by two-step process*. Cellulose, 2011. **18**(2): p. 237-245.
66. Huang, H.-D., et al., *Ultra-low gas permeability and efficient reinforcement of cellulose nanocomposite films by well-aligned graphene oxide nanosheets*. Journal of Materials Chemistry A, 2014. **2**(38): p. 15853-15863.

67. Wu, Y., et al., *Clarification of go acted as a barrier against the crack propagation of the cellulose composite films*. Composites Science and Technology, 2014. **104**: p. 52-58.
68. Graenacher, C. and R. Sallmann, *Cellulose solutions and process of making same*, 1939, Google Patents.
69. Johnson, D.L., *Compounds dissolved in cyclic amine oxides*, 1969, Google Patents.
70. Li, H.-J., et al., *Development and characterization of anti-fouling cellulose hollow fiber UF membranes for oil-water separation*. Journal of Membrane Science, 2006. **279**(1): p. 328-335.
71. Zhou, S., et al., *Preparation of cellulose-graphene oxide aerogels with N-methyl morpholine-N-oxide as a solvent*. Journal of Applied Polymer Science, 2018. **135**(15): p. 46152.
72. Heinze, T. and T. Liebert, *Unconventional methods in cellulose functionalization*. Progress in Polymer Science, 2001. **26**(9): p. 1689-1762.
73. Matsumoto, T., et al., *Solution properties of celluloses from different biological origins in LiCl·DMAc*. Cellulose, 2001. **8**(4): p. 275-282.
74. Dupont, A.-L., *Cellulose in lithium chloride/N,N-dimethylacetamide, optimisation of a dissolution method using paper substrates and stability of the solutions*. Polymer, 2003. **44**(15): p. 4117-4126.
75. Furuno, H., et al., *Chemical structure elucidation of total lignins in woods. Part II: Analysis of a fraction of residual wood left after MWL isolation and solubilized in lithium chloride/N, N-dimethylacetamide*. Holzforschung, 2006. **60**(6): p. 653-658.
76. Zhang, C., et al., *Dissolution mechanism of cellulose in N, N-dimethylacetamide/lithium chloride: revisiting through molecular interactions*. The Journal of Physical Chemistry B, 2014. **118**(31): p. 9507-9514.

77. Zhang, X., et al., *Regenerated cellulose/graphene nanocomposite films prepared in DMAC/LiCl solution*. Carbohydrate Polymers, 2012. **88**(1): p. 26-30.
78. Eberhardt, T.L., S. Lebow, and K.G. Reed, *Partial dissolution of ACQ-treated wood in lithium chloride/N-methyl-2-pyrrolidinone: Separation of copper from potential lignocellulosic feedstocks*. Chemosphere, 2012. **86**(8): p. 797-801.
79. Han, D., et al., *Cellulose/graphite oxide composite films with improved mechanical properties over a wide range of temperature*. Carbohydrate Polymers, 2011. **83**(2): p. 966-972.
80. Luong, N.D., et al., *Graphene/cellulose nanocomposite paper with high electrical and mechanical performances*. Journal of Materials Chemistry, 2011. **21**(36): p. 13991-13998.
81. Secor, E.B., et al., *Inkjet printing of high conductivity, flexible graphene patterns*. The Journal of Physical Chemistry Letters, 2013. **4**(8): p. 1347-1351.
82. Wang, F., et al., *Multifunctional graphene nanoplatelets/cellulose nanocrystals composite paper*. Composites Part B: Engineering, 2015. **79**: p. 521-529.
83. Yan, C., et al., *Highly stretchable piezoresistive graphene-nanocellulose nanopaper for strain sensors*. Advanced Materials, 2014. **26**(13): p. 2022-2027.
84. Xu, H., et al., *A multifunctional wearable sensor based on a graphene/inverse opal cellulose film for simultaneous, in situ monitoring of human motion and sweat*. Nanoscale, 2018. **10**(4): p. 2090-2098.
85. Kafy, A., et al., *Cellulose/graphene nanocomposite as multifunctional electronic and solvent sensor material*. Materials Letters, 2015. **159**: p. 20-23.

86. Ouyang, W., et al., *Scalable preparation of three-dimensional porous structures of reduced graphene oxide/cellulose composites and their application in supercapacitors*. Carbon, 2013. **62**: p. 501-509.
87. Patel, M.U., et al., *Low surface area graphene/cellulose composite as a host matrix for lithium sulphur batteries*. Journal of Power Sources, 2014. **254**: p. 55-61.
88. Tian, M., et al., *Enhanced mechanical and thermal properties of regenerated cellulose/graphene composite fibers*. Carbohydrate Polymers, 2014. **111**: p. 456-462.
89. Mahmoudian, S., et al., *A facile approach to prepare regenerated cellulose/graphene nanoplatelets nanocomposite using room-temperature ionic liquid*. Journal of Nanoscience and Nanotechnology, 2012. **12**(7): p. 5233-5239.
90. Li, Y., et al., *Hybridizing wood cellulose and graphene oxide toward high-performance fibers*. NPG Asia Materials, 2015. **7**(1): p. e150.
91. Li, Y., et al., *Hybridizing wood cellulose and graphene oxide toward high-performance fibers*. NPG Asia Materials, 2015. **7**(1): p. e150-e150.
92. Xu, M., et al., *Highly tough cellulose/graphene composite hydrogels prepared from ionic liquids*. Industrial Crops and Products, 2015. **70**: p. 56-63.
93. Si, H., et al., *One-Step In Situ Biosynthesis of Graphene Oxide–Bacterial Cellulose Nanocomposite Hydrogels*. Macromolecular Rapid Communications, 2014. **35**(19): p. 1706-1711.
94. Wan, C. and J. Li, *Graphene oxide/cellulose aerogels nanocomposite: Preparation, pyrolysis, and application for electromagnetic interference shielding*. Carbohydrate Polymers, 2016. **150**: p. 172-179.
95. Yang, J., et al., *Cellulose/graphene aerogel supported phase change composites with high thermal conductivity and good shape stability for thermal energy storage*. Carbon, 2016. **98**: p. 50-57.

96. Zhang, J., et al., *Graphene-oxide-sheet-induced gelation of cellulose and promoted mechanical properties of composite aerogels*. The Journal of Physical Chemistry C, 2012. **116**(14): p. 8063-8068.
97. Chook, S.W., et al., *A graphene oxide facilitated a highly porous and effective antibacterial regenerated cellulose membrane containing stabilized silver nanoparticles*. Cellulose, 2014. **21**(6): p. 4261-4270.
98. El Miri, N., et al., *Synergistic effect of cellulose nanocrystals/graphene oxide nanosheets as functional hybrid nanofiller for enhancing properties of PVA nanocomposites*. Carbohydrate polymers, 2016. **137**: p. 239-248.
99. Tu, K., et al., *Portable visible-light photocatalysts constructed from Cu₂O nanoparticles and graphene oxide in cellulose matrix*. The Journal of Physical Chemistry C, 2014. **118**(13): p. 7202-7210.
100. Zabetakis, D., M. Dinderman, and P. Schoen, *Metal-Coated Cellulose Fibers for Use in Composites Applicable to Microwave Technology*. Advanced Materials, 2005. **17**(6): p. 734-738.
101. Shi, K., et al., *Efficient lightweight supercapacitor with compression stability*. Advanced Functional Materials, 2016. **26**(35): p. 6437-6445.
102. Baimpos, T., et al., *A polymer-Metglas sensor used to detect volatile organic compounds*. Sensors and Actuators A: Physical, 2010. **158**(2): p. 249-253.
103. Ibanez, F.J. and F.P. Zamborini, *Chemiresistive sensing of volatile organic compounds with films of surfactant-stabilized gold and gold-silver alloy nanoparticles*. ACS Nano, 2008. **2**(8): p. 1543-1552.
104. Consales, M., et al., *SWCNT nano-composite optical sensors for VOC and gas trace detection*. Sensors and Actuators B: Chemical, 2009. **138**(1): p. 351-361.
105. Liu, X., et al., *A survey on gas sensing technology*. Sensors, 2012. **12**(7): p. 9635-9665.

106. Sharma, S. and M. Madou, *A new approach to gas sensing with nanotechnology*. Philosophical Transactions of the Royal Society A: Mathematical, Physical and Engineering Sciences, 2012. **370**(1967): p. 2448-2473.
107. Patra, M., et al., *Nanotechnology applications for chemical and biological sensors*. Defence Science Journal, 2008. **58**(5): p. 636-649.
108. Sun, P., et al., *Dispersive SnO₂ nanosheets: hydrothermal synthesis and gas-sensing properties*. Sensors and Actuators B: Chemical, 2011. **156**(2): p. 779-783.
109. Li, X., et al., *Microwave hydrothermal synthesis and gas sensing application of porous ZnO core-shell microstructures*. RSC Advances, 2014. **4**(61): p. 32538-32543.
110. Sun, P., et al., *Gas sensing with hollow α -Fe₂O₃ urchin-like spheres prepared via template-free hydrothermal synthesis*. CrystEngComm, 2012. **14**(24): p. 8335-8337.
111. Qi, H., et al., *Carbon nanotube–cellulose composite aerogels for vapour sensing*. Sensors and Actuators B: Chemical, 2015. **213**: p. 20-26.
112. Wang, T., et al., *A review on graphene-based gas/vapor sensors with unique properties and potential applications*. Nano-Micro Letters, 2016. **8**(2): p. 95-119.
113. Potyrailo, R.A., *Polymeric sensor materials: toward an alliance of combinatorial and rational design tools?* Angewandte Chemie International Edition, 2006. **45**(5): p. 702-723.
114. Wang, X., et al., *Fabrication and gas sensing behavior of poly (3, 4-ethylenedioxythiophene) coated polypropylene fiber with engineered interface*. Reactive and Functional Polymers, 2017. **112**: p. 74-80.
115. Bhandari, S., *Polymer/carbon composites for sensor application*, in *Carbon-Containing Polymer Composites*. 2019, Springer. p. 503-531.

116. Geim, A. and K. Novoselov, *The rise of graphene, nanoscience and technology: a collection of reviews from nature journals*. World Scientific, 2010: p. 11-19.
117. Brownson, D.A., D.K. Kampouris, and C.E. Banks, *An overview of graphene in energy production and storage applications*. Journal of Power Sources, 2011. **196**(11): p. 4873-4885.
118. Cai, W., et al., *Large area few-layer graphene/graphite films as transparent thin conducting electrodes*. Applied Physics Letters, 2009. **95**(12): p. 123115.
119. Leenaerts, O., B. Partoens, and F. Peeters, *Adsorption of H₂O, NH₃, CO, NO₂, and NO on graphene: A first-principles study*. Physical Review B, 2008. **77**(12): p. 125416.
120. Liu, C., et al., *Graphene-based supercapacitor with an ultrahigh energy density*. Nano Letters, 2010. **10**(12): p. 4863-4868.
121. Wu, Z.-S., et al., *Graphene anchored with Co₃O₄ nanoparticles as anode of lithium ion batteries with enhanced reversible capacity and cyclic performance*. ACS Nano, 2010. **4**(6): p. 3187-3194.
122. Liang, J., et al., *Novel Cu nanowires/graphene as the back contact for CdTe solar cells*. Advanced Functional Materials, 2012. **22**(6): p. 1267-1271.
123. Schedin, F., et al., *Detection of individual gas molecules adsorbed on graphene*. Nature Materials, 2007. **6**(9): p. 652.
124. Lu, G., L.E. Ocola, and J. Chen, *Reduced graphene oxide for room-temperature gas sensors*. Nanotechnology, 2009. **20**(44): p. 445502.
125. Kim, K.S., et al., *Large-scale pattern growth of graphene films for stretchable transparent electrodes*. Nature, 2009. **457**(7230): p. 706.
126. Sutter, P.W., J.-I. Flege, and E.A. Sutter, *Epitaxial graphene on ruthenium*. Nature Materials, 2008. **7**(5): p. 406.

127. Wang, Y. and J.T. Yeow, *A review of carbon nanotubes-based gas sensors*. Journal of sensors, 2009. **2009**.
128. Hüsing, N. and U. Schubert, *Aerogels-airy materials: chemistry, structure, and properties*. Angewandte Chemie International Edition, 1998. **37**(1-2): p. 22-45.
129. Pierre, A.C. and G.M. Pajonk, *Chemistry of aerogels and their applications*. Chemical Reviews, 2002. **102**(11): p. 4243-4266.
130. Qi, H., E. Mäder, and J. Liu, *Unique water sensors based on carbon nanotube-cellulose composites*. Sensors and Actuators B: Chemical, 2013. **185**: p. 225-230.
131. Stankovich, S., et al., *Synthesis of graphene-based nanosheets via chemical reduction of exfoliated graphite oxide*. Carbon, 2007. **45**(7): p. 1558-1565.
132. Zhang, J., et al., *Reduction of graphene oxide via L-ascorbic acid*. Chemical Communications, 2010. **46**(7): p. 1112-1114.
133. Sahoo, S., et al., *Reduced graphene oxide as ultra-fast temperature sensor*. arXiv preprint arXiv:1204.1928, 2012.
134. Di Bartolomeo, A., et al., *Multiwalled carbon nanotube films as small-sized temperature sensors*. Journal of Applied Physics, 2009. **105**(6): p. 064518.
135. Kuo, C.Y., et al., *Nano temperature sensor using selective lateral growth of carbon nanotube between electrodes*. IEEE Transactions on Nanotechnology, 2007. **6**(1): p. 63-69.
136. Gao, S.I., et al., *Glass fibers with carbon nanotube networks as multifunctional sensors*. Advanced Functional Materials, 2010. **20**(12): p. 1885-1893.
137. Deng, Y., et al., *Water Vapor Sensing by Carbon Nanoparticle "Skin"*. Advanced Materials Interfaces, 2015. **2**(18): p. 1500244.

138. Brown, R., *Handbook of polymer testing: physical methods*. 1999: CRC Press.
139. Yamada, T., et al., *A stretchable carbon nanotube strain sensor for human-motion detection*. *Nature Nanotechnology*, 2011. **6**(5): p. 296.
140. Pötschke, P., et al., *Liquid sensing properties of melt processed polypropylene/poly (ϵ -caprolactone) blends containing multiwalled carbon nanotubes*. *Composites Science and Technology*, 2011. **71**(12): p. 1451-1460.
141. Pötschke, P., et al., *Liquid sensing properties of fibres prepared by melt spinning from poly (lactic acid) containing multi-walled carbon nanotubes*. *Composites Science and Technology*, 2010. **70**(2): p. 343-349.
142. Zhang, B., et al., *Enhanced gas sensing properties to acetone vapor achieved by α - Fe_2O_3 particles ameliorated with reduced graphene oxide sheets*. *Sensors and Actuators B: Chemical*, 2017. **241**: p. 904-914.
143. Varghese, S.S., et al., *Recent advances in graphene based gas sensors*. *Sensors and Actuators B: Chemical*, 2015. **218**: p. 160-183.
144. Zhang, B., et al., *Preparation and characterization of gas-sensitive composites from multi-walled carbon nanotubes/polystyrene*. *Sensors and Actuators B: Chemical*, 2005. **109**(2): p. 323-328.
145. Chen, S.G., et al., *Gas sensitivity of carbon black/waterborne polyurethane composites*. *Carbon*, 2004. **42**(3): p. 645-651.
146. Hansen, C.M., *Hansen solubility parameters: a user's handbook*. 2002: CRC Press.
147. Bouvree, A., et al., *Conductive polymer nano-biocomposites (CPC): chitosan-carbon nanoparticle a good candidate to design polar vapour sensors*. *Sensors and Actuators B: Chemical*, 2009. **138**(1): p. 138-147.

148. Lu, J., et al., *Vapour sensing with conductive polymer nanocomposites (CPC): Polycarbonate-carbon nanotubes transducers with hierarchical structure processed by spray layer by layer*. *Sensors and Actuators B: Chemical*, 2009. **140**(2): p. 451-460.
149. Castro, M., et al., *Carbon nanotubes/poly (ϵ -caprolactone) composite vapour sensors*. *Carbon*, 2009. **47**(8): p. 1930-1942.
150. Fan, Q., et al., *Vapor sensing properties of thermoplastic polyurethane multifilament covered with carbon nanotube networks*. *Sensors and Actuators B: Chemical*, 2011. **156**(1): p. 63-70.
151. Devi, L.G., et al., *Photo degradation of Methyl Orange an azo dye by Advanced Fenton Process using zero valent metallic iron: Influence of various reaction parameters and its degradation mechanism*. *Journal of Hazardous Materials*, 2009. **164**(2): p. 459-467.
152. Sun, S.-P., et al., *Decolorization of an azo dye Orange G in aqueous solution by Fenton oxidation process: effect of system parameters and kinetic study*. *Journal of Hazardous Materials*, 2009. **161**(2): p. 1052-1057.
153. Ramirez, J.H., et al., *Modelling of the synthetic dye Orange II degradation using Fenton's reagent: From batch to continuous reactor operation*. *Chemical Engineering Journal*, 2009. **148**(2): p. 394-404.
154. Riaz, N., et al., *Photodegradation of Orange II under visible light using Cu-Ni/TiO₂: effect of calcination temperature*. *Chemical Engineering Journal*, 2012. **185**: p. 108-119.
155. Ember, E., et al., *Metal ion-catalyzed oxidative degradation of Orange II by H₂O₂. High catalytic activity of simple manganese salts*. *New Journal of Chemistry*, 2009. **33**(1): p. 34-49.
156. Gan, P.P. and S.F.Y. Li, *Efficient removal of Rhodamine B using a rice hull-based silica supported iron catalyst by Fenton-like process*. *Chemical Engineering Journal*, 2013. **229**: p. 351-363.

157. Hsueh, C., Y. Huang, and C. Chen, *Novel activated alumina-supported iron oxide-composite as a heterogeneous catalyst for photooxidative degradation of reactive black 5*. Journal of Hazardous Materials, 2006. **129**(1): p. 228-233.
158. Lim, H., et al., *Highly active heterogeneous Fenton catalyst using iron oxide nanoparticles immobilized in alumina coated mesoporous silica*. Chemical Communications, 2006(4): p. 463-465.
159. Ramirez, J.H., et al., *Fenton-like oxidation of Orange II solutions using heterogeneous catalysts based on saponite clay*. Applied Catalysis B: Environmental, 2007. **71**(1): p. 44-56.
160. Garrido-Ramírez, E., B. Theng, and M. Mora, *Clays and oxide minerals as catalysts and nanocatalysts in Fenton-like reactions-a review*. Applied Clay Science, 2010. **47**(3): p. 182-192.
161. Aleksić, M., et al., *Heterogeneous Fenton type processes for the degradation of organic dye pollutant in water-The application of zeolite assisted AOPs*. Desalination, 2010. **257**(1): p. 22-29.
162. Hu, X., et al., *Adsorption and heterogeneous Fenton degradation of 17 α -methyltestosterone on nano Fe₃O₄/MWCNTs in aqueous solution*. Applied Catalysis B: Environmental, 2011. **107**(3): p. 274-283.
163. Zhou, L., et al., *Fe₃O₄/MWCNT as a heterogeneous Fenton catalyst: degradation pathways of tetrabromobisphenol A*. RSC Advances, 2014. **4**(47): p. 24900-24908.
164. Song, S., et al., *Facile synthesis of Fe₃O₄/MWCNTs by spontaneous redox and their catalytic performance*. Nanotechnology, 2010. **21**(18): p. 185602.
165. Deng, J., X. Wen, and Q. Wang, *Solvothermal in situ synthesis of Fe₃O₄-multi-walled carbon nanotubes with enhanced heterogeneous Fenton-like activity*. Materials Research Bulletin, 2012. **47**(11): p. 3369-3376.

166. Rache, M.L., et al., *Azo-dye orange II degradation by the heterogeneous Fenton-like process using a zeolite Y-Fe catalyst—kinetics with a model based on the Fermi's equation*. Applied Catalysis B: Environmental, 2014. **146**: p. 192-200.
167. Duarte, F., et al., *Fenton-like degradation of azo-dye Orange II catalyzed by transition metals on carbon aerogels*. Applied Catalysis B: Environmental, 2009. **85**(3): p. 139-147.
168. Nguyen, T.D., et al., *Magnetic Fe₂MO₄ (M: Fe, Mn) activated carbons: fabrication, characterization and heterogeneous Fenton oxidation of methyl orange*. Journal of Hazardous Materials, 2011. **185**(2): p. 653-661.
169. Rodriguez, A., et al., *Heterogeneous Fenton catalyst supports screening for mono azo dye degradation in contaminated wastewaters*. Ind. Eng. Chem. Res, 2010. **49**(2): p. 498-505.
170. Duan, F., et al., *Heterogeneous Fenton-like degradation of 4-chlorophenol using iron/ordered mesoporous carbon catalyst*. Journal of Environmental Sciences, 2014. **26**(5): p. 1171-1179.
171. Voitko, K.V., et al., *Morphological and chemical features of nano and macroscale carbons affecting hydrogen peroxide decomposition in aqueous media*. Journal of Colloid and Interface Science, 2011. **361**(1): p. 129-136.
172. Zubir, N.A., et al., *Structural and functional investigation of graphene oxide-Fe₃O₄ nanocomposites for the heterogeneous Fenton-like reaction*. Scientific Reports, 2014. **4**: p. 4594.
173. He, H. and C. Gao, *Supraparamagnetic, conductive, and processable multifunctional graphene nanosheets coated with high-density Fe₃O₄ nanoparticles*. ACS Applied Materials & Interfaces, 2010. **2**(11): p. 3201-3210.
174. Wu, H., et al., *Control on the formation of Fe₃O₄ nanoparticles on chemically reduced graphene oxide surfaces*. CrystEngComm, 2012. **14**(2): p. 499-504.

175. Liu, M., et al., *Synthesis of magnetite/graphene oxide composite and application for cobalt (II) removal*. The Journal of Physical Chemistry C, 2011. **115**(51): p. 25234-25240.
176. Ramirez, J.H., C.A. Costa, and L.M. Madeira, *Experimental design to optimize the degradation of the synthetic dye Orange II using Fenton's reagent*. Catalysis Today, 2005. **107**: p. 68-76.
177. Garrido-Ramírez, E., B. Theng, and M. Mora, *Clays and oxide minerals as catalysts and nanocatalysts in Fenton-like reactions-a review*. Applied Clay Science, 2010. **47**(3-4): p. 182-192.
178. Zhang, W., et al., *Unraveling Stress-Induced Toxicity Properties of Graphene Oxide and the Underlying Mechanism*. Advanced Materials, 2012. **24**(39): p. 5391-5397.
179. Matsumoto, Y., et al., *Photoreaction of graphene oxide nanosheets in water*. The Journal of Physical Chemistry C, 2011. **115**(39): p. 19280-19286.
180. Jasuja, K., et al., *Microwave-reduced uncapped metal nanoparticles on graphene: tuning catalytic, electrical, and Raman properties*. The Journal of Physical Chemistry Letters, 2010. **1**(12): p. 1853-1860.
181. Karousis, N., et al., *Graphene oxide with covalently linked porphyrin antennae: Synthesis, characterization and photophysical properties*. Journal of Materials Chemistry, 2011. **21**(1): p. 109-117.
182. Yosefi, L., M. Haghghi, and S. Allahyari, *Solvothermal synthesis of flowerlike p-BiOI/n-ZnFe₂O₄ with enhanced visible light driven nanophotocatalyst used in removal of acid orange 7 from wastewater*. Separation and Purification Technology, 2017. **178**: p. 18-28.
183. Herney-Ramirez, J., et al., *Degradation of Acid Orange 7 using a saponite-based catalyst in wet hydrogen peroxide oxidation: Kinetic study with the Fermi's equation*. Applied Catalysis B: Environmental, 2011. **101**(3-4): p. 197-205.

184. Aghdam, S.M., et al., *Precipitation dispersion of various ratios of BiOI/BiOCl nanocomposite over g-C₃N₄ for promoted visible light nanophotocatalyst used in removal of acid orange 7 from water*. Journal of Photochemistry and Photobiology A: Chemistry, 2017. **338**: p. 201-212.
185. Margan, P. and M. Haghghi, *Sono-coprecipitation synthesis and physicochemical characterization of CdO-ZnO nanophotocatalyst for removal of acid orange 7 from wastewater*. Ultrasonics Sonochemistry, 2018. **40**: p. 323-332.
186. Margan, P. and M. Haghghi, *Hydrothermal-assisted sol-gel synthesis of Cd-doped TiO₂ nanophotocatalyst for removal of acid orange from wastewater*. Journal of Sol-Gel Science and Technology, 2017. **81**(2): p. 556-569.
187. Moradi, M., M. Haghghi, and S. Allahyari, *Precipitation dispersion of Ag-ZnO nanocatalyst over functionalized multiwall carbon nanotube used in degradation of Acid Orange from wastewater*. Process Safety and Environmental Protection, 2017. **107**: p. 414-427.
188. Namai, A., et al., *Synthesis of an electromagnetic wave absorber for high-speed wireless communication*. Journal of the American Chemical Society, 2008. **131**(3): p. 1170-1173.
189. Watts, P.C., et al., *High permittivity from defective multiwalled carbon nanotubes in the X-band*. Advanced Materials, 2003. **15**(7-8): p. 600-603.
190. Shi, Z.c., et al., *Random composites of nickel networks supported by porous alumina toward double negative materials*. Advanced Materials, 2012. **24**(17): p. 2349-2352.
191. Ohkoshi, S.i., et al., *A Millimeter-Wave Absorber Based on Gallium-Substituted ϵ -Iron Oxide Nanomagnets*. Angewandte Chemie International Edition, 2007. **46**(44): p. 8392-8395.

192. Li, N., et al., *Electromagnetic interference (EMI) shielding of single-walled carbon nanotube epoxy composites*. Nano Letters, 2006. **6**(6): p. 1141-1145.
193. Liang, J., et al., *Electromagnetic interference shielding of graphene/epoxy composites*. Carbon, 2009. **47**(3): p. 922-925.
194. Yan, D.-X., et al., *Electromagnetic interference shielding of segregated polymer composite with an ultralow loading of in situ thermally reduced graphene oxide*. Nanotechnology, 2014. **25**(14): p. 145705.
195. Li, B., et al., *Highly organized two-and three-dimensional single-walled carbon nanotube-polymer hybrid architectures*. ACS Nano, 2011. **5**(6): p. 4826-4834.
196. Hsiao, S.-T., et al., *Lightweight and flexible reduced graphene oxide/water-borne polyurethane composites with high electrical conductivity and excellent electromagnetic interference shielding performance*. ACS Applied Materials & Interfaces, 2014. **6**(13): p. 10667-10678.
197. Qin, F. and C. Brosseau, *A review and analysis of microwave absorption in polymer composites filled with carbonaceous particles*. Journal of Applied Physics, 2012. **111**(6): p. 4.
198. Thomassin, J.-M., et al., *Polymer/carbon based composites as electromagnetic interference (EMI) shielding materials*. Materials Science and Engineering: R: Reports, 2013. **74**(7): p. 211-232.
199. Li, B., et al., *Ultrathin SWNT films with tunable, anisotropic transport properties*. Advanced Functional Materials, 2011. **21**(10): p. 1810-1815.
200. Chen, Q.-y., et al., *Nonlinear current-voltage characteristics of conductive polyethylene composites with carbon black filled pet microfibrils*. Chinese Journal of Polymer Science, 2013. **31**(2): p. 211-217.
201. Shi, S.-L. and J. Liang, *The effect of multi-wall carbon nanotubes on electromagnetic interference shielding of ceramic composites*. Nanotechnology, 2008. **19**(25): p. 255707.

202. Xu, C. and X. Wang, *Fabrication of flexible metal-nanoparticle films using graphene oxide sheets as substrates*. *Small*, 2009. **5**(19): p. 2212-2217.
203. Wang, H., et al., *Ni(OH)₂ nanoplates grown on graphene as advanced electrochemical pseudocapacitor materials*. *Journal of the American Chemical Society*, 2010. **132**(21): p. 7472-7477.
204. Cao, X., et al., *Preparation of novel 3D graphene networks for supercapacitor applications*. *Small*, 2011. **7**(22): p. 3163-3168.
205. Zhang, X.-Y., et al., *Graphene/TiO₂ nanocomposites: synthesis, characterization and application in hydrogen evolution from water photocatalytic splitting*. *Journal of Materials Chemistry*, 2010. **20**(14): p. 2801-2806.
206. Huang, X., et al., *Synthesis of gold square-like plates from ultrathin gold square sheets: The evolution of structure phase and shape*. *Angewandte Chemie International Edition*, 2011. **50**(51): p. 12245-12248.
207. Su, J., et al., *Fe₃O₄-graphene nanocomposites with improved lithium storage and magnetism properties*. *The Journal of Physical Chemistry C*, 2011. **115**(30): p. 14469-14477.
208. Shen, B., et al., *Lightweight, multifunctional polyetherimide/graphene@Fe₃O₄ composite foams for shielding of electromagnetic pollution*. *ACS Applied Materials & Interfaces*, 2013. **5**(21): p. 11383-11391.
209. Wang, T., et al., *Graphene-Fe₃O₄ nanohybrids: synthesis and excellent electromagnetic absorption properties*. *Journal of Applied Physics*, 2013. **113**(2): p. 024314.
210. Sun, X., et al., *Laminated magnetic graphene with enhanced electromagnetic wave absorption properties*. *Journal of Materials Chemistry C*, 2013. **1**(4): p. 765-777.

211. Guan, P., X. Zhang, and J. Guo, *Assembled Fe₃O₄ nanoparticles on graphene for enhanced electromagnetic wave losses*. Applied Physics Letters, 2012. **101**(15): p. 153108.
212. Thakur, S. and N. Karak, *Green reduction of graphene oxide by aqueous phytoextracts*. Carbon, 2012. **50**(14): p. 5331-5339.
213. Zhang, H.-B., et al., *Vacuum-assisted synthesis of graphene from thermal exfoliation and reduction of graphite oxide*. Journal of Materials Chemistry, 2011. **21**(14): p. 5392-5397.
214. Stankovich, S., et al., *Stable aqueous dispersions of graphitic nanoplatelets via the reduction of exfoliated graphite oxide in the presence of poly (sodium 4-styrenesulfonate)*. Journal of Materials Chemistry, 2006. **16**(2): p. 155-158.
215. Abraham, J., et al., *Investigation into dielectric behaviour and electromagnetic interference shielding effectiveness of conducting styrene butadiene rubber composites containing ionic liquid modified MWCNT*. Polymer, 2017. **112**: p. 102-115.
216. Yousefi, N., et al., *Highly aligned graphene/polymer nanocomposites with excellent dielectric properties for high-performance electromagnetic interference shielding*. Advanced Materials, 2014. **26**(31): p. 5480-5487.
217. Kim, J.Y., et al., *Enhanced Dielectric Performance in Polymer Composite Films with Carbon Nanotube-Reduced Graphene Oxide Hybrid Filler*. Small, 2014. **10**(16): p. 3405-3411.
218. Wang, B., et al., *Two-layer materials of polyethylene and a carbon nanotube/cyanate ester composite with high dielectric constant and extremely low dielectric loss*. Carbon, 2013. **54**: p. 224-233.
219. Zheng, J., et al., *Enhanced microwave electromagnetic properties of Fe₃O₄/graphene nanosheet composites*. Journal of Alloys and Compounds, 2014. **589**: p. 174-181.

220. Zong, M., et al., *One-pot simplified co-precipitation synthesis of reduced graphene oxide/Fe₃O₄ composite and its microwave electromagnetic properties*. Materials Letters, 2013. **106**: p. 22-25.
221. Colaneri, N.F. and L. Schacklette, *EMI shielding measurements of conductive polymer blends*. IEEE Transactions on Instrumentation and Measurement, 1992. **41**(2): p. 291-297.
222. Ohlan, A., et al., *Microwave absorption behavior of core-shell structured poly(3, 4-ethylenedioxy thiophene)-barium ferrite nanocomposites*. ACS Applied Materials & Interfaces, 2010. **2**(3): p. 927-933.
223. Ohlan, A., et al., *Microwave absorption properties of conducting polymer composite with barium ferrite nanoparticles in 12.4-18 GHz*. Applied Physics Letters, 2008. **93**(5): p. 053114.
224. Das, N.C., et al., *Single-walled carbon nanotube/poly (methyl methacrylate) composites for electromagnetic interference shielding*. Polymer Engineering & Science, 2009. **49**(8): p. 1627-1634.
225. Feng, X., et al., *High Electromagnetic Interference Shielding Effectiveness of Carbon Nanotube-Cellulose Composite Films with Layered Structures*. Macromolecular Materials and Engineering, 2018. **303**(11): p. 1800377.
226. Jana, P., A. Mallick, and S. De, *Electromagnetic interference shielding effectiveness of short carbon fibre-filled polychloroprene vulcanized by barium ferrite*. Journal of Materials Science, 1993. **28**(8): p. 2097-2104.
227. Phang, S.-W., et al., *Applications of polyaniline doubly doped with p-toluene sulphonic acid and dichloroacetic acid as microwave absorbing and shielding materials*. Materials Chemistry and Physics, 2007. **104**(2-3): p. 327-335.
228. Jana, P., A. Mallick, and S. De, *Effects of sample thickness and fiber aspect ratio on EMI shielding effectiveness of carbon fiber filled polychloroprene composites in the X-band frequency range*. IEEE Transactions on Electromagnetic Compatibility, 1992. **34**(4): p. 478-481.

229. Zhang, H.-B., et al., *Tough graphene– polymer microcellular foams for electromagnetic interference shielding*. ACS Applied Materials & Interfaces, 2011. **3**(3): p. 918-924.
230. Huang, H.-D., et al., *Cellulose composite aerogel for highly efficient electromagnetic interference shielding*. Journal of Materials Chemistry A, 2015. **3**(9): p. 4983-4991.

Publications and attended conferences

1. Yian Chen, Petra Pötschke, Jürgen Pionteck, Brigitte Voit, and Haisong Qi. Smart cellulose/graphene composites fabricated by in-situ chemical reduction of graphene oxide for multiple sensing applications. *J. Mater. Chem. A*, 2018,6, 7777-7785;
2. Yian Chen, Petra Pötschke, Jürgen Pionteck, Brigitte Voit, and Haisong Qi. Fe₃O₄ Nanoparticles Grown on Cellulose/GO Hydrogels as Advanced Catalytic Materials for the Heterogeneous Fenton-like Reaction. *ACS Omega* 2019,4,3 5117-5125;
3. Yian Chen, Petra Pötschke, Jürgen Pionteck, Brigitte Voit, and Haisong Qi. Multifunctional Cellulose/Graphene/Fe₃O₄ Composite Aerogels for Electromagnetic Interference Shielding. (To be submitted);
4. Yian Chen, Petra Pötschke, Jürgen Pionteck, Brigitte Voit, and Haisong Qi. Reduced Graphene Oxide-Cellulose Aerogels for Vapour Sensing Applications. (To be submitted);
5. Minoj Gnanaseelan, Yian Chen, Jinji Luo, Beate Krause, Jürgen Pionteck, Petra Pötschke, Haisong Qi. Cellulose-carbon nanotube composite aerogels as novel thermoelectric materials. *Composites Science and Technology*, 2018, 163: 133-140;
6. Yian Chen, Petra Pötschke, Jürgen Pionteck, Brigitte Voit, and Haisong Qi. Smart cellulose/graphene composites fabricated by in-situ chemical reduction of graphene oxide for multiple sensing applications. Poster, CNPComp2019, London, England.

Versicherung

Hiermit versichere ich, dass ich die vorliegende Arbeit ohne unzulässige Hilfe Dritter und ohne Benutzung anderer als der angegebenen Hilfsmittel angefertigt habe; die aus fremden Quellen direkt oder indirekt übernommen Gedanken sind als solche kenntlich gemacht. Die Arbeit wurde bisher weder im Inland noch im Ausland in gleicher oder ähnlicher Form einer anderen Prüfungsbehörde vorgelegt.

Datum:

Unterschrift:

Erklärung

Frühere Promotionsverfahren haben nicht stattgefunden.

Die vorliegende Arbeit wurde in der Zeit von Oktober 2016 bis März 2020 am Leibniz-Institut für Polymerforschung Dresden e.V. im Rahmen des Projektes zum Thema:“ Synthesis and Characterization of Novel Functional Materials based on Cellulose and Graphene oxide” unter wissenschaftlicher Betreuung von Frau Dr. rer. nat. Petra Pötschke und Frau Prof. Dr. Brigitte Voit durchgeführt.

Ich erkenne die Promotionsordnung der Fakultät Chemie und Lebensmittelchemie der Technischen Universität Dresden vom 01.11.2016 in vollem Umfang an.

Datum:

Unterschrift: